

INFN - Laboratori Nazionali di Frascati
Servizio Documentazione

LNF-93/021 (IR)
11 Maggio 1993

FINUDA

A DETECTOR FOR NUCLEAR PHYSICS AT DAΦNE

M. Agnello^a, G. Belli^b, G. Bendiscioli^c, G.C. Bonazzola^d, E. Botta^d, T. Bressani^d, D. Calvo^d, P. Camerini^e, C. Cattaneo^c, N. Colonna^f, M. Corradini^b, S. Costa^d, G. D'Erasmus^f, F. D'Isep^d, A. Donzella^b, A. Feliciello^d, A. Filippi^d, V. Filippini^c, E.M. Fiore^f, L. Fiore^f, P. Gianotti^g, D.R. Gill^h, N. Grion^e, C. Guaraldo^g, A.E. Kuzminⁱ, F. Iazzi^a, A. Lanaro^g, L. Lee^h, E. Lodi Rizzini^b, V. Lucherini^g, S. Marcello^d, G.M. Marshall^h, B. Minetti^a, P. Montagna^c, A.A. Nozdrin^h, A. Olin^h, A. Pantaleo^f, V. Patricchio^f, I.L. Pisarevⁱ, E. Rossetto^d, A. Rotondi^c, R. Rui^e, P. Salvini^c, B.Z. Serduykⁱ, A. Sharma^d, G. Smith^h, S. Tessaro^e, L. Venturelli^b, S. Yen^h and A. Zenoni^l

^a*Dipartimento di Fisica del Politecnico di Torino and INFN, Sezione di Torino, I-10125 Torino, Italy*

^b*Dipartimento di Elettronica per l'Automazione, Università di Brescia and INFN, Sezione di Torino, I-25060 Brescia, Italy*

^c*Dipartimento di Fisica Nucleare e Teorica, Università di Pavia and INFN, Sezione di Pavia, I-27100 Pavia, Italy*

^d*Dipartimento di Fisica Sperimentale, Università di Torino and INFN, Sezione di Torino, I-10125 Torino, Italy*

^e*Dipartimento di Fisica, Università di Trieste and INFN, Sezione di Trieste, I-34127 Trieste, Italy*

^f*Dipartimento di Fisica, Università di Bari and INFN, Sezione di Bari, I-70126 Bari, Italy*

^g*Istituto Nazionale di Fisica Nucleare, Laboratori Nazionali di Frascati, I-00044 Frascati, Italy*

^h*TRIUMF, 4004 Wesbrook Mall, Vancouver, BC, V6T 2A3, Canada*

ⁱ*Joint Institute for Nuclear Research, Dubna, SU-101000 Moscow, Russia*

^l*Dipartimento di Elettronica per l'Automazione, Università di Brescia and INFN, Sezione di Pavia, I-25060 Brescia, Italy*

ABSTRACT

We propose the construction of a detector dedicated to Nuclear Physics studies, called FINUDA, at DAΦNE, the Frascati Φ-Factory. The initial physics program is focused on the spectroscopy and decay modes of Λ-hypernuclei, which are produced following the stopping of tagged K^- in nuclear targets. The unique property of kaons at DAΦNE, coupled to the expected performances of FINUDA (momentum resolution of 0.2% FWHM and dedicated triggers) will allow an unprecedented step forward concerning the precision of the measurements and, even more, the counting rates. At $\mathcal{L} = 10^{32} \text{ cm}^{-2} \text{ s}^{-1}$ we expect to produce and carefully study about 20 hypernuclei, most of them new. The puzzling situation regarding the validity of the $\Delta I = \frac{1}{2}$ rule for non-mesonic decays of hypernuclei will be hopefully clarified. FINUDA could also be used for measurements on low energy $K\mathcal{N}$ interactions.

1 Introduction

The Frascati ϕ -factory DAΦNE [1] will provide, from 1995, some 10^3 $K\bar{K}$ pairs/s at ~ 16 MeV, background free and tagged. Besides the main goal of profiting of this unique possibility for a precise measurement of $\Re(\varepsilon'/\varepsilon)$ to $\sim 10^{-4}$ and of other CP violating parameters in the $K\bar{K}$ system [2], the kaons at DAΦNE obtained from ϕ decay (see. Tab. 1) could be used for other measurements, in particular for Nuclear Physics experiments.

Table 1: ϕ decays.

Mode	B.R.(%)	p_{max} (MeV/c)
K^+K^-	49	127
$K_S^0K_L^0$	34	110
$\rho\pi$	13	182
$\pi^+\pi^-\pi^0$	2	462
$\eta\gamma$	1.3	362
other	~ 1	-

For some specific measurements for which the availability of low-energy kaons and their cleanliness are a mandatory prerequisite, DAΦNE may allow measurements of better quality and comparable counting rates than an advanced proton machine, like KAON [3]. It was noticed by Bressani [4] that K^- from ϕ decays at a ϕ -factory offer a unique opportunity for high resolution hypernuclear spectroscopy with K^- at rest.

The reason is clear if one looks at Table 2 in which the probabilities of the K^\pm to survive after a given length are reported as a function of the energy. At proton machines, where kaons are emitted from an external production target, the distance between the source of particles and the experimental area is at least of $10 \div 15$ m, for radiation safety requirements. K^\pm of less than $400 \div 450$ MeV/c cannot obviously survive to such a distance in numbers suitable for an intense beam. Then, for experiments where lower energies (including stopping K^-) are needed, one has to degrade in momentum a $500 \div 600$ MeV/c beam with a moderator just in front of the experimental apparatus. The moderator introduces a large uncertainty in the momenta of the outgoing particles due to straggling. For experiments with stopped K^- , one is then obliged to use rather thick targets (at least 1 g/cm²) in order to have an acceptable stopping rate. Unfortunately, a thick target introduces an error on the momentum of the emitted charged particles due to the uncertainty in the interaction point, that cannot be accounted for. Often, the high resolution of the spectrometers coupled to such a stopping device is then useless.

Table 2: Probabilities $P(x)$ of survival of K^\pm at different energies after a given length $x(\text{cm})$.

T (MeV)	p (MeV/c)	P(3)	P(50)	P(100)
10.0	100	0.96	0.51	0.26
30.0	175	0.98	0.68	0.47
50.0	228	0.98	0.75	0.56
100.0	330	0.99	0.82	0.67

On the contrary, the ~ 16 MeV (K^+ , K^-) produced at DAΦNE stop in a material thickness of less than 100 mg/cm^2 , and the uncertainty of the interaction point gives a $\Delta p/p$ of the outgoing particles well matched with the resolution of the best magnetic spectrometers that can be designed.

Nuclear physics experiments, listed below, require the best energy resolution that may be achieved with the present technologies. Taking into account the 4π geometry over which the kaons are emitted from the interaction region, a cylindrical magnetic spectrometer around the interaction region must be built. Such a spectrometer, whose main features will be described in the following, will be called by the acronym FINUDA (Fisica NUcleare a DAΦNE). In addition to one-arm experiments, such a detector will be used for coincidence experiments and must be able to detect also other particles (charged or neutral) emitted following the interaction of K^- with nuclei. The large solid angle of detection, typical of detectors at intersecting beam machines, would be a further advantage compared to spectrometers built at fixed target machines.

2 The physics program of FINUDA

2.1 Λ -hypernuclei spectroscopy

A hypernucleus is a many-body system composed of non-strange nucleons and one or more strange baryons (Λ , Σ , Ξ). Considering the simplest known case, the presence of a strangeness degree of freedom in a Λ -hypernucleus adds a new dimension to our evolving picture of nuclear physics. At the hadron level, such hypernuclei provide a new many-body spectroscopy, where dynamical symmetries may appear that are forbidden in ordinary nuclei by the Pauli principle.

In the simple valence quark model, baryons are composed of three quarks symmetrized in flavor-spin, and antisymmetrized in color. The proton, the neutron and the Λ

are the lightest three baryons in the ground-state baryon octet, and they were chosen by Sakata in his prequark triplet model to represent the fundamental particle system from which all other baryons could be constructed [5]. In conventional nuclear physics, it is simplest to discuss Λ -hypernuclei using the Sakata triplet concept. Thus, the triplet set of particles (p , n , Λ) are considered identical to first order under the strong interaction [6]. Therefore, the concept of strangeness exchange is similar to the more familiar concept of charge exchange, and the Λ is treated, with the exception of the Pauli principle, as another nucleon. Of course, strangeness symmetry is broken, as is reflected in the significantly larger mass of the Λ , and the weaker Λ - \mathcal{N} potential. However, it is preserved sufficiently to provide an extremely useful way to discuss Λ -hypernuclei states and reactions.

To a large extent the Λ is expected to maintain its identity within the nuclear medium. This reflects the standard picture that nucleons retain their identity in nuclei. Thus, structure of light hypernuclei, the first ones to be studied with some detail in counter experiments, has been described using a simple shell-model basis, as in conventional nuclear dynamics. The Λ , as a distinguishable baryon, resides in the 1s shell for the hypernuclear ground state. In heavy nuclei we may expect that the Λ would stay deep within the nuclear medium. Single particle states would then appear in Λ -hypernuclei, in a much more cleaner way than in ordinary nuclei, since the difficulties linked to the Pauli exclusion principle and to the pairing interactions will be absent.

Fig. 1 shows an excitation spectrum in ${}^{89}_{\Lambda}\text{Y}$ obtained at the Brookhaven AGS, showing s, p, d, f, and g Λ -orbitals [7]; it demonstrates in a striking way the validity of the concept of shell model orbitals, not just in the valence region, but deep within the nuclear interior. In non strange nuclei, the single-particle strength is broadly fragmented with excitation energy, and a deeply bound hole-state is so fragmented as to be essentially unobservable. In a Λ -hypernucleus, the distinguishable Λ may occupy any orbital, leading to a well-defined, sharp set of states. The spectrum of Fig. 1 was taken with a resolution of 2.6 MeV FWHM and only the major shell orbitals are resolved. With better resolution, more details due to spin splitting of different states may appear.

The above arguments indicate that, to a first approximation, and with the scarce energy resolution so far accessible in the experiments, Λ remains as a composite particle well distinguishable within the nucleus. However, it is possible that high resolution experiments may reveal effects due to a partial deconfinement of Λ in nuclear matter. Following the success of some of the quark models in outlining many features of the baryon spectrum, it has been suggested that they could be even more appropriate for describing the short range region of the baryon-baryon interaction. Following this approach, the nucleus has

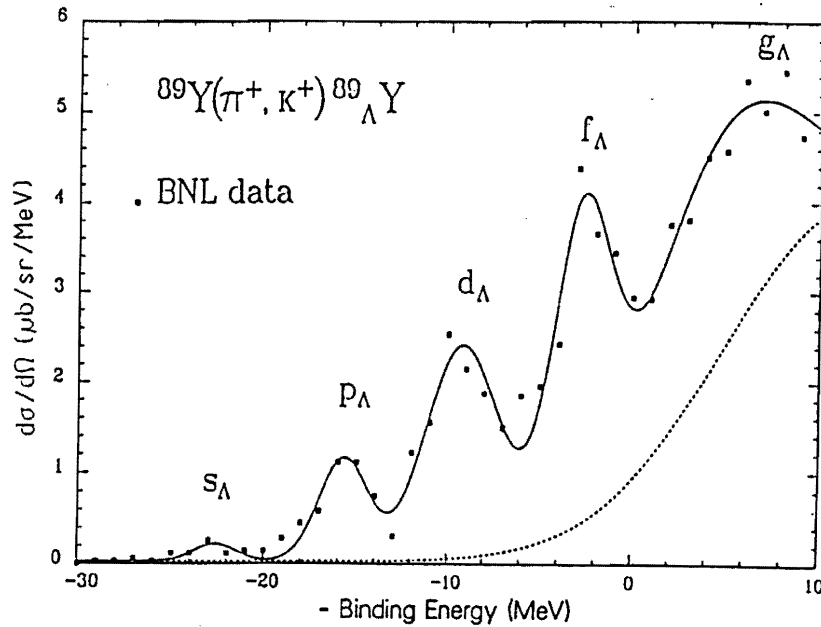


Figure 1: Hypernuclear states obtained in the $^{89}\text{Y}(\pi^+, K^+)^{89}_{\Lambda}\text{Y}$ reaction, showing the Λ in the s, p, d, f and g orbitals, as measured at AGS. The solid line represents a DWBA calculation (from Ref.[7]).

to be represented as built up with quark bags. Due to the confinement, the bags behave like baryons at relatively large distances (> 1 fm) and interact through boson exchange as in the conventional model. At shorter distances (< 1 fm), the bags may overlap and fuse to form larger bags of six (or nine) quarks, where the interaction is carried out by quark and gluon exchange.

An example of how hypernuclear physics may give unique answers to this fundamental problem is shown by Fig. 2.

In the first row the baryon configuration for ^4He and $^5_{\Lambda}\text{He}$ are reported. The baryons are assumed to be distinguishable, with the component quarks fully confined. In the second row the opposite hypothesis is assumed, i.e. the quarks are fully deconfined, so that they occupy quark shell orbitals. For ^4He there is no substantial difference between the nucleon and quark description. For $^5_{\Lambda}\text{He}$, on the contrary, one can notice that the u- and d- quarks of the Λ cannot stay in the $s_{\frac{1}{2}}$ orbital, but in the $p_{\frac{3}{2}}$ one, whereas the s-quark may occupy the lowest energy state. In the baryon picture, all the 5 elementary constituents may occupy the $s_{\frac{1}{2}}$ orbital. Then, if there is a partial deconfinement of the

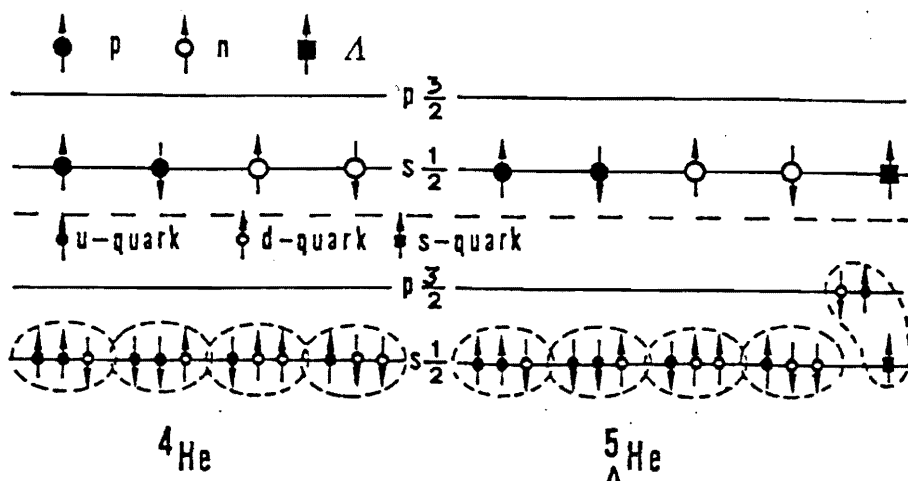


Figure 2: Baryon (upper row) and quark (lower row) configurations for the ${}^4\text{He}$ and ${}^5_{\Lambda}\text{He}$ systems.

quarks in nuclei, this effect could manifest itself more clearly in hypernuclei. As a matter of fact, the binding energy of the ${}^5_{\Lambda}\text{He}$ in the ground state is slightly smaller than that expected with the baryon picture [8], but more data on many hypernuclei are necessary before drawing any conclusion. We refer to recent Conference Proceedings [9], [10] or review articles [11], [12] for a general discussion on the importance of the Hypernuclei spectroscopy.

In conclusion, there is a very rich field of nuclear physics, conventional but perhaps new, that may be addressed by means of high resolution spectroscopy, and DAΦNE is a well suited machine to this purpose.

2.2 Decay of hypernuclei and possible violation of the $\Delta I = \frac{1}{2}$ rule

In this section we will outline the physics interest of this fascinating subject. A very complete and up-to-date review is due to Cohen [13].

A free Λ -hyperon decays into a nucleon and a pion through the weak non-leptonic decay:

$$\Lambda \rightarrow p + \pi^- (\sim 64\%) \quad (1)$$

$$\Lambda \rightarrow n + \pi^0 (\sim 36\%) \quad (2)$$

The lifetime τ_{Λ} is $2.63 \pm 0.02 \times 10^{-10}$ s, the energy released is $Q = 37$ MeV and the

corresponding momentum of the nucleon is about 100 MeV/c, or approximately 5 MeV of kinetic energy.

The decays (1) and (2) may occur with an isospin change (ΔI) of $\frac{1}{2}$ or $\frac{3}{2}$. An s -quark converts to a u - (or a d -) quark through W boson exchange. The V-A Hamiltonian describing this decay can be written as:

$$\mathcal{H}_{V-A} = \frac{G_F}{\sqrt{2}} \sin \vartheta_c \cos \vartheta_c \bar{u} \gamma_\mu (1 - \gamma_5) s \bar{d} \gamma^\mu (1 - \gamma_5) u + c.c. \quad (3)$$

ϑ_c being the Cabibbo angle. Such a model assumes equal contributions for $\Delta I = \frac{1}{2}$ and $\Delta I = \frac{3}{2}$ transitions. However, the experimental branching ratios of (1) and (2), as well as the branching ratios of other strange particles decays, imply that the $\Delta I = \frac{1}{2}$ amplitude is enhanced by at least one order of magnitude. It is immediate to see in fact that the experimental ratio between the two dominating decays is given approximately by the square of the Clebsch-Gordan coefficients in the $\Delta I = \frac{1}{2}$ amplitude:

$$|\frac{1}{2}, -\frac{1}{2}\rangle = \sqrt{\frac{2}{3}} |p\pi^-\rangle - \sqrt{\frac{1}{3}} |n\pi^0\rangle \quad (4)$$

Λ -hypernuclei in their ground state, or in low-lying excited states with a γ -decay lifetime larger than the free Λ lifetime, decay also via weak-interaction mechanism. However, the weak decay of the free Λ -hyperon changes totally when it is embedded in nuclear matter. The binding energy B_Λ increases linearly with A , reaching the saturation value of 25 MeV for heavy hypernuclei, and the phase space for the mesonic decays (1) and (2) is greatly reduced. The final-state nucleon produced in the decay has a very low momentum (< 100 MeV/c), and the process is consequently Pauli-blocked. We recall that the Fermi momentum for a nucleon in a nucleus is ~ 270 MeV/c.

It has long time been recognized that, because the mesonic decay mode would be strongly inhibited in all but the lightest hypernuclei [14], the primary decay channel would be the non-leptonic weak reaction $\Lambda \mathcal{N} \rightarrow \mathcal{N} \mathcal{N}$, referred to as non-mesonic decay. The energy release is approximately 176 MeV, corresponding to a momentum of each of the final nucleons of ~ 417 MeV/c. This decay mode has a much larger phase space, compared to that of the mesonic one, and the final nucleons are not Pauli-blocked. A measurement of the relative branching ratio for the non-mesonic channels:

$$\Lambda + p \rightarrow n + p \quad (5)$$

$$\Lambda + n \rightarrow n + n \quad (6)$$

could provide information about the structure of the weak Hamiltonian, in particular on the relative importance of the $\Delta I = \frac{1}{2}$ and $\Delta I = \frac{3}{2}$ amplitudes.

However, particular care must be devoted to many different effects related to the nuclear medium (initial and final state interactions, nuclear structure, ...) that can strongly distort the true weak interaction mechanism. A very detailed discussion of all these effects can be found in Ref [13].

In spite of the great physics interest for the decay of hypernuclei, the data up to now available are scarce and not precise. This is due to the tremendous difficulty in producing abundantly Λ -hypernuclei in their ground states and detecting the products of their decay. Extremely hard is to study the non-mesonic decay (6) for which two fast neutrons have

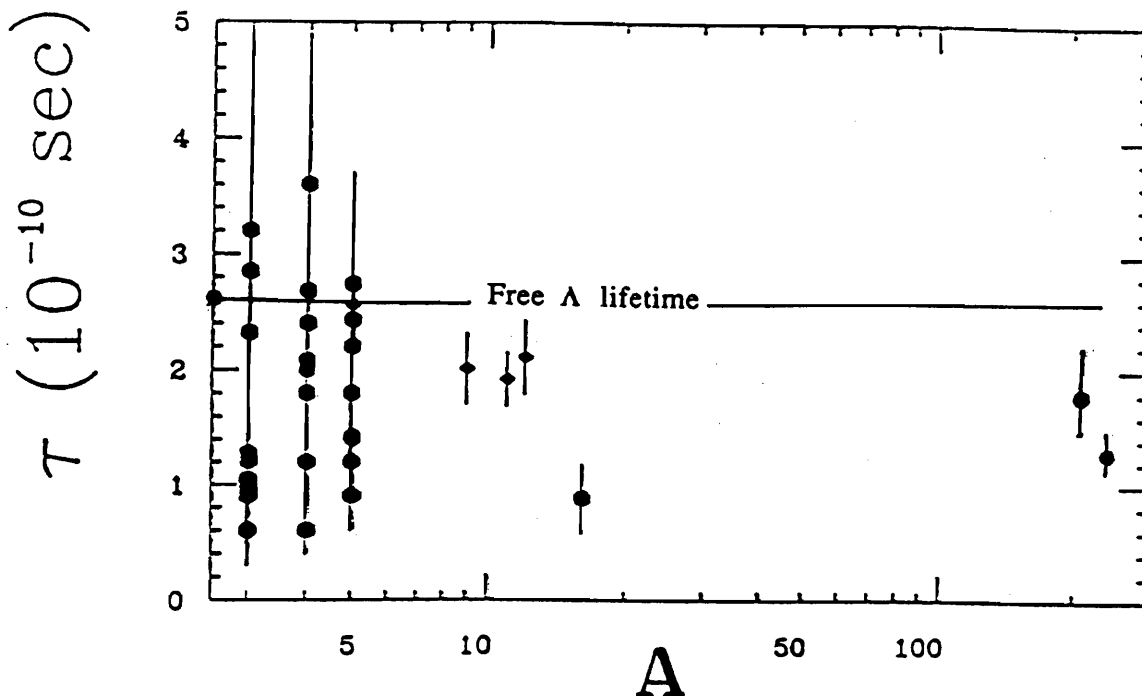


Figure 3: Present experimental values of the lifetime τ_{Λ} of the Λ -hyperon in hypernuclei as a function of A (from Ref. [13]) with the addition of the new measurement for ${}^{238}_{\Lambda}\text{U}$.

to be detected in coincidence and related to the hypernuclear ground states. Clearly, the fact that in nuclear matter the decay channels of the Λ are different than in the free space may have effects too on the value of the lifetime τ_{Λ} . Fig. 3 shows the values of the lifetime

τ_Λ of the Λ -hyperon in various hypernuclei, as a function of the mass number A . One may observe the big errors affecting the measurements. It is interesting to note that the values of τ_Λ reported in Fig. 3 were obtained by quite different techniques. The values for the light hypernuclei ($A \leq 5$) are from old bubble chamber and emulsion experiments, a part a new recent measurement for ${}^5_\Lambda\text{He}$ from a counter experiment at the Brookhaven AGS [15]. The values for $9 \leq A \leq 12$ were also given by this last experiment. The lifetime for ${}^{16}_\Lambda\text{O}$ was measured by an unusual technique, by bombarding with a relativistic ${}^{16}\text{O}$ beam a polyethylene target [16]. τ_Λ for ${}^{209}_\Lambda\text{Bi}$ and ${}^{238}_\Lambda\text{U}$ was measured at CERN LEAR by studying the delayed fission following \bar{p} annihilation at rest [17]. The most recent analysis [18] of this experiment has provided for the lifetime of heavy hypernuclei a value of $(1.25 \pm 0.15) \times 10^{-10}$ s. Even with this precision, the experimental situation indicates a decrease of τ_Λ in nuclear matter. An experiment providing τ_Λ in nuclei as a function of A with the same apparatus and techniques is clearly needed.

Fig. 4 shows the ratio Q^- of non-mesonic to π^- mesonic decay as a function of A ; again one may notice that large errors are affecting the measurements, relevant also to the mass number of the decaying hypernucleus (old emulsion experiments). However, a general trend showing the dominance of non mesonic decays over the mesonic ones for $A \geq 3$ is evident. It is expected that the ratio between the π^- and π^0 mesonic modes could be modified with respect to the free Λ ratio (1) and (2) in light nuclei due to the Pauli blocking on different nucleons. A systematic theoretical study of the mesonic decay for the p-shell hypernuclei was performed by Itonaga [19], and a measurement of the π^0 decay of ${}^{12}_\Lambda\text{C}$, recently performed at KEK [20], though affected by a large error, was in agreement with the calculation.

Fig. 5 shows the ratio q of the $\Lambda + n \rightarrow n + n$ non-mesonic decay to the total non-mesonic decay as a function of A . The errors are very large, since we are dealing with the decay experimentally most difficult to detect. An increase of q with A is evident.

A very recent analysis of the non-mesonic decay for light hypernuclei (${}^4_\Lambda\text{H}$, ${}^4_\Lambda\text{He}$ and ${}^5_\Lambda\text{He}$), performed by Schumacher [21], showed an apparent violation of the $\Delta I = \frac{1}{2}$ rule. In light hypernuclei, 1S_0 and 3S_1 initial $\Lambda\mathcal{N}$ spin configurations with isospin $\frac{1}{2}$ can decay non-mesonically to six $\mathcal{N}\mathcal{N}$ final state spin configurations with isospin of either 1 or 0. For any reaction mechanism leading to $I = 1$ final states, the ratio of neutron-neutron decay (R_n) to proton neutron decay (R_p) is given by:

$$\frac{R_n}{R_p} = \frac{\lambda^2 + 4 - 4\lambda}{2\lambda^2 + 2 + 4\lambda}, \quad (7)$$

where λ is the ratio of the isospin 3/2 decay amplitude to the isospin 1/2 decay amplitude.

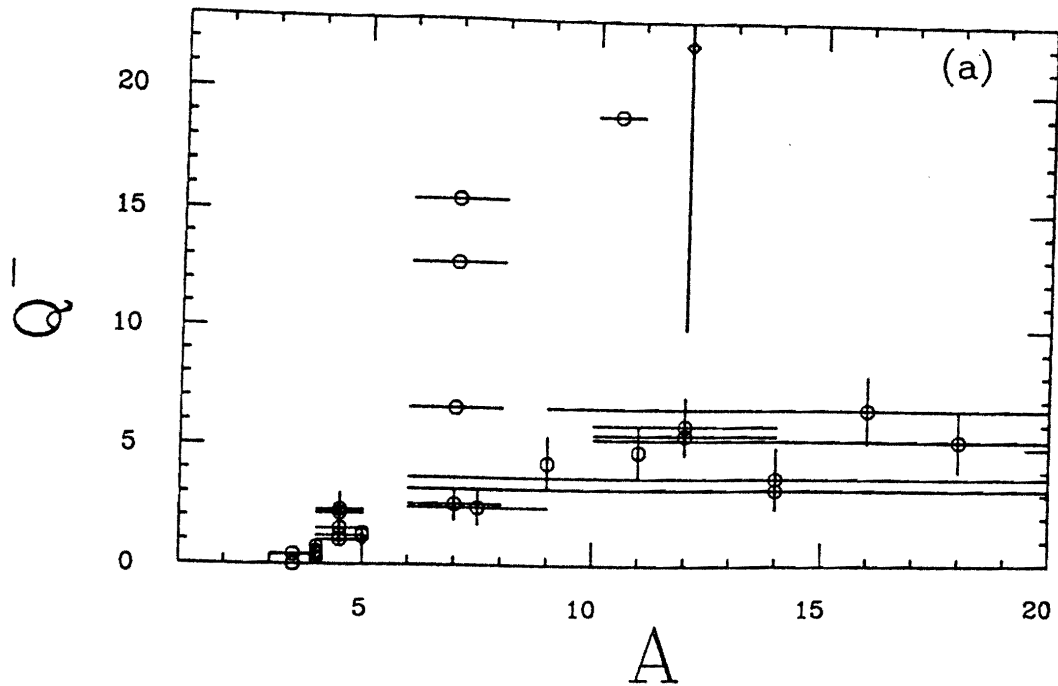


Figure 4: Ratio Q^- of non-mesonic to π^- mesonic decay rates as a function of A (from Ref. [13]).

Defining furthermore R_{NS} as the rate for the $\Lambda N \rightarrow N N$ decay from spin state S , it follows that for pure $\Delta I = \frac{1}{2}$ rule interactions we have $R_{n0} = 2 R_{p0}$ ($I = 1$ final state only) and $R_{n1} \leq 2 R_{p1}$ (both $I = 0$ and 1 final states). Hence the quantity which is obtained by Schumacher is the ratio $r = R_{n0}/R_{p0}$, which for the pure $\Delta I = \frac{1}{2}$ interaction must be 2, and for $\Delta I = \frac{3}{2}$ interaction would be $1/2$. He finds from the data $r = 0.23 \pm 0.17$, suggesting a rather large violation in the case of light hypernuclei. However, the above error was obtained treating the errors on the experimental values as independent and uncorrelated. A more careful analysis of the possible correlation between the errors leads to the conclusion that the data are not consistent with pure $\Delta I = \frac{1}{2}$ hypothesis at the 1.6σ level and suggest that the $\Delta I = \frac{3}{2}$ amplitude may be comparable to or possibly larger than the $\Delta I = \frac{1}{2}$ piece. However we recall that other approaches [22], [23] to the non-mesonic decay of Λ -hypernuclei predict values of the Q^- and q ratios different than those so far discussed still maintaining the validity of the $\Delta I = \frac{1}{2}$ rule. These approaches require more than two baryons in the initial/final state.

These remarks strongly support the interest in performing accurate measurements on the decay modes of hypernuclei and, possibly, of the Λ lifetime.

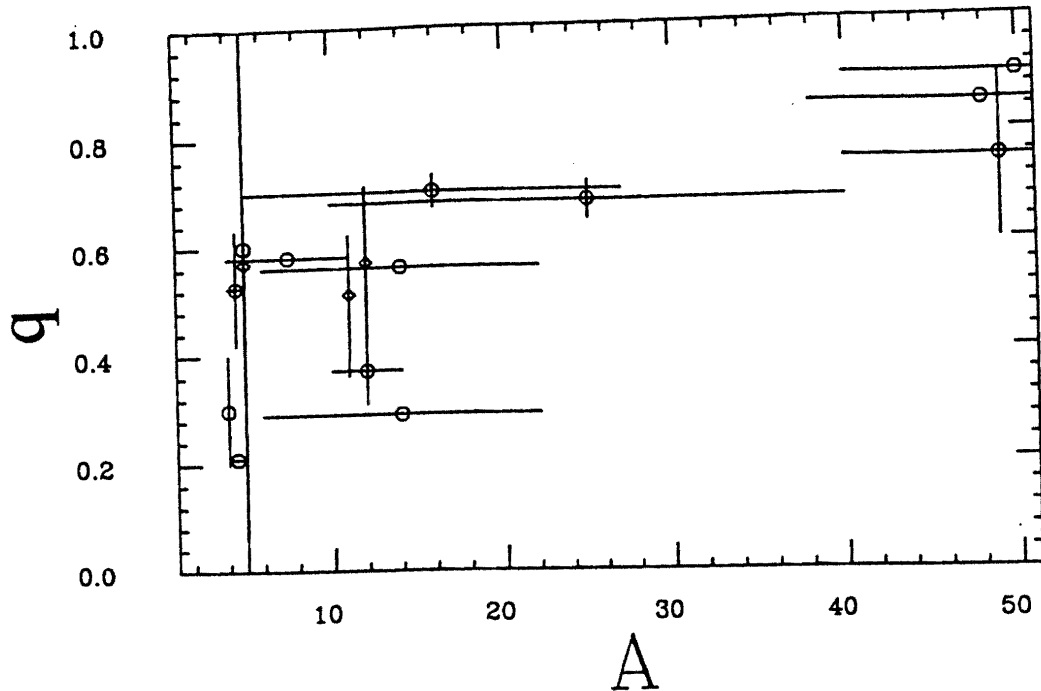
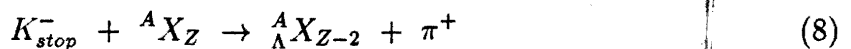


Figure 5: Ratio of neutron stimulated non-mesonic decay rate to the total non-mesonic decay rate as a function of A (from Ref. [13]).

2.3 Production of Λ -hypernuclei with a large neutron excess

As it will be discussed with more details in Sec. 3, experiments with magnetic spectrometers have studied essentially the production of Λ -hypernuclei by means of two-body reactions, in which one of the neutrons of the nuclear target was transformed into a Λ . Even at DAΦNE, the dominant reaction that will be used is the (K_{stop}^-, π^-) one. However, due to the expected high rate of stopped K^- , two step reactions occurring in the same nucleus could be detectable. In particular, as pointed out by Majling [24], a (K_{stop}^-, π^0) reaction on a proton followed by a (π^0, π^+) reaction on another proton would produce at the end a neutron-rich hypernucleus:



The rate for the two-step reaction (8) would be lower by two orders of magnitudes than that for the one step reactions (K_{stop}^-, π^-) , (K_{stop}^-, π^0) , whose rate is typically 10^{-3} /stopped K^- .

We may be rather sure of this estimate, bearing in mind the ratio of the analogous

two-step (π^\pm, π^\mp) double charge exchange reactions on nuclei with the one-step charge exchange ones (π^\pm, π^0) [25]. Fig 6 shows the chart of light Λ -hypernuclei with the new neutron rich species that could possibly be observed.

As it will be discussed in Sec. 5, a production rate of 10^{-5} /stopped K^- is within the capabilities of FINUDA at DAΦNE. If detected, reactions like (8) will really open a new window on the hypernuclear species that may be produced, namely:

- 1) all hypernuclei produced by (K^-, π^+) reactions would be new, they were never observed until now;
- 2) some of the new species must be stable, since their nuclear core is already stable;
- 3) it is also possible to produce very heavy Hyperhydrogen isotopes ${}^6_{\Lambda}H$ and ${}^7_{\Lambda}H$, from 6Li and 7Li targets.

2.4 Is there a π^+ decay mode of hypernuclei?

The H particle has been the subject of theoretical and experimental studies following the Jaffe proposal [26] based upon the MIT bag model. A careful review on the H particle was performed by Guaraldo [27]. Although there has been no evidence of the existence of the H , no experiment can exclude the possibility of strongly bound H particle. A recent lattice QCD calculation [28], performed with the largest lattice size even used for the H mass, shows that the mass could be quite light, even lighter than that of two nucleons. In that case the H becomes stable not only against strong decays but also weak decays. On the other hand, if the H particle is lighter than two nucleons, a nucleus become unstable against $\Delta S = -2$ double β decay producing the H as final state product. The most stringent lower limit on the H mass, as given by double β decay, is 1800 MeV.

Kishimoto [29] has pointed out that there is a window in the H mass (1820 ÷ 1880 MeV), for which the existence of the H could manifest itself in a new hadronic weak decay mode, the decay with a π^+ in the final state. The elementary reactions would be:

$$\Lambda + p \rightarrow H + \pi^+ \quad (9)$$

$$\Lambda + n \rightarrow H + \pi^0 \quad (10)$$

The resulting π meson would have, assuming for example a mass of 1850 MeV for the H , ~ 64 MeV for the decay (9), ~ 70 MeV for the decay (10). The important point

						${}^{16}_{\Lambda}\text{O}$ 13.0 p 6.7			
					${}^{14}_{\Lambda}\text{N}$ 12.17 p 2.42	${}^{15}_{\Lambda}\text{N}$ 13.59 p 8.97	${}^{16}_{\Lambda}\text{N}$ (13) n 10.2		
				${}^{12}_{\Lambda}\text{C}$ 10.80 p 9.25	${}^{13}_{\Lambda}\text{C}$ 11.69 Λ 11.69	${}^{14}_{\Lambda}\text{C}$ 12.17 n 5.43	${}^{15}_{\Lambda}\text{C}$ (13.6) n 9.6	${}^{16}_{\Lambda}\text{C}$ (13) n 0.6	
			${}^9_{\Lambda}\text{B}$ 8.29 p 1.59	${}^{10}_{\Lambda}\text{B}$ 8.89 p 2.00	${}^{11}_{\Lambda}\text{B}$ 10.24 p 7.71	${}^{12}_{\Lambda}\text{B}$ 11.37 Λ 11.37	${}^{13}_{\Lambda}\text{B}$ (11.7) n 3.7	${}^{14}_{\Lambda}\text{B}$ (12.2) n 5.4	${}^{15}_{\Lambda}\text{B}$ (13.6) n 2.4
		${}^7_{\Lambda}\text{Be}$ 5.16 2p 0.7	${}^8_{\Lambda}\text{Be}$ 6.84 τ 5.31	${}^9_{\Lambda}\text{Be}$ 6.71 α 3.50	${}^{10}_{\Lambda}\text{Be}$ 9.11 n 4.07	${}^{11}_{\Lambda}\text{Be}$ (10.2) n 7.9	${}^{12}_{\Lambda}\text{Be}$ (11.4) n 1.6	${}^{13}_{\Lambda}\text{Be}$ (11.7) n 3.5	
		${}^6_{\Lambda}\text{Li}$ 4.50 p -0.6	${}^7_{\Lambda}\text{Li}$ 5.58 d 3.93	${}^8_{\Lambda}\text{Li}$ 6.80 t 6.15	${}^9_{\Lambda}\text{Li}$ 8.50 n 3.73	${}^{10}_{\Lambda}\text{Li}$ (9.1) n 4.6	${}^{11}_{\Lambda}\text{Li}$ (10.2) n 0.3		
	${}^4_{\Lambda}\text{He}$ 2.39 Λ 2.39	${}^5_{\Lambda}\text{He}$ 3.12 Λ 3.12	${}^6_{\Lambda}\text{He}$ 4.18 n 0.17	${}^7_{\Lambda}\text{He}$ 5.23 n 2.92	${}^8_{\Lambda}\text{He}$ 7.16 n 1.49	${}^9_{\Lambda}\text{He}$ (8.5) n 3.9			
	${}^3_{\Lambda}\text{H}$ 0.13 Λ 0.13	${}^4_{\Lambda}\text{H}$ 2.04 Λ 2.04	${}^5_{\Lambda}\text{H}$ (3.1) n -1.8	${}^6_{\Lambda}\text{H}$ (4.2) 2n .06	${}^7_{\Lambda}\text{H}$ (5.2) 3n 0.4				

Figure 6: Chart of light Λ -hypernuclei with binding energies B_{Λ} and particle instability thresholds ([from Ref. 24]). The neutron rich hypernuclei observable in (K_{stop}^-, π^-) reactions are indicated with \spadesuit .

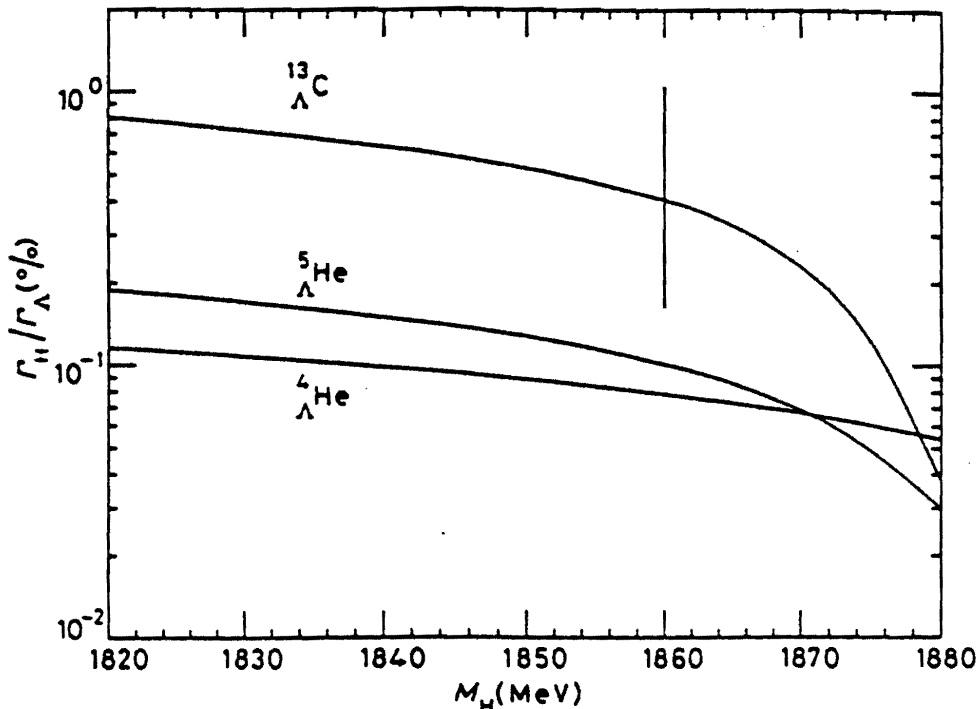


Figure 7: Decay rate of π^+ mesonic decay as a function of the H mass, for the hypernuclei ${}^{13}_\Lambda\text{C}$, ${}^5_\Lambda\text{He}$ and ${}^4_\Lambda\text{He}$. The ordinate scale is in (%) of the total decay rate (from Ref. [29]).

in the Kishimoto's observation is that the presence of monochromatic π^+ following the decay of hypernuclei would be a unique signature for the existence of the H and would at the same time provide a measurement of its mass.

The decay (10), with a π^0 in the final state, is difficult, if not impossible, to utilize for this purpose, since conventional mesonic decay modes, though strongly suppressed as discussed in Sec. 2.2, are competing.

Kishimoto evaluated the rates for the decay (9) and the results are shown by Fig. 7, as a function of the H mass, for ${}^{13}_\Lambda\text{C}$, ${}^5_\Lambda\text{He}$ and ${}^4_\Lambda\text{He}$. The obtained π^+ decay rate is $\sim 10^{-2} \div 10^{-3}$ of that of free Λ decay when the H mass is below 1870 MeV, a value within the reach of FINUDA.

2.5 The puzzle of Σ -hypernuclei

The discovery of narrow peaks (a few MeV) in production reactions (K^- , π^-) with K^- of 720 MeV/c, that could be kinematically interpreted as due to the formation of narrow Σ -hypernuclear states, was quite surprising. In fact, though the Σ -hyperon for many aspects is similar to the Λ - one concerning the lifetime and the interaction strength with nucleons, it was believed that its behaviour in nuclear matter was completely different. In fact, if Λ decay in nuclear matter proceeds through a weak interacting process ($\Delta S = 1$),

then the Σ can decay through the strong interacting process ($\Delta S = 0$) $\Sigma + \mathcal{N} \rightarrow \Lambda + \mathcal{N}$. The width of the Σ -hypernuclear states was therefore expected to be a few tens of MeV. Following the first experiments at CERN [30] and AGS [31] which claimed the unexpected presence of narrow Σ -hypernuclear states in (K^-, π) reactions with K^- in flight ($400 \div 720$ MeV/c) an even most striking evidence came from an experiment with K^- at rest, performed at KEK [32]. However, further high statistics studies, always at KEK, did not show evidence for the existence of Σ -hypernuclei, apart, perhaps ${}^4_\Sigma\text{He}$. A clear-cut answer to this intriguing puzzle is urgently needed. A recent review on the theoretical and experimental aspects of Σ -hypernuclei can be found in Ref. [11].

2.6 K^+ -Nucleus total cross section

It is known that, among meson probes, the K^+ holds a very special position. The K^+ meson contains a strange anti-quark and since there are no (valence) strange quarks in the nucleon, quark-antiquark annihilation is strongly suppressed. Thus K^+ cannot couple strongly to a 3-quark object and the $K^+\mathcal{N}$ system has no known resonance below 1 GeV/c. For this reason the $K^+ - \mathcal{N}$ interaction has two important properties: it has a weak energy dependence and a weak strength. Below 1 GeV/c the typical $K^+ - \mathcal{N}$ cross-section (9 mb) is about an order of magnitude smaller than the $\pi^- - \mathcal{N}$ and $K^- - \mathcal{N}$ cross section in the same momentum region.

A small cross-section means a long mean free path (~ 7 fm) for propagation of the K^+ in the nuclear medium. Therefore, unlike other hadrons whose mean free path is $1 \div 2$ fm, the K^+ is capable of probing the entire volume of the nucleus (it may be considered a sort of "heavy electron") and the complexity inherent in understanding the other strongly absorbed probes is avoided. Indeed, to first order, the K^+ -Nucleus interaction can be viewed as a single scattering of the K^+ with a nucleon and only small and calculable corrections to this picture are needed.

Given the properties of the K^+ as a "clean" probe, it was a surprise to find experimentally [33] that the ratio:

$$\mathcal{R} = \frac{\sigma(K^+{}^{12}\text{C})}{6\sigma(K^+d)} \quad (11)$$

of the cross-section for K^+ scattering on ${}^{12}\text{C}$ and deuterium is > 1 , at least at momenta $p_L > 600$ MeV/c.

This discrepancy should be considered significant and has been interpreted [34] as an indication of the "swelling" or "partial deconfinement" of the nucleon inside nuclei. It

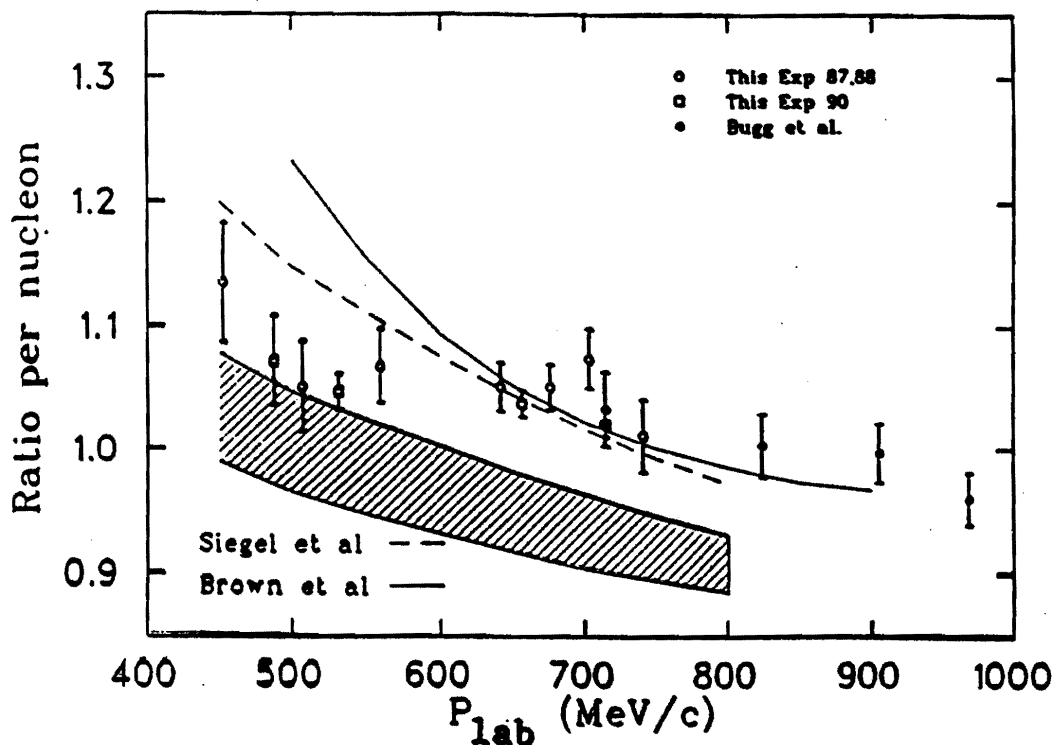


Figure 8: Experimental and theoretical values of \mathcal{R} [Ref. 33]. The shadowed band between solid lines corresponds to no “swelling” within the theoretical uncertainties. The dashed and continuous lines correspond, respectively, to calculations done with a 10% increase in the s-wave phase shift ($\delta R/R = 0.1$) and a density dependent rescaling effect with $const = 0.1$.

was argued that a possible “swelling” of nucleons in nuclei might lead to an increase in magnitude of the dominant $K^+ - \mathcal{N}$ s-wave phase shift:

$$\delta(I = 1, \text{ s-wave}) = -k(R + \delta R) \quad (12)$$

R being the nuclear radius.

Weise [35] considered this effect in the context of the more general concept of scale changes in nuclei, through a density-dependent rescaling of constituent quark (and hadron) masses according to:

$$\frac{m_q^*(\rho)}{m_q(0)} = 1 - const \frac{\rho}{\rho_0} \quad (13)$$

with $const \sim 0.1 \div 0.2$, with a corresponding renormalization of the (vector meson dominated) s-wave $K^+ - \mathcal{N}$ amplitude.

In Fig. 8 the experimental and theoretical values of \mathcal{R} are reported [33]. The shadowed band between solid lines corresponds to no “swelling” within the theoretical uncertainties. The dashed and continuous lines correspond, respectively, to calculations done with a 10% increase in the s-wave phase shift ($\delta R/R = 0.1$) and a density dependent rescaling effect with $const = 0.1$.

As seen, neither of these models is able to well reproduce the experimental points.

It is clear that such an "EMC-like" effect should be further investigated, for several nuclear target and in particular at low (< 400 MeV/c) momenta, for which the ratio \mathcal{R} seems to assume larger discrepancies with the expected value $\mathcal{R} = 1$.

2.7 $K\mathcal{N}$ scattering at low energy and the σ -term

There is at present substantial interest in the strangeness content of the nucleon. This interest has largely arisen because there exist discrepancies between several experimental and theoretical results that seem to require a significant inclusion of strange quarks in normal nucleons. The best known experimental results that point to this strange quark content in the nucleon are the long standing problem of the pion-nucleon σ -term [36] and the recent studies of the proton spin structure function by the European Muon Collaboration (EMC) [37].

QCD is presently accepted as the theory of strong interactions. The Lagrangian of QCD when constructed with the assumption that the quarks are massless, i.e. $m_u = m_d = m_s = 0$, is chiral symmetric. The current quarks of course are not massless, leading to acceptance of the idea that chiral symmetry is *spontaneously* broken and a quark mass term appears in the Lagrangian that is responsible for its *explicit* breaking.

The chiral SU(3) symmetry breaking operator is measured through the $\pi\mathcal{N}$ σ -term [36] which is determined using $\pi\mathcal{N}$ scattering data and data from pionic atoms. When analysed via a well accepted technique [38] the result requires a nucleon mass that is about 300 MeV too low. The very controversial solution to this problem is to assume that the nucleon contains a substantial amount of $\bar{s}s$ quarks even at hadronic scales. Such a solution to this discrepancy between experimental and theoretical results seems to indicate that the strangeness content of the proton could be as much as 10÷20%, very substantial considering that the conventional proton of the constituent quark model is pictured to contain no quarks other than those of the first generation, the up and the down.

The second experiment mentioned above also points to the need for a strange quark content in the nucleon. In it the EMC [37] used deep inelastic μ - p scattering to determine the fraction of the proton spin carried by each flavour. The results indicate that not only is the total amount of the proton spin carried by the light quarks approximately zero but that $\bar{s}s$ -pairs in the proton carry a significant fraction of its spin. This, as yet controversial result along with the $\pi\mathcal{N}\sigma$ -term results, impart substantial suspicion

upon our expectations as derived from the constituent quark model, an outcome that has become known as the spin crisis of the proton.

In addition to the above two experimental-theoretical controversies there exists a significant body of data from a variety of reaction studies that indicate that the Okubo-Zweig-Iizuka (OZI) rule [39] is violated for reactions involving nucleons. The reactions usually studied involve the production of the ϕ meson. The OZI rule implies that the amplitudes for processes involving disconnected (hairpin) quark diagrams should be vanishingly small. Thus if the ϕ is pure $\bar{s}s$ its coupling to hadrons containing no strange quarks should be highly suppressed. ϕ production in reactions such as $pp \rightarrow pp\phi$, $\pi^-p \rightarrow \phi n$ and $\bar{p}p \rightarrow \phi\pi^+\pi^-$ is thus expected to be very small compared to ω production. Ellis, Gabathuler and Karliner in a recent review [40] of the data on the ϕ/ω production cross sections found that in fact the ratio is larger than the OZI rule would dictate and argue that the strange quark content of the proton can be used to explain this "evasion" of the OZI rule. Henley, Krien and Williams [41] have carried the discussion one step further and suggested that ϕ production can be used as a measure of the strangeness content of the nucleon.

The resolution of the question whether the nucleon contains strange quarks or not is of fundamental importance because it relates directly to our understanding of how QCD is manifest at normal distances (~ 1 fm). It has been suggested by Jaffe and Korpa [42] that new data and an improved theoretical analysis of the $K\mathcal{N}$ σ -term is very important for the resolution of this puzzle. The provision of new data is necessary because the extraction of the $K\mathcal{N}$ σ -terms (isospin 1 or 0 being possible) from the presently available experimental data cannot provide an adequate test of the various model dependent predictions because at present the experimental errors are much too large [43].

The existence of very low energy kaons at DAΦNE (K^+ and K^- as well as the K^0 for which it is being built) will make possible a determination of the $K\mathcal{N}\sigma$ -terms. The DAΦNE kaons will be monoenergetic, essentially background free and because they occur in pairs from the decay of a ϕ meson will be tagged as to their direction in space. These features will allow for the measurements proposed here of K^+p and K^-p elastic scattering and $K^-p \rightarrow K^0n$ charge exchange reactions. These reactions will also be carried out using the deuteron as a target in order to obtain the same information for the neutron. No existing or planned facility will make possible measurement of $K\mathcal{N}$ interactions at the energies possible at DAΦNE.

In order to study $K\mathcal{N}$ scattering utilizing the DAΦNE low energy tagged kaon beams we are investigating the possibility of utilizing a solid hydrogen or deuterium target

inside the collider beam pipe. A solid hydrogen target up to 1 mm thickness held below 3 K under UHV conditions has been developed at TRIUMF for use in a muon catalyzed fusion experiment.

In the K - p scattering experiment, the target will be surrounded by layers of multi-layer silicon strip counter with 2 coordinate readout (see Sec. 4).

3 Production of Λ -hypernuclei

Neglecting for simplicity the hypernuclei production processes induced by antiprotons and relativistic ions, there are essentially two ways for producing and studying the hypernuclear spectra, with K^- beams and with π^+ beams. The larger amount of data has been produced so far by means of the strangeness exchange reaction:



on a neutron of a nucleus, which transfers the strangeness from the K^- to the struck neutron, transforming it into a Λ . The reaction kinematics of (14) shown by Fig. 9 (Feshbach-Kerman kinematics) has the specific feature that, with the π^- detected at 0° , there is in the laboratory frame a "magic" value of the K^- momentum for which the Λ -hyperon is produced at rest, and the π^- carries all the momentum. The momentum transfer is very small, 0 at the magic momentum (505 MeV/c), and can be varied in a controlled way by changing the beam momentum and/or the π^- emission angle.

Hypernuclear final states for which the Λ has the same spin and orbital wave function of the transformed neutron are the most copiously ones produced with (14). The cross-sections may reach values of the order of mb/sr.

Recently, the associated production reaction:



always on a neutron of a nucleus, was proved to be very efficient for producing Λ -hypernuclei at AGS. The kinematics of (15) is such that a relatively large momentum (~ 350 MeV/c) is transferred to the Λ -hyperon, always for forward detection of the K^+ . The cross-sections are then lower by at least two orders of magnitude than those for (14), but this drawback is overcompensated by the larger intensities of the π^+ beams. The hypernuclear final states produced by (15) are different than for (14): mainly high spin hypernuclear states are observed.

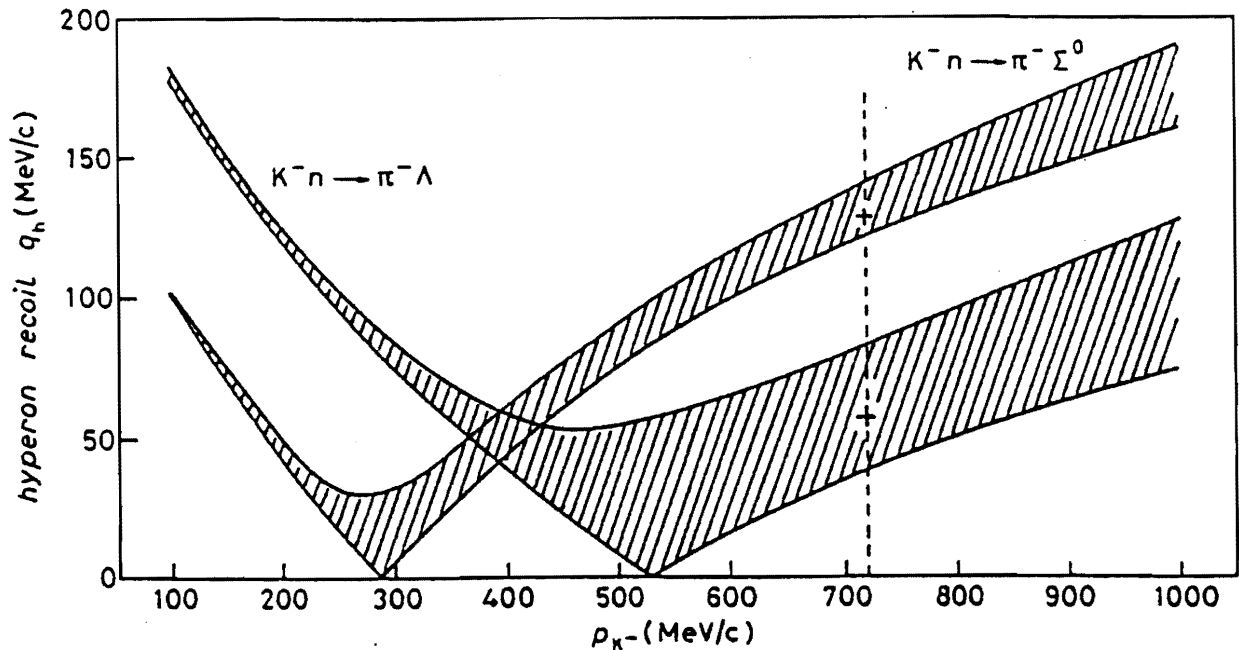
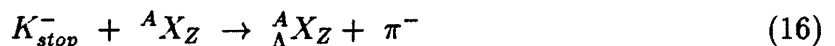


Figure 9: Kinematics in the forward direction for the Λ , and, respectively, Σ^0 production. The curves which limit the hatched areas downwards are for a π^- emission angle of 0° , those which limits upwards for 6° .

A way of combining the advantages of (14) and (15): high production rate and many hypernuclear final states, is that of using reaction (14) but with K^- at rest:



The momentum transferred to the produced Λ hyperon is of the same order of magnitude (250 MeV/c) than (15) and the production rates for defined hypernuclear final states are still quite high: 10^{-3} /stopped K^- . This technique was used very efficiently at KEK, where an impressive bulk of high quality data, with a lot of physics information was produced [44]. Fig. 10 shows a typical spectrum obtained at KEK with a ^{12}C target. The peaks at 273 MeV/c and 261 MeV/c are assigned as due to the ground state of $^{12}_\Lambda\text{C}$ and to the first excited state, of configurations $p_{(3/2)_n}^{-1} s_\Lambda$ and $p_{(3/2)_n}^{-1} p_\Lambda$ respectively. Concerning finally the production of neutron-rich hypernuclei, the reaction (14) with K^- at rest would be the most efficient, since the momenta of the produced π are very close to those corresponding to the Δ resonance, and then the charge exchange cross section is around its maximum value.

A similar production reaction than (14) holds for Σ^- hypernuclei, obviously replacing

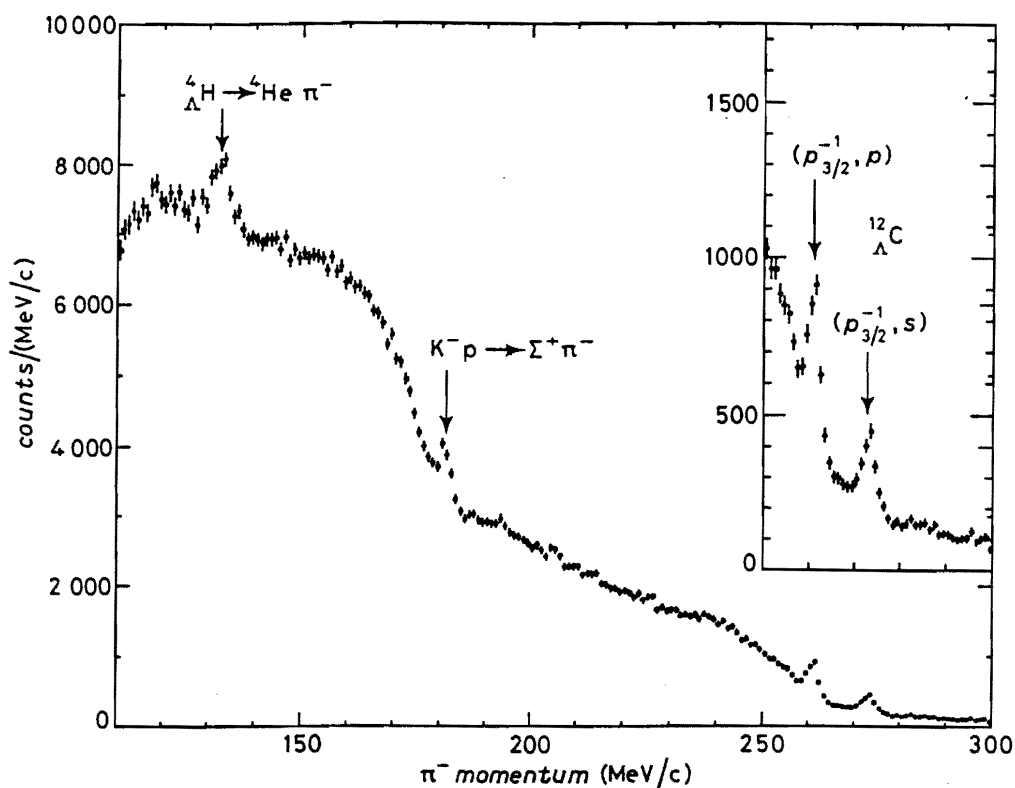


Figure 10: π^- spectrum from ^{12}C (stopped K^- , π^-) reaction measured at KEK. The insert shows on an expanded scale the high momentum region, corresponding to the production of $^{12}_{\Lambda}\text{C}$ in the excited and ground state (from Ref. [44]).

the appropriate mass for the Σ and remembering that the Σ hyperon has three states of charge and that a π^+ can be emitted in the case of Σ^- production. The pions from Σ -hypernuclei production have a momentum around $180 \div 200$ MeV/c, again depending on the target and the final state. However, we must recall that the most recent experiments with stopped K^- at KEK have seriously questioned the existence of narrow Σ -hypernuclei bound states, previously reported by the experiments performed with K^- in flight [30]. A clear-cut answer to this question would be a very important physics results from DAΦNE.

Finally, indirect population of Λ hypernuclei, in particular $^4_{\Lambda}\text{H}$, was observed with stopped K^- [45].

The $^4_{\Lambda}\text{H}$ production is again signalled by the monochromatic pion (133 MeV/c) emitted in the two-body mesonic decay:



Fig. 11 shows low-momentum regions of measured (stopped K^- , π^-) spectra on several

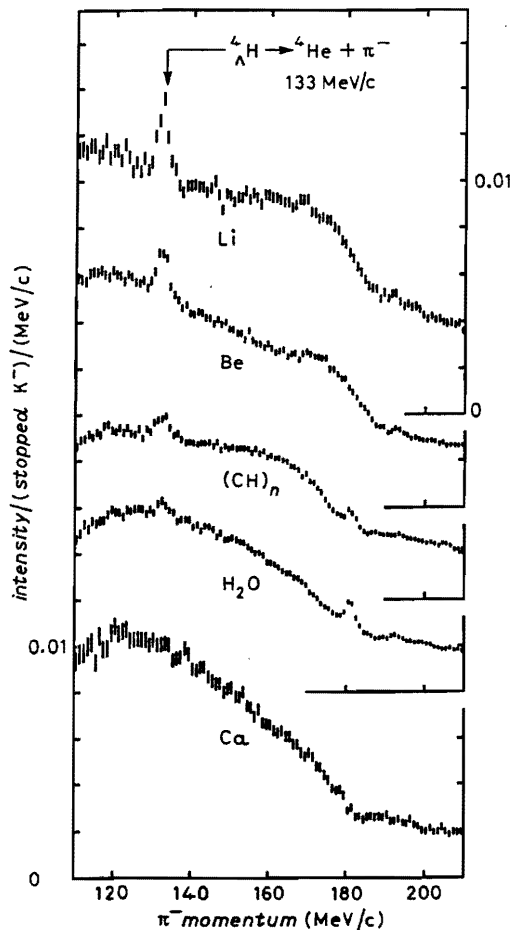


Figure 11: Low-momentum regions of (stopped K^- , π^-) spectra on several nuclear targets. The vertical scale of all spectra is the intensity per stopped K^- (from Ref. [45]).

nuclear targets.

What was surprising was not the observation of light hypernuclei production on heavy targets, already reported by old emulsion experiments, but the large production rate. It could not be explained by an α -cluster absorption mechanism, but perhaps by a model [44] in which a Λ generated by the $\Lambda\pi$ production or by the $\Sigma\mathcal{N} \rightarrow \Lambda\mathcal{N}$ conversion is trapped in the nucleus and forms a “ Λ compound nucleus”, which may decay into a hyperfragment such as ${}^4_{\Lambda}\text{He}$.

4 The FINUDA detector

4.1 General description

In this chapter we will describe the characteristic of a detector optimized for high-resolution spectroscopy of pions following the primary interaction of a K^- at rest with target nuclei, with simultaneous detection of other charged particles and neutrons. This detector will allow to perform the physics program from Sec. 2.1 to 2.5. With some modifications and/or using part of the apparatus also the physics program outlined in Sec. 2.6 and 2.7 could be performed. It is also conceivable that modifications of the detector system might allow also for high-resolution spectroscopy of π^0 , opening thus a new window on (K^-, π^0) reactions on nuclei, that produce the hypernuclei that are mirror of those produced in (K^-, π^-) reactions.

FINUDA is a non focusing magnetic spectrometer with cylindrical geometry. We based our design criteria on reasonable extrapolations of performances of present technology, with emphasis on detectors most of which we successfully used in previous experiments (see Appendix 1), optimized in order to have a large solid angle, the best momentum resolution and good trigger capabilities.

Fig. 12 gives a general view of the proposed detector, which consists of the following parts:

- 1) an interaction/target region;
- 2) an external tracking system;
- 3) an outer scintillator array.

The full apparatus is immersed into a solenoidal field, homogeneous within 1% over the volume used for the tracking of the charged particles. In the following we will assume a coordinate frame with the z -axis oriented along the (e^+, e^-) colliding beams direction, and oriented towards the e^+ beam, and the y -axis oriented perpendicularly to the floor. However, we will often refer to cylindrical (ρ, ϕ, z) coordinates. The (K^+, K^-) pairs used for physics are emitted from the interaction region, whose dimensions are assumed to be $\sigma_x = 0.2$ mm in the x direction and $\sigma_y = 0.02$ mm in the y one; along z , we assume a bunch-crossing region having a σ of 3 cm. We assume furthermore, at the maximum design luminosity $\mathcal{L} = 10^{33}$ cm⁻² s⁻¹, a bunch crossing frequency of 380 MHz, with an inter-bunch time of 2.6 ns. The (K^+, K^-) from ϕ decay follow a $\sin^2\vartheta$ law, ϑ being the angle relative to the z -axis.

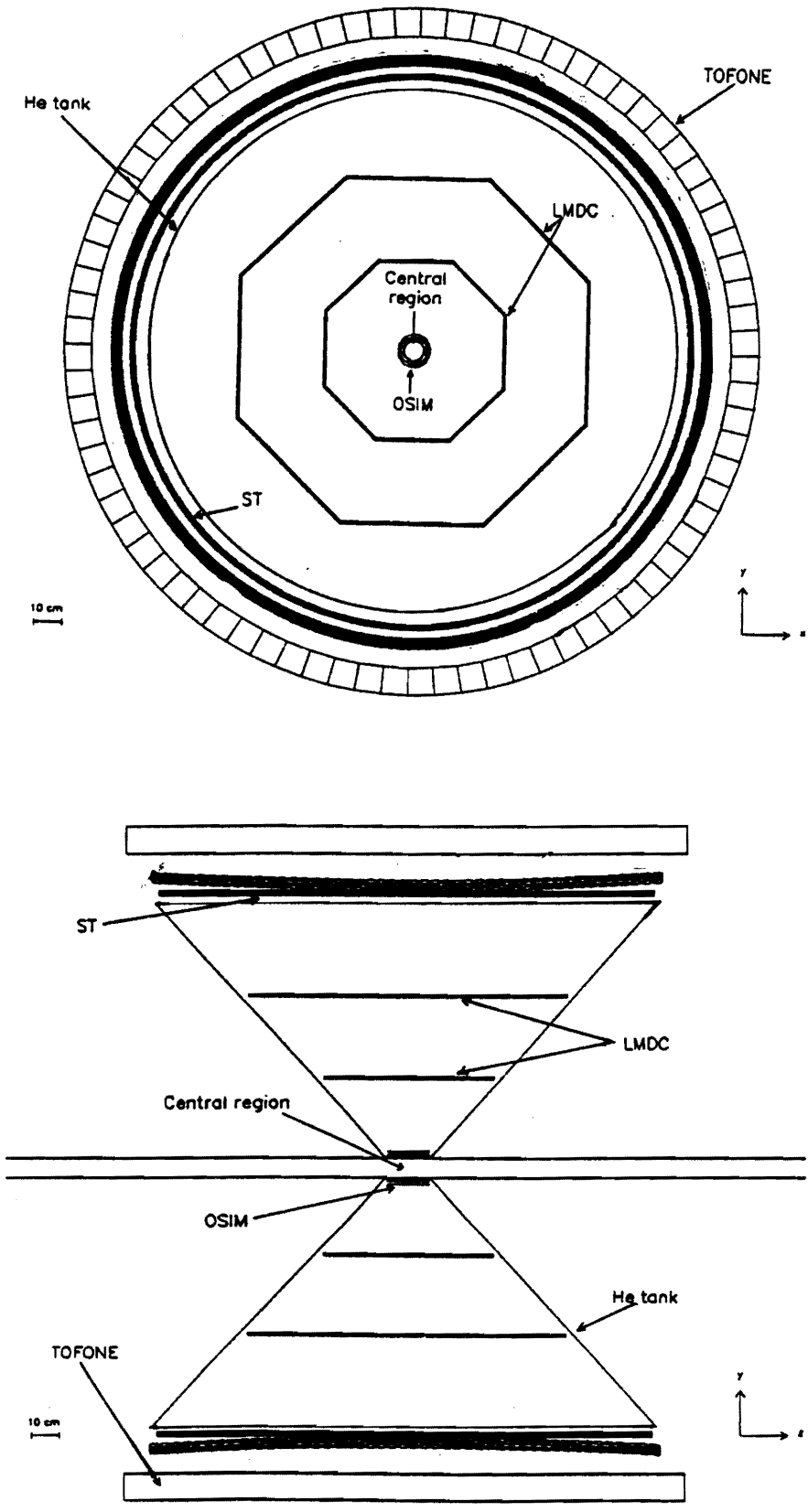


Figure 12: General view of the FINUDA detector.

In this section we will describe briefly the main tasks and expected performances of the various subdetectors located inside the magnet. The cylindrical interaction/target region of FINUDA consists of the beam pipe, a scintillator barrel (TOFINO), an internal polygonal Si microstrip array (ISIM) and the internal nuclear stopping target. Fig. 13 shows the two views of the proposed arrangement. For completeness we have indicated too the external (outer) polygonal Si microstrip array (OSIM) that however is a part of the external tracking system. The above arrangement must accomplish the following tasks:

- 1) the (K^+, K^-) pairs from ϕ decay have to be identified in a time fast enough to contribute to first level trigger;
- 2) the (K^+, K^-) coordinates before the nuclear target have to be measured;
- 3) the monochromatic K^- has to be stopped as near as possible to the external surface of the target.

Since the K^- from ϕ decay have an energy of 16.1 MeV, they cross, before stopping, a very reduced amount of material (e.g. 0.5 g cm^{-2} of ^{12}C). This fact represents the unique feature of DAΦNE that will allow hypernuclear spectroscopy with unprecedented resolution but it requires the design of very thin detectors before the nuclear target.

The fast scintillators are used for first level trigger allowing a topology selection of back to back events (K^+, K^- from ϕ decay at rest), a multiplicity information and $\Delta E/\Delta x$ measurement.

The position information from ISIM obtained with a σ of a few tens of microns will allow the reconstruction of the (K^+, K^-) trajectories. (We will refer to the rms deviation for the accuracy on the localization, whereas for energy and momenta spectra we will quote the FWHM.) This information, together with the measurement, in the external tracking system, of the trajectory of π^- emitted in the hypernuclear formation reaction, will allow the determination of the position of the stopping point of the K^- inside the thin target. The thicknesses needed for the inner detectors are determined by the requirement of stopping the K^- inside a target of thickness as close as possible to the diffuseness for the range due to its energy straggling, taking into account also the K^- angular distribution.

The proposed thicknesses are the following: $200 \mu\text{m}$ of Beryllium for the beam pipe, 1.5 mm for the scintillators of TOFINO, $300 \mu\text{m}$ for ISIM and finally about 1.5 mm for

a Carbon stopping target. In these conditions K^- emitted from 45° to 135° stop in the target volume.

The length of the interaction/target region is determined by the requirement of accepting all the (K^+, K^-) pairs emitted from 45° to 135° along z coordinate from -3.5 cm to $+3.5$ cm, which corresponds to the FWHM of the (e^+, e^-) interaction region. The resulting length of the stopping target will be 17 cm and will allow an acceptance for (K^+, K^-) of more than 90%.

With the above described assembly, a Monte Carlo calculation is used to evaluate the distribution of the stopping points of the K^- inside the thin target. Fig. 14 shows the radial distribution of the stopping points for the case of the carbon target; the effect of different K^- emission angles, energy straggling and multiple scattering are accounted for. The distribution shows a well defined peak, which can be used to perform a first order estimate of the π^- energy loss in the target.

The ISIM will allow the reconstruction of the trajectory of the (K^+, K^-) ; the intersection of this trajectory with that of the π^- measured by the external tracking system will give a reliable estimation of the point of formation of the hypernucleus inside the target thickness. The measured momenta of the emitted charged particles could then be corrected also for the energy lost in the already thin target obtaining a further improvement in the momentum resolution. Fig. 15 shows the effect of this correction on Monte Carlo simulated pions of 270 MeV/c (this value will be taken in the following as a typical one) and assuming a momentum resolution of the external tracking system of 0.3% FWHM.

The performance of the external tracking system is the most crucial since it will allow the measurement of the momenta of π^- emitted from the formation reaction (16). The momentum resolution enters directly into the determination of the hypernuclear energy levels. It is straightforward to see that, with M_H, M_A, M_π, M_K denoting the masses of the hypernucleus, target nucleus, π^- and K^- , the hypernuclear mass is given by:

$$M_H = M_A + M_K - M_\pi - T_\pi \quad (18)$$

neglecting the hypernucleus recoil energy. Then $\Delta M_H = \Delta T_\pi$ and

$$\frac{\Delta T_\pi}{T_\pi} = \frac{\sqrt{p_\pi^2 + m_\pi^2} + m_\pi}{\sqrt{p_\pi^2 + m_\pi^2}} \frac{\Delta p_\pi}{p_\pi} = f(p_\pi) \frac{\Delta p_\pi}{p_\pi} \quad (19)$$

The function $f(p_\pi)$ depends obviously on the hypernuclear final state, but in a rather smooth way. Taking as typical ${}^{12}_\Lambda\text{C}$ in the ground state from a target of ${}^{12}\text{C}$, we obtain

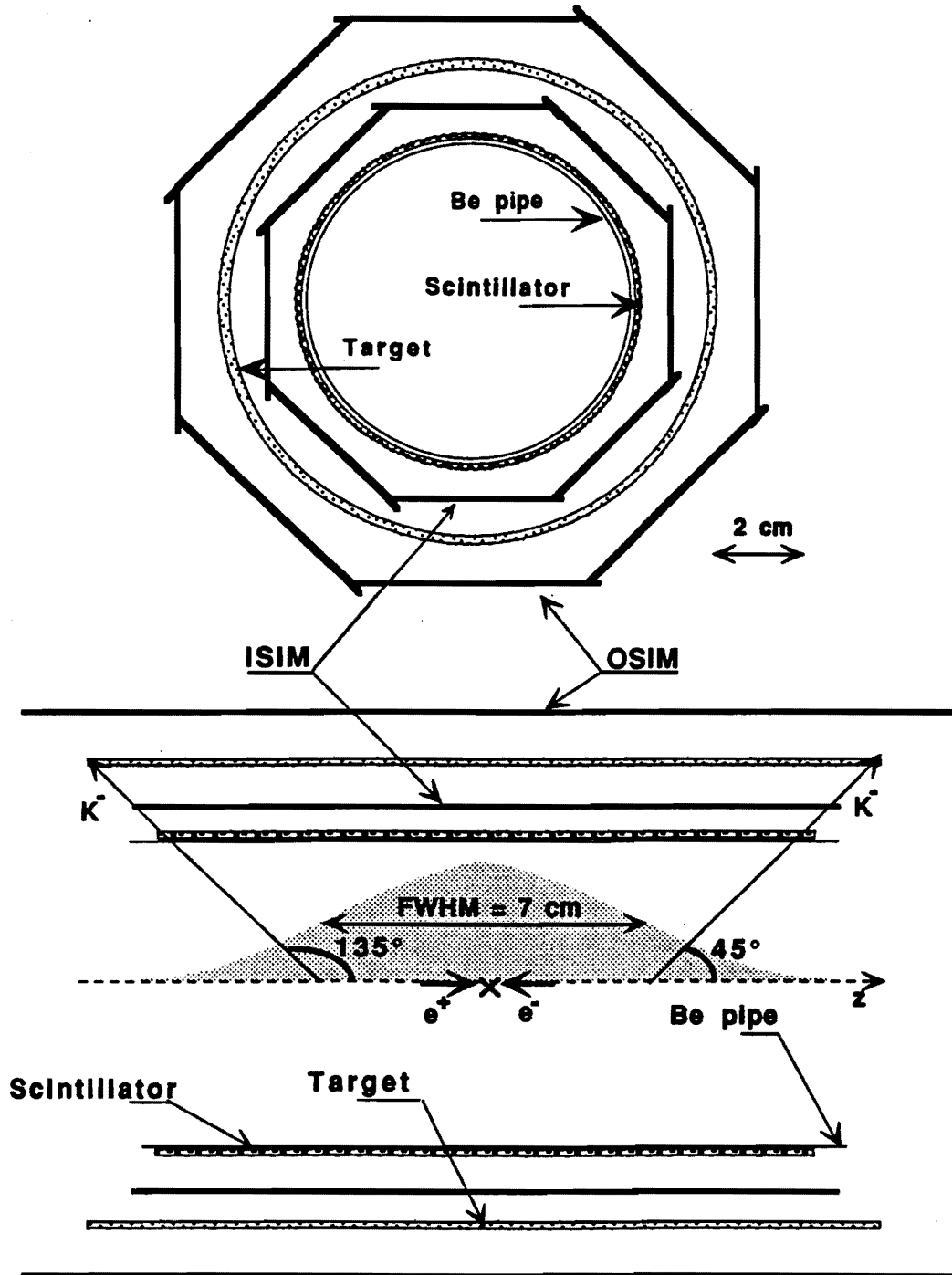


Figure 13: The two views of the proposed target/interaction region.

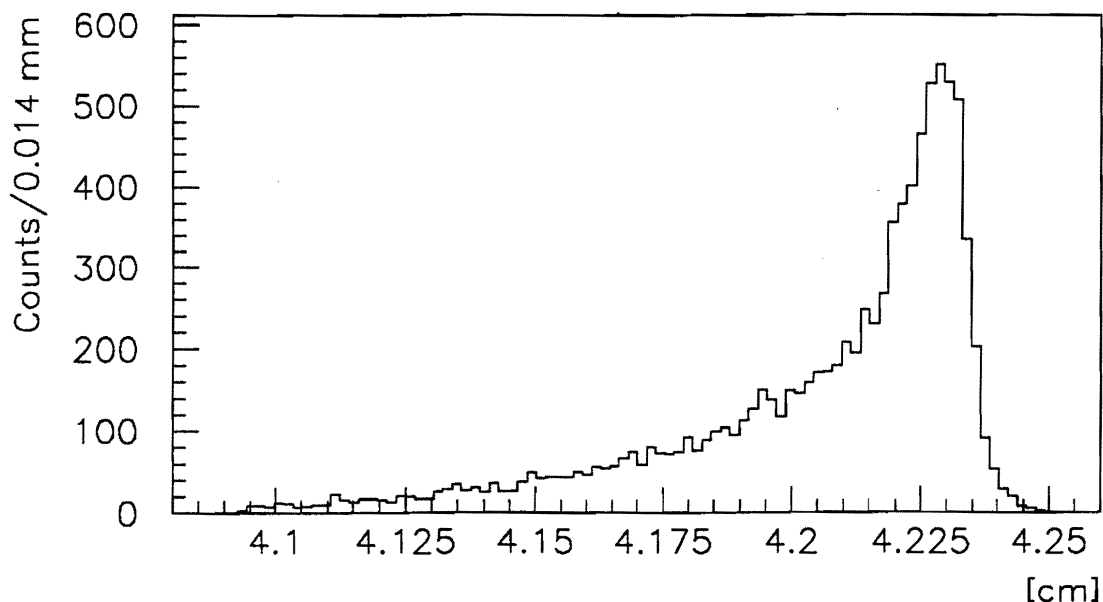


Figure 14: Radial distributions of the stopping points, as obtained in a MC simulation for a Carbon target.

from (16) $p_\pi = 272 \text{ MeV}/c$, $T_\pi = 166.2 \text{ MeV}$, and then, for this state $f(p_\pi)$ is 1.4. We may assume this value of $f(p_\pi)$ as a typical one. From (19) it is clear that each 10^{-3} in $\Delta p/p$ corresponds to 236 KeV in the energy resolution for the hypernuclear levels.

The minimum information required for the reconstruction of a charged particle trajectory in an almost uniform magnetic field is represented by three points along its path. Factors affecting the momentum resolution are the multiple scattering due to materials along the particle path and the spatial resolution in the determination of the measured points.

The solution we have chosen is that of high spatial resolution low mass detectors immersed in a helium atmosphere to minimize multiple scattering.

The requirement of low mass is particularly stringent on the detectors located along the particle trajectory and can be partially released for the detectors measuring the initial and final point of the tracks.

To better face the pattern recognition problem we decided furthermore to measure four points for each track.

The first point on the track is given with accuracies of the order of $30 \mu\text{m}$ by the OSIM array which is the first track localizing device that the particle encounters. The

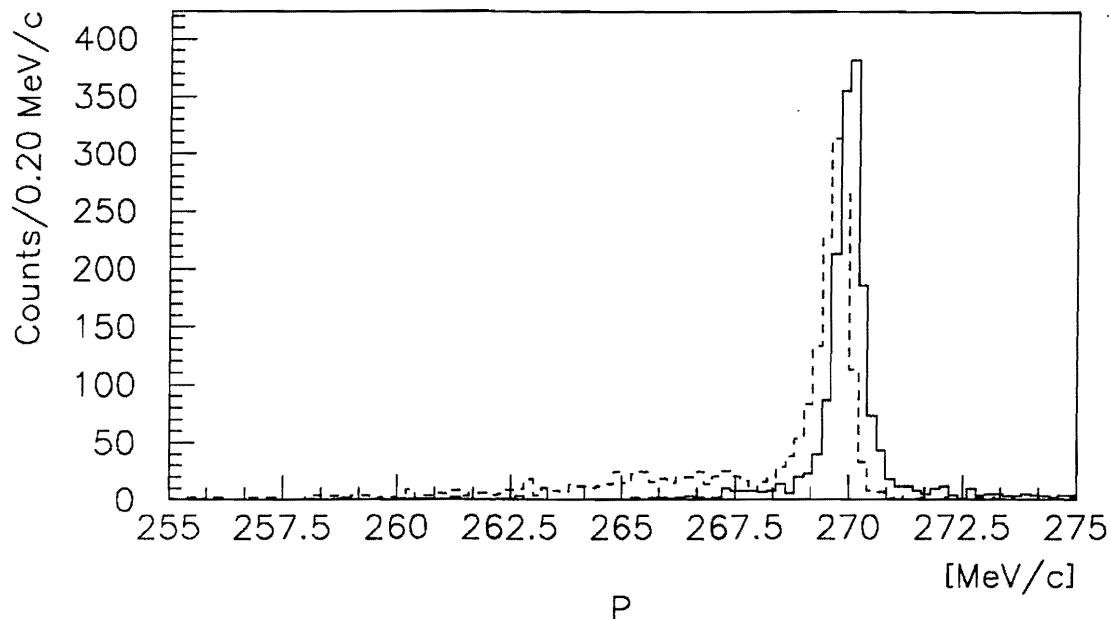


Figure 15: MC simulation of the effect of the “tagging technique” on the π^- reconstructed momentum spectrum. π^- momentum distribution with (solid line) and without (dotted line) corrections.

last point is given with an accuracy of $50 \mu\text{m}$ in the (ρ, φ) plane and about $300 \mu\text{m}$ in zeta coordinate by an array of straw tubes (ST). The substantial advantage of using ST for the measurement of the last point is that the spatial resolution is independent of the incidence angle of the track.

Two internal points are measured by low mass drift chambers (LMDC) providing a resolution of $100 \mu\text{m}$ in the (ρ, φ) plane and a much more coarse resolution (1% of the wire length) in the zeta coordinate obtained by charge division.

Taking into account the minimum amount of materials for these chambers as described in Sec. 4.5 and the quoted spatial resolutions we obtained by Monte Carlo simulation a momentum resolution of about 0.2% FWHM for pions of 270 MeV/c, as shown in Fig. 16.

We considered also the option of a Time Projection Chamber (TPC) providing good intrinsic spatial resolution, good pattern recognition and that in addition would also give us information on $\Delta E/\Delta x$. However the Monte Carlo simulation of the performance of such a device showed that the maximum momentum resolution attainable is of the order of 1.4% FWHM as shown by Fig. 17. The reasons for such unsatisfactory behaviour are

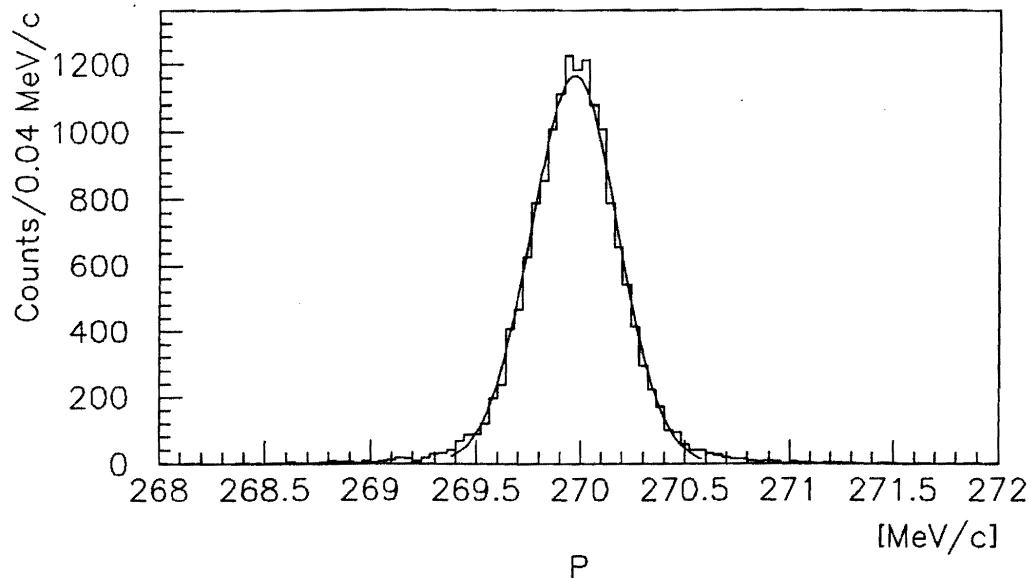


Figure 16: Momentum resolution with a tracking device based on LMDCs, as obtained by a MC simulation, for 270 MeV/c pions.

the high curvature of low momentum tracks and the need of thick entrance walls.

The outer scintillator array (TOFONE) will be used for first level trigger and for neutron detection.

4.2 Internal scintillator barrel (TOFINO)

The 1.5 mm thick, 14 cm long inner scintillator barrel (TOFINO) will be segmented in 12 strips, 1.8 cm wide each, subtending a $\Delta\varphi$ of 30° .

A greater segmentation would produce losses due to the bending of (K^+ , K^-) inside the pipe and to the dead zones between adjacent strips.

The calculated $\Delta E/\Delta x$ in the scintillators for (K^+ , K^-), (π^+ , π^-), (μ^+ , μ^-) and (e^+ , e^-) of momenta foreseen at DAΦNE are shown in Fig. 18 taking too into account the angular dependence.

As it can be seen, there is a large separation in energy lost by kaons from that by pions, muons and electrons. The non-linear relationship between light output and energy loss will introduce a small correction.

The scintillators will be seen from one side by phototubes (PMs) put outside the magnetic field through 200 cm long properly shaped light guides. This solution against the

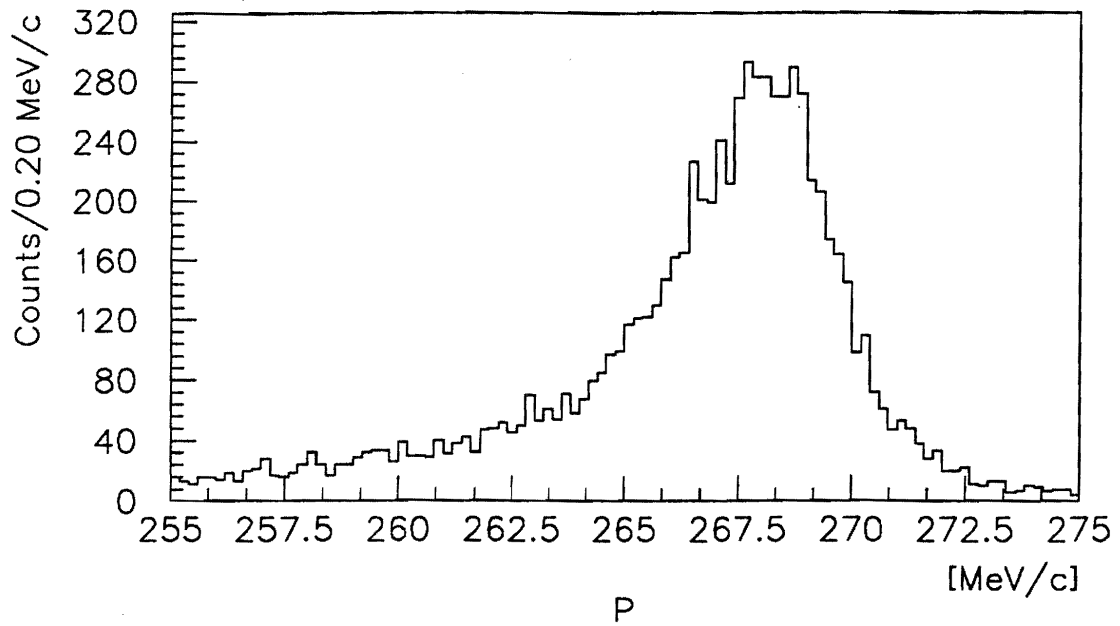


Figure 17: Momentum resolution with a TPC based tracking device, as obtained for a MC simulation, for 270 MeV/c pions.

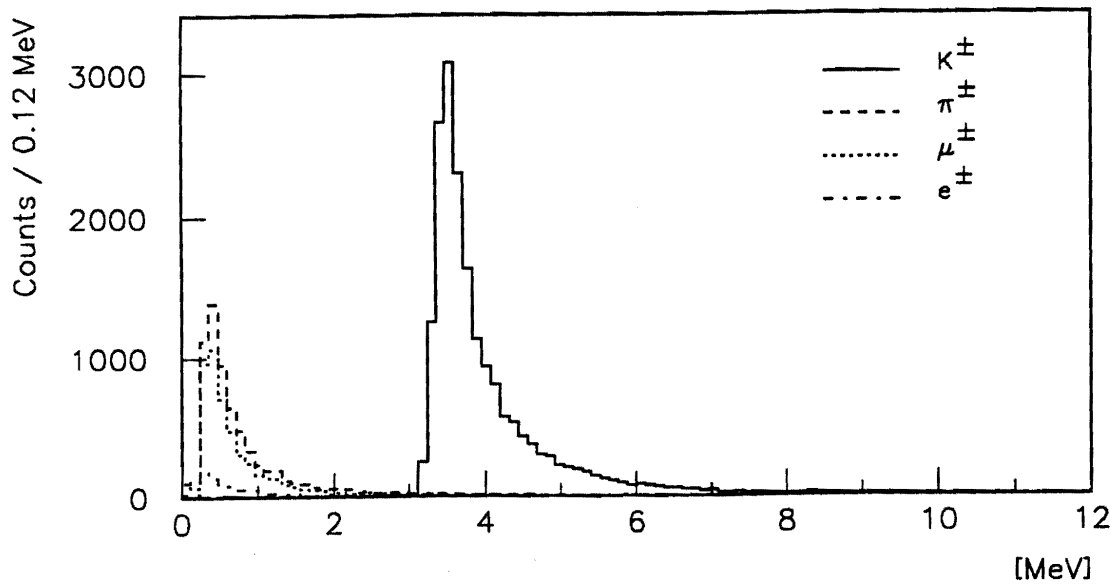


Figure 18: ΔE in internal scintillator (1.5 mm thick) for different particles.

usual two sides viewing is due mainly to mechanical reasons, to allow an easy extraction of the detector from the solenoid.

The inconvenience of one side light collection is twofold: an inhomogeneity of the response and different arrival times of scintillation light depending on the impact point of particles along the length on the slab. The response inhomogeneity (about 10%) is small however compared to the angular spread effect.

To overcome the second point, a method described in Sec. 4.9, will allow the definition of a good trigger time and a good START signal for TOF and tracking devices.

All the individual scintillators of TOFINO will obviously be instrumented by ADC and TDC channels. Protons from non-mesonic decay of hypernuclei (Λ) will be detected by TOFINO with solid angles close to π (see Fig. 13) and then we could measure directly τ_Λ in hypernuclei following the technique already used at BNL [15]. We will measure the time spectrum of events recorded in a slab different than those which detected the (K^+ , K^-) pair. Prompt π^- ($250 \div 270$ MeV/c) corresponding to the formation of ground state of hypernuclei must exhibit a symmetrical time distribution, with a width corresponding to the instrumental time resolution. On the contrary charged particles (protons, eventually pions for light targets) emitted following the decay of hypernuclei must exhibit a time distribution showing an asymmetry just due to the fact that Λ follows an exponential decay time law, with a decay constant given by τ_Λ . The experimental capability of observing such an asymmetry is related to :

- 1) the instrumental time resolution of each slab of TOFINO;
- 2) the precision in the alignment in time of the different slabs;
- 3) the electronic stability of the full system;
- 4) a careful off-line correction of the measured times in order to take into account the different paths of particles hitting TOFINO; the correction can be performed by means of the localization information from ISIM.

If we were able to obtain at the end a time resolution of $250 \div 300$ ps FWHM, we could measure the asymmetry and then τ_Λ . Fig. 19a shows a MC simulation of the time distribution of events following an exponential decay distribution with $\tau_\Lambda = 100$ and 200 ps respectively. The prompt event distribution ($\tau_\Lambda = 0$) is also shown for comparison. An instrumental total time resolution of 300 ps FWHM was assumed. The distributions are not corrected for the different path lengths of the particles. Fig. 19b shows the

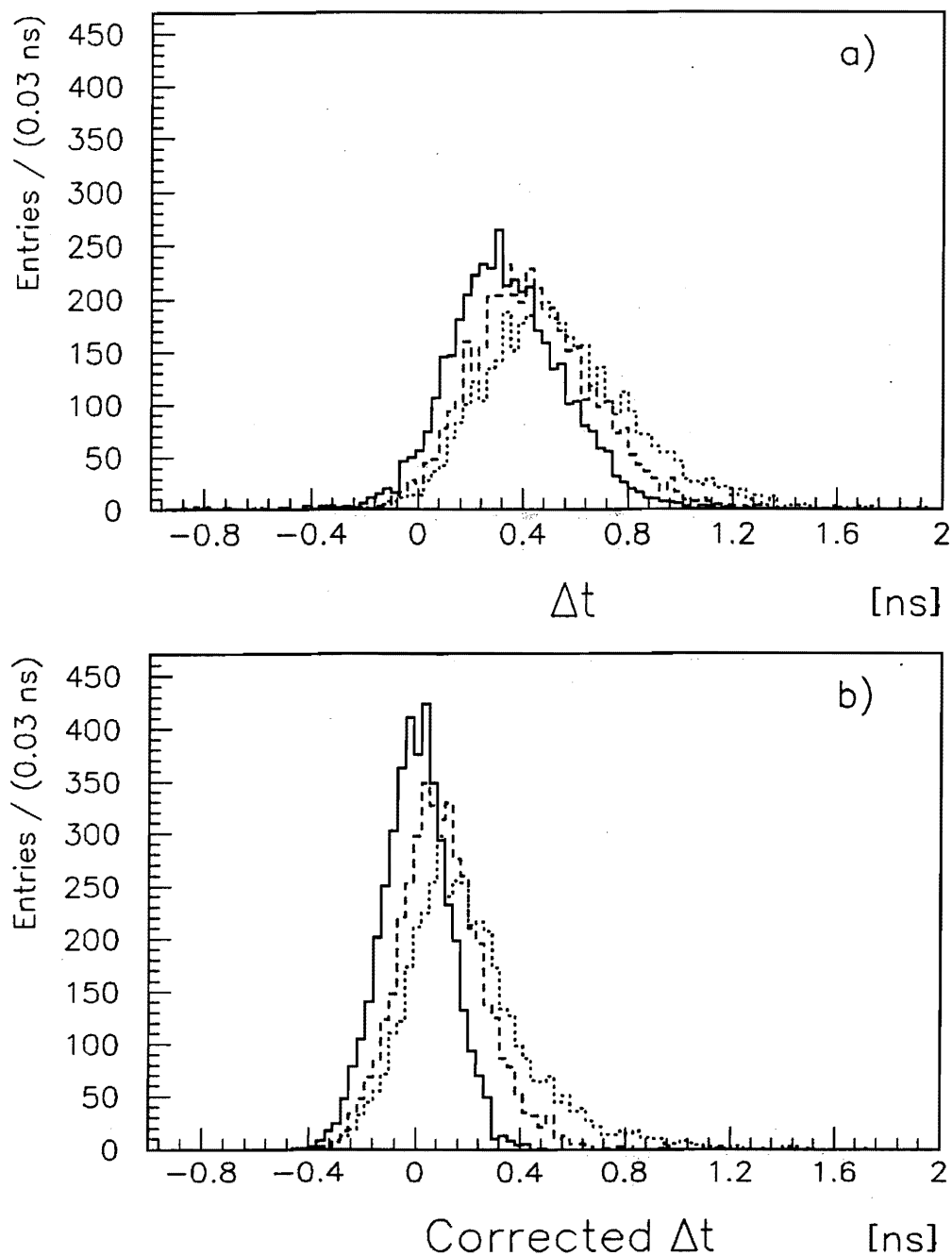


Figure 19: a) Time distribution of events recorded by TOFINO due to proton stimulated non-mesonic decays. The dashed and dotted lines refer to $\tau_A = 100$ and 200 ps respectively. The solid line shows the time distribution for prompt events ($\tau_A = 0$). The distributions are not corrected for the different path lengths. b) Same than a), but with corrections for the different path lengths.

same distributions, suitably corrected for the different path lengths as measured by the tracking devices, in the same hypotheses. It can be seen that with $\sim 10^3$ events in the distributions, an error of ± 5 ps on τ_A will be obtained.

We are designing a prototype for a careful study of the instrumental time resolution. We are also evaluating which PM offers the best performances with the further requirement of working into a stray magnetic field greater than 0.1 T.

The proposed scintillator material is NE102A, which is fast (2.4 ns), with high light output and highly radiation resistant. The selected PMs will be XP2020 or PMs with similar performances.

4.3 The Silicon microstrip detectors

Two silicon micro-strip arrays (ISIM and OSIM) will sandwich the target (see Fig. 13).

The OSIM (Outer Silicon Microstrip) cross-section is an octagon and, in this arrangement, the sensitive area is about 80% of the total area. Each face comprises 4 double-sided micro-strip wafers, and each of them is 4.5 cm wide, 5 cm long and 300 μm thick. Couples of wafers will have longitudinal micro-strips welded together, such as to form a wafer 4.5 cm wide and 10 cm long. The surface covered by a face will be $4.5 \times 20 \text{ cm}^2$. Signals will be processed at the two extremities of each face. The momentum resolution required for the external tracking system requires a spatial resolution of about 30 μm in (ρ, φ) plane and zeta coordinate. In turn, this spatial resolution dictates the size of the micro-strip pitch (50 μm) and the pitch distance (20 μm) for both faces of each wafer. Every second (or third) strip will be instrumented with readout electronics. The process of reading one out of two (three) strips will improve the spatial resolution, but at the expenses of an increased noise since the total charge will be shared between two (three) strips. The ratio of a signal induced by a minimum ionizing particle to noise will establish the optimum number of instrumented channels.

The ISIM (Inner Silicon Microstrip) detector is very similar to the OSIM detector with an octagonal cross section. Each of the eight faces consists of two double-sided silicon micro-strip wafers, covering a surface of $3 \times 15 \text{ cm}^2$. Wafers of ISIM array will have the same characteristics as the OSIM wafers, namely, pitch and pitch distance will be 50 μm and 20 μm , respectively. Signals will be processed at the two extremities of each face.

The (total) thickness of the wafer should not exceed 200 μm in order to keep the K energy loss below 2 MeV, regardless the angle of emission of kaons. The vertices due to

negative kaons stopping into the target and prompt pions leaving the target will determine the penetration depth of kaons in the target. In turn, the kaon penetration depth can be related, through the target thickness, to the amount of material (g/cm^2) that prompt pions must traverse before emerging from the target, and the latter quantity to the pion energy loss, ΔE_π , through dE/dx curves. In absence of tracking devices, for a Carbon target 1.5 mm thick, ΔE_π is as large as 0.5 MeV for a pion kinetic energy of 164.4 MeV ($p_\pi = 270 \text{ MeV}/c$), hence affecting the final momentum measurement. The hypernuclear reaction vertex will be measured with an accuracy of $\sim 150\mu\text{m}$, length comparable with the average range straggling of kaons in the target. The silicon micro-strip wafers that will equip both ISIM and OSIM detectors are commercially supplied [46].

For each wafer, the charge collected by the transversal (with respect to the zeta direction) micro-strips will be busted outside of the detector with kapton readout cables. This technical solution is spurred by the necessity of maintaining the effective thickness of ISIM and OSIM below $300 \mu\text{m}$ and $400 \mu\text{m}$, respectively. We will likely use a standard design for the front-end electronics [47] and for the analog to digital conversion [48]. However, the low event multiplicity following ϕ decays, and the circumstance that the requirement of spatial resolution on ISIM may be somehow released without serious worsening of the performances of the apparatus has addressed the collaboration to study an alternative readout chain for ISIM (see Appendix 2) and also the possibility of employing a cylindrical microstrip gas chamber (GMSC) (see Appendix 3).

4.4 The targets

The nuclear targets of easier use are those which are solid at room temperature and isotopically pure. The last requirement is mandatory for high resolution experiments, in which a small (5÷10%) mixture of two or more isotopes may complicate the interpretation of the hypernuclear energy spectra.

We may then envisage the following classes of targets:

- 1) easy (solid, isotopically pure): ^9Be , ^{12}C (98.9%), ^{27}Al , ^{31}P , ^{45}Sc , ^{51}V , ^{55}Mn , ^{59}Co , ^{75}As (poison!), ^{89}Y , ^{98}Nb , ^{103}Rh , ^{133}Cs , ^{165}Ho , ^{181}Ta , ^{197}Au , ^{209}Bi ;
- 2) feasible (flammable solids, to be sealed off, or elements isotopically enriched): ^6Li , ^7Li , ^{10}B , ^{11}B , ^{23}Na , ^{40}Ca (97%);
- 3) difficult, but very interesting (from the physical point of view): ^3He , ^4He (cryogenic targets or solid targets inside the beam pipe).

4.5 Low mass drift chambers (LMDC)

High accuracy drift chambers (HADCs) have been successfully operated reaching a spatial resolution of less than $50 \mu\text{m}$ [49]. Fig. 20 shows a cross section of a HADC.

A uniform drift field is obtained by sandwiching sense and field wires between two cathode planes made by equidistant wires at increasing potentials. This field is bound by low mass ground planes on both sides. We will call this structure the standard HADC. Reliably stable operation of these chambers has been demonstrated with argon-isobutane (75%-25%) as gas mixture, working in the saturated drift velocity mode. Very large HADC ($4 \times 2 \text{ m}^2$) have been operated for years in the Omega detector at CERN. The different voltages at which cathode wires have to be set can be supplied by orderly connecting wires to a fan out. For operation in magnetic field the drift field lines must be tilted in order to compensate for the Lorentz angle of the drifting electrons.

The z-coordinate is given by current division along the anode wires, accuracies of the order of 1% of the wire length are usually obtained with the best achieved value of $\sim 0.4\%$; in addition this method has the advantage of measuring the drift time twice, thus improving the localization accuracy. The solution of the left-right ambiguity is obtained replacing the anode wire by a pair of wires with a $200 \mu\text{m}$ separation. This gives an unambiguous signal determining the side where the track crosses the cell with a small efficiency loss (less than 1%) in the region between two anode wires. The drift cell length will be of about 2.5 cm. Typical design parameters are given in Tab. 3.

Fig. 21 shows schematically the arrangement of the two LMDC layers (I and II) around the interaction region.

To reduce multiple scattering due to the wires, the cathode planes in an optional and advanced LMDC structure [50], (cross section shown in Fig. 22), would consist of thin plastic foils ($\sim 10 \div 15 \mu\text{m}$) with cathode strips ($\leq 1 \mu\text{m}$ thick, 1 mm apart) printed on. In addition we would use a low mass gas mixture as will be discussed in the following.

Our baseline option is the widely used HADC. In addition we will continue R&D for the LMDC, concerning the chamber gas and materials which have to be optimized. In the HADC low energy particles crossing the cathode wires are affected by a large multiple scattering angle, for this class of tracks the momentum resolution is bad. For the four planes of cathodes in HADCs I and II, about 20% of the tracks are affected. It is clear the advantage of using the cathode foils in LMDC. For both chambers we expect to obtain a localization accuracy of $100 \mu\text{m}$ for tracks normal to the chamber surface. This resolution will worsen linearly with the angle of incidence reaching $150 \mu\text{m}$ for 45° .

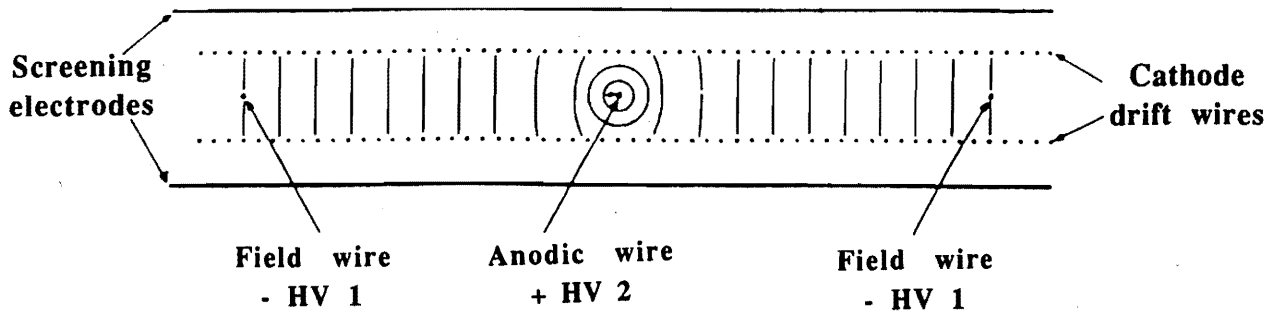


Figure 20: Cross section of HADC.

The requirements of gas mixtures for both HADC and LMDC are the following: they should have a large radiation length to minimize multiple scattering, should provide a large number of primary ion pairs (N_p), and have a low diffusion coefficient; furthermore a small Lorentz angle is requested to avoid distortions due to the $\vec{E} \times \vec{B}$ effects. The drift velocity should ideally be saturated. If not it can be anyway compensated for by a uniform drift electric field and on-line calibrations of the space-drift time relationships. In addition, the operation characteristics of the chambers with the chosen gas mixtures should be stable with respect to contamination of helium from the helium tank. It is also desirable that the gas mixture is well quenched, transparent to background γ radiation.

A (70%-30%) gas mixture of helium-dimethyl ether (He-DME) satisfies almost all the above requirements. The radiation length of this mixture is 674 m, ~ 6 times more than argon-based mixtures. N_p for this mixture is 21, sufficient to obtain the resolutions we estimate. Finally this mixture has shown excellent gas amplification properties, and spatial resolutions of $\sim 100 \mu\text{m}$ have been reported [51]. One limitation of DME is that it attacks certain materials used for construction of drift chambers. This limitation can

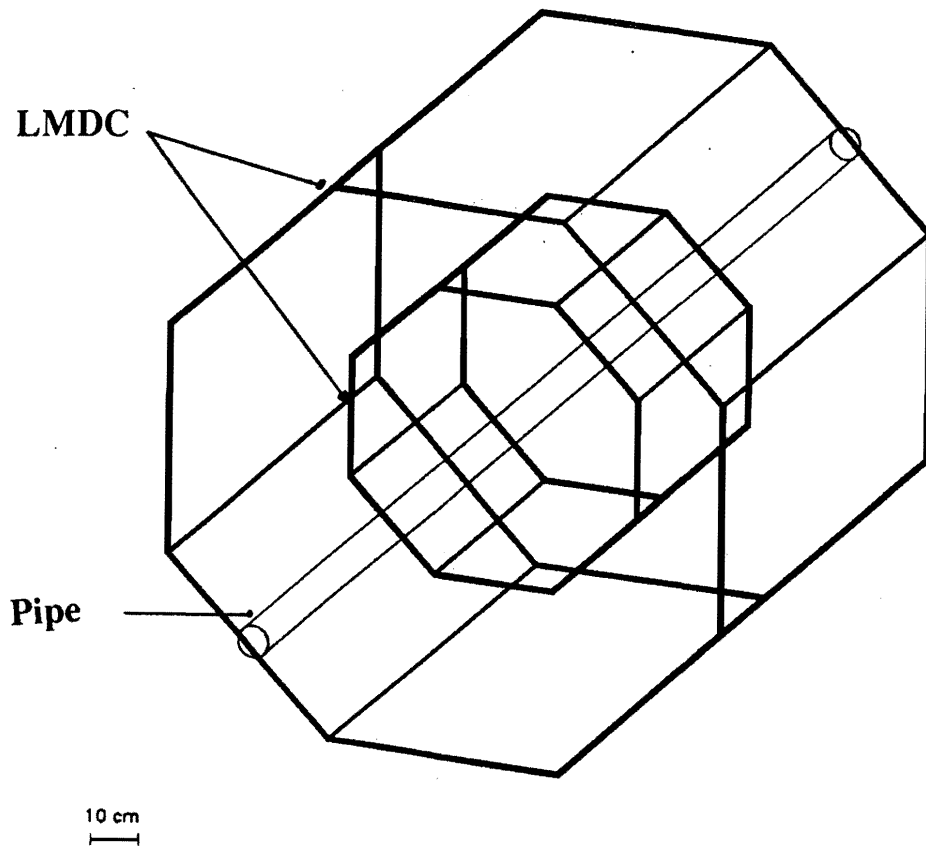


Figure 21: Arrangement of the LMDC modules.

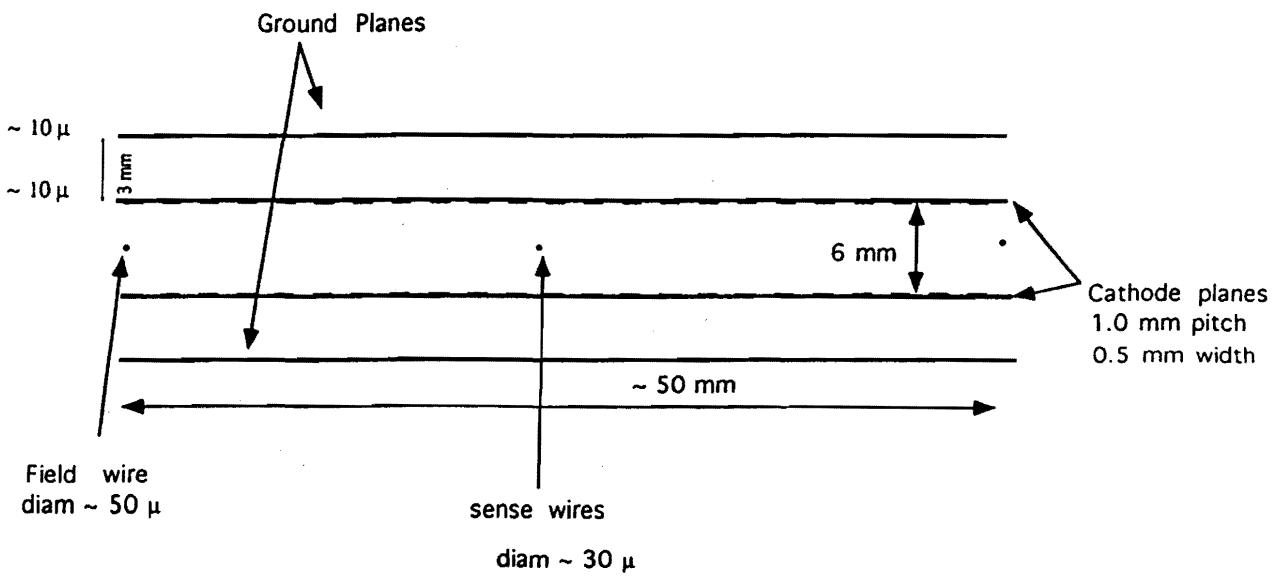


Figure 22: Cross section of LMDC.

Table 3: Typical design parameters of HADC/LMDC.

sense wire diameter	20 μm
sense wire pitch	50 mm
field wire diameter	50 μm
field wire pitch	50 mm
cathode wire diameter	50 μm
cathode wire pitch	1 mm
material of the ground planes	Upilex + 0.3 μm of Gold
thickness of the ground planes	10 μm
gas mixture	He-CO ₂ -DME(70%-25%-5%)
cathode foil material for LMDC	Upilex + 0.3 μm of Gold
width of cathode strips	0.5 mm
pitch of cathode strips	1 mm
accuracy for perpendicular tracks	100 μm
total thickness of gas mixture in two HADC/LMDC layers	$4 \times 10^{-5} X_0$
total thickness of 4 wire planes (stainless steel)	$4.5 \times 10^{-3} X_0$
total thickness of 4 wire planes	$10^{-3} X_0$
total thickness of 4 plastic foils	$10^{-4} X_0$

be overcome by using properly chosen materials [52]; Upilex¹ can be used for the cathode plane for our purposes.

The other limitation of DME is the flammability limit in air, which is 3.4%. We have tackled this problem by adding carbon dioxide to this mixture. We have computed the transport parameters namely drift velocity and diffusion coefficient of a mixture of He-CO₂-DME (70%-25%-5%) and compared with those of He-DME (70%-30%) and He-CO₂ (70%-30%) [53]. Fig. 23 illustrates this comparison.

The drift velocity of this mixture is not saturated at the fields of operation of the chambers. The Lorentz angle of DME is small, about $2^\circ \div 3^\circ$ at 1.5 T for fields of $1 \div 2$ kV/cm, compared to $8^\circ \div 10^\circ$ of He-DME (70%-30%), and to 32° of Ar-Methane (90%-10%) at similar fields [53].

It is apparent that the proposed mixture retains both the desirable properties of DME and non-flammability of CO₂. This will be experimentally investigated with the first prototype.

¹Ultra high heat resistant polyimide film; Ube Industries Ltd.; Tokyo, Japan.

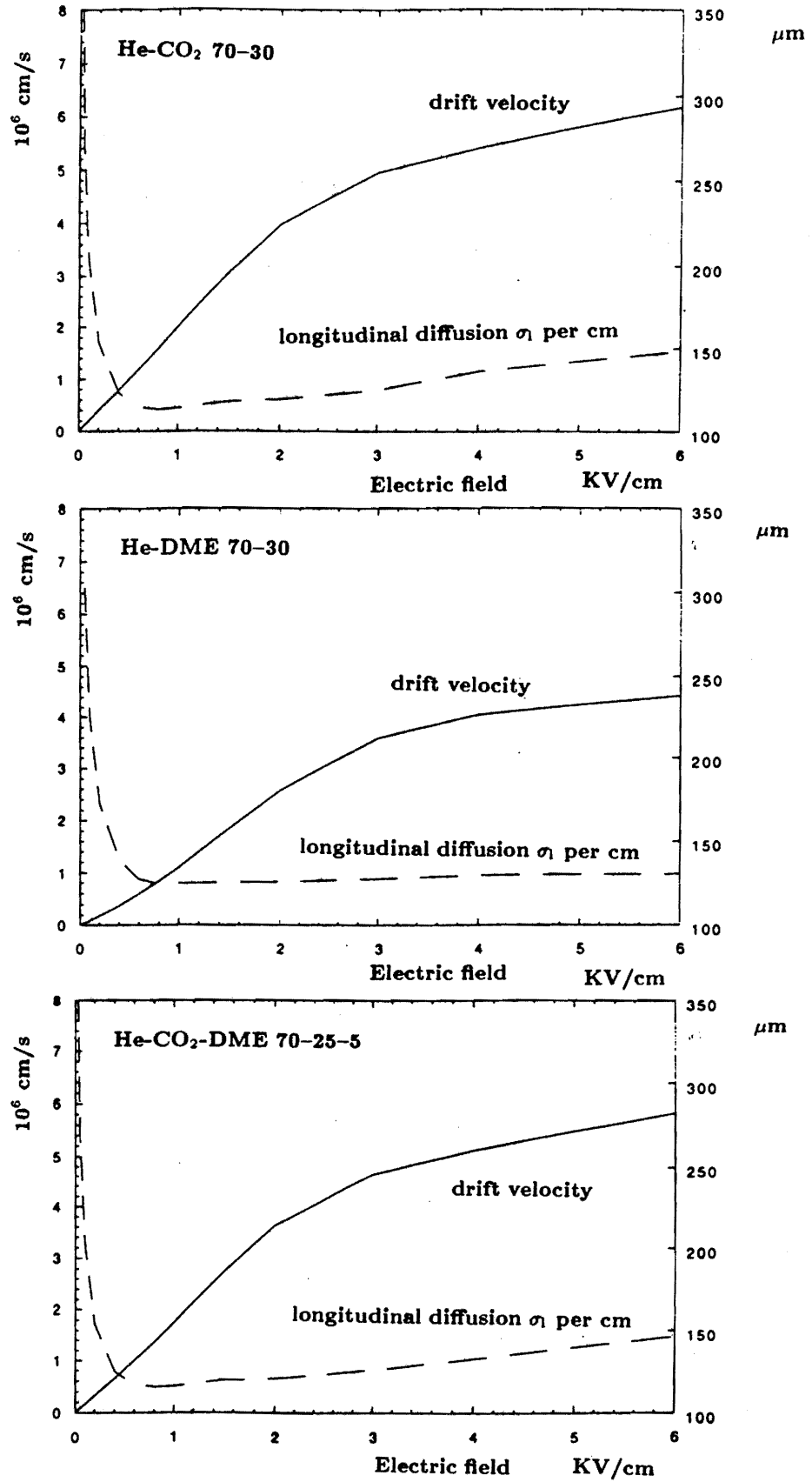


Figure 23: Comparison of the drift velocities and longitudinal diffusion coefficient σ_l for mixture of He-CO₂(70%-30%), He-DME(70%-30%) and He-CO₂-DME(70%-25%-5%).

Table 4: Specifications and materials tentatively used for ST.

material of the sense wire	stainless steel
sense wire diameter	30 μm
diameter of the straws	15 mm
material of the straws	100 μm of aluminized Upilex

4.6 The outer straw tube (ST) array

The basic cell design is a tube or straw of metallized plastic as cathode, with diameter of about 1.5 cm, with an anode wire stretched along its length. Arrays of straw tubes have been constructed and operated reliably as tracking devices with different materials and gases, yielding spatial resolutions of $< 50 \mu m$ in several experiments [54], [55], [56]. Zhou et al. [54] have reported a spatial resolution of 35 μm , 45 μm has been obtained in [55], and 49 μm in [56]. Hence it is resonable to assume an accuracy of 50 μm .

The advantages of having such a system are good modularity and complete electrical and mechanical independence. Problems of photon feedback and neighboring channel cross talk are drastically reduced. Furthermore construction is easy and costs are low. These considerations have been thoroughly studied and examined in [57].

The tubes will be arranged in three superlayers A, B and C (moving out from the interaction vertex). Each superlayer will contain two layers of straw tubes staggered by a distance corresponding to the tube radius in order to have full efficiency with respect to the incidence angle of the tracks. The anode wires of the superlayer A will be parallel to the z axis, while the two other will be tilted by angles of $\pm 15^\circ$ respectively to unambiguously define the coordinates of a hitting track. We are investigating the best mechanical arrangement which will optimize angular acceptance, efficiency and mechanical construction.

Tab. 4 gives some specifications and the materials tentatively to be used in this tracker. The best gas to be employed seems to be pure DME [54] since we do not have constraints of mass at the last layer.

4.7 The outer scintillator array (TOFONE)

The main functions of this detector are the detection of charged particles having a radius of curvature (p/B) larger than a fixed value for first level trigger purposes and the detection of fast ($\sim 400 \text{ MeV}/c$) neutrons from non-mesonic decay. Indeed at a field value

Table 5: TOFONE features.

	<i>TOFONE features</i>
internal radius	109 <i>cm</i>
number of slabs	80
slab width	8 <i>cm</i>
slab thickness	10 <i>cm</i>
slab length	200 <i>cm</i>

of 1.3 T particles with momenta lower than 230 MeV/c will spiralize inside the apparatus and will not hit TOFONE. Then, out of the spectrum show in Fig. 10 only the high momentum portion, which contains the peaks due to hypernucleus formation, is detected. The background generated by the low momentum portion of the spectrum is cut by the trigger request.

The TOFONE will be a cylindrical array of scintillator slabs aligned along z . The dimensions foreseen are given in Table 5.

We will probably use NE110 or NE102A scintillator. Each slab is viewed at both ends by two PMs through suitably shaped light guides whose geometry is chosen as to optimize light collection.

The TOFONE will cover $\sim 60\%$ of the solid angle. If no particular problem will arise from the mechanical point of view, we plan to cover also the inner part of the solenoid end caps by scintillators having a similar segmentation, in order to increase the solid angle for detecting the neutrons up to $\sim 90\%$. A final decision will be taken following the executive mechanical plan.

We expect, on the basis of previous experience and looking at the performances of similar systems, a total time of flight resolution of less than 1 ns FWHM, while with a suitable treatment of the signals from the two PMs looking at the same scintillator slab, the z coordinate of the detected particle can be determined within 5 cm FWHM. The resolutions on the other coordinates are given by the slab dimensions.

The large thickness of the TOFONE is explained by the necessity of detecting neutrons from non-mesonic decays. It is well known that, when the neutron energy increases, the detection efficiency decreases and consequently there would be a strong motivation to make the scintillator thicker. On the other part with an increased thickness it is more difficult to achieve a uniform light collection and the resolution worsens. We foresee to achieve a neutron detection efficiency of $\sim 13\div 15\%$, based on previous experience on

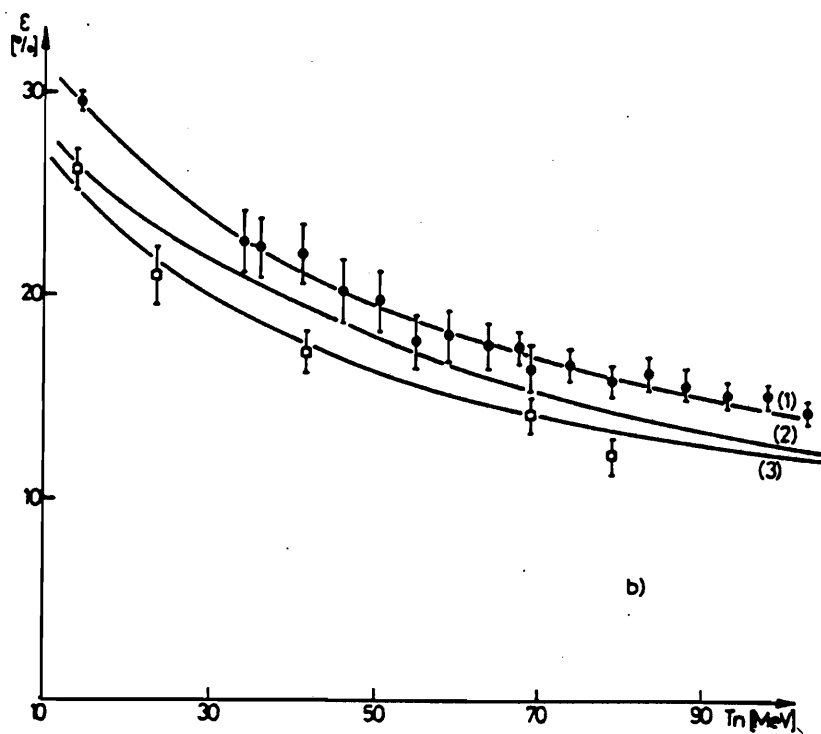


Figure 24: An example of the behaviour of the detection efficiency for a neutron scintillator's bar (from Ref. [58]).

similar systems [58]. Fig. 24 shows the variation of the measured neutron detection efficiency ϵ_n as a function of the neutron energy for a bar of NE 110, $10 \times 10 \times 100 \text{ cm}^3$, i.e. quite similar (a part the length, that in our case is twice) to that we envisage to use, for an equivalent proton energy threshold setting of 2.5 MeV. For neutron energies around 88 MeV ϵ_n is $\sim 13\%$. The resolution on the energy of the neutron, determined both by the scintillator's thickness and the intrinsic time resolution, is rather coarse: 25% for the 88 MeV neutrons from non-mesonic decay. However, it may still indicate, together with the angular correlation, if there will be strong variations from the simple two-body non-mesonic decay mode, as for instance, advocated by other approaches to the phenomenon.

4.8 The Superconducting Magnet

The extensive simulation work carried on up to now, demonstrated that a solenoid, with 2 m diameter and 2 m length and B_{MAX} up to 1.5 T, with a uniformity of the order or better than 1% in the tracking volume, satisfies our physics requirements. Further

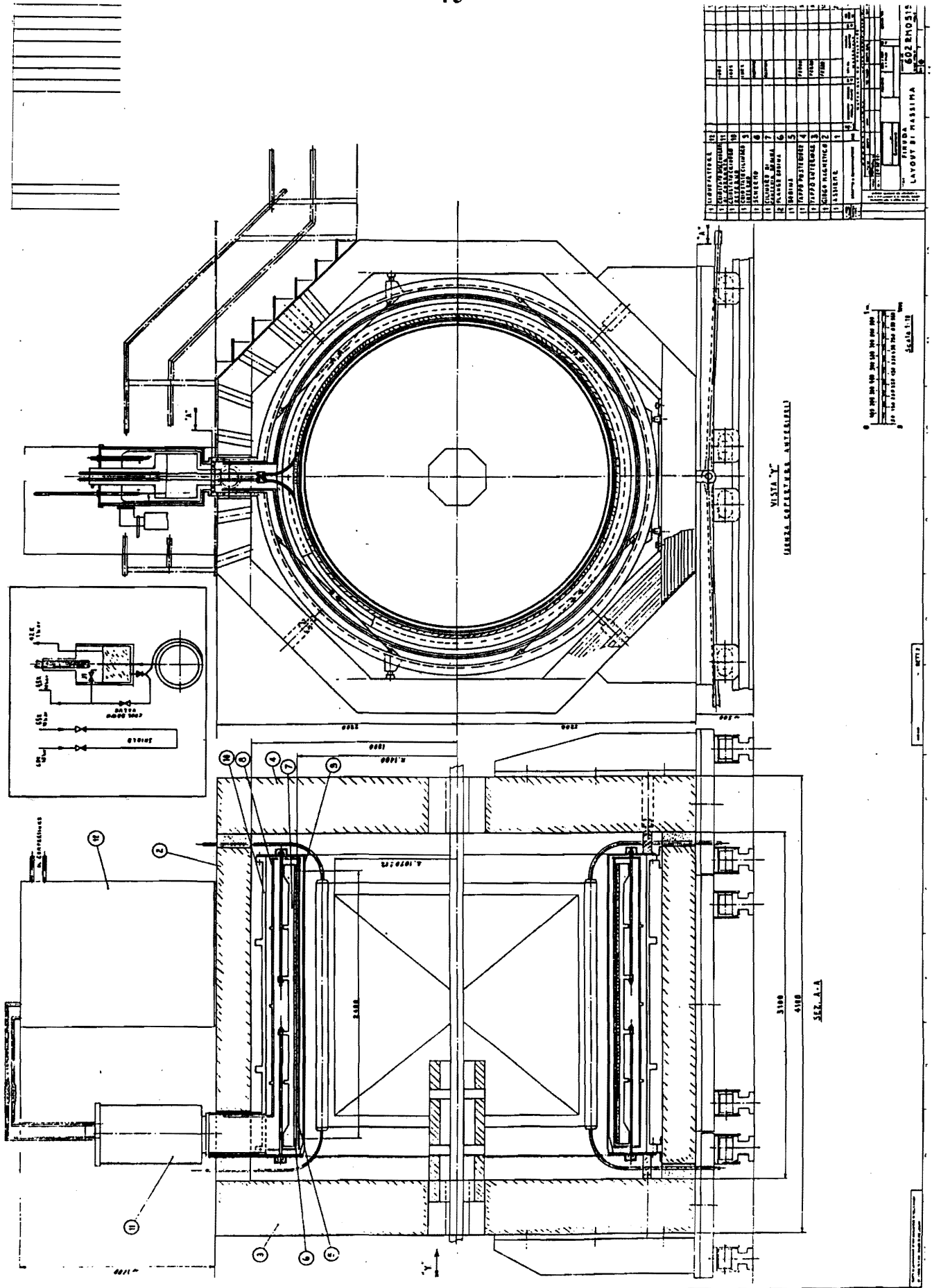


Figure 25: Drawing of the superconducting solenoid. Only one of the low beta Q-poles is drawn for simplicity.

requirements are stray field outside of the magnetic yoke less than few hundreds of Gauss, alignment between the magnetic and the beam axis better than ± 1 mm: at least one of the iron end-cups removable in two sections for access to the detector pieces.

To achieve a B_{MAX} of ~ 1.5 T in the described volume, with a conventional warm magnet, it is necessary to have an electrical power of ~ 3 MW, quantity clearly unmanageable, due the present cost of electricity. For this reason, a superconducting solenoid has been considered and a possible solution will be discussed.

A drawing of the superconducting solenoid is shown in Fig. 25. The coils are made of two layers of superconducting cable, type Rutherford LuCu/NbTi, stabilized with pure (99.996%) Al, and fed with a current of 4100 A. To improve the field homogeneity, the current density in the coils is greater at the borders (55.5 MA/m^2) than at the center (41.5 MA/m^2): this can be obtained using at the border a cable with smaller cross section. To this purpose the coils have been divided in a central zone, 1400 mm long, and two lateral zones, 500 mm long each, in which the current density is 1.34 times greater.

In this way a field uniformity near to 1% has been obtained in the tracking volume: changing the respective length of the central and lateral zones, it would be possible to improve further this value. The coils, insulated with a glass ribbon, will be soaked (under vacuum) with a two component epoxy resin polymerized under pressure. This ensures a good insulation, excellent electrical characteristics and excellent mechanical performances at low temperature.

A 20 mm thick, Al alloy, cylinder will be mounted immediately outside the coil, having a twofold function: mechanical support against the outward directed electromagnetic pressure and support for the tubes used to cool the coils, properly configured to assure a circulation for natural convection during the 4.2 K operation.

The yoke which closes the field lines will have an octagonal cross section, with two end-caps: one, or both, of these will be divided into two sections and movable on rails. The height will be 4200 mm and the length 4100 mm. The walls will be made of superimposed iron layers type ARMCO, each $60 \div 80$ mm thick, for a total thickness of 400 mm, while the end-caps will be 500 mm thick. These dimensions of the return yoke ensure a stray field outside the solenoid of less than a few hundreds of Gauss.

Both the coils and the shields will be cooled using a helium liquefier automatically driven. The global system will work under VME multi-tasking, able to monitor all the more significant parameters, to drive in a complete automatic way all the operations, to allow control from the experiment (i.e. to fix the value of the magnetic field).

The magnetic field stability will be continuously monitored by NMR. More details

Table 6: Main characteristics of the solenoid.

$B_{0,MAX}$	1.5 T
NI	3.6 Masp
Nominal current	4100 A
Stored energy	14 MJ
Autoinductance	1.62 H
B_{MAX} on the conductor	1.8 T
R_{prot}	0.244 Ω
$\tau_{discharge}$	6.6 s
Temperature margin	3 K
Height	4200 mm
Length	4100 mm
Weights:	Ferromagnetic yoke: 260 Ton Magnet and cryostat : 8 Ton Cold Box liquefier : 1.5 Ton
Electrical consumption :	He liquefier : 92 KW Power supply : 10 KW
Hydraulic consumption :	He liquefier : 4 m ³ /h of water at 3 bar Power supply : 1 m ³ /h of water
Estimated thermal losses :	\sim 8 W at 4.2 K \sim 100 W at 60 K

on the solenoid can be found in the Appendix 4.

Table 6 summarizes the main characteristics of the described magnet.

4.9 First level trigger

At the top luminosity $\mathcal{L} = 10^{33} \text{ cm}^{-2}\text{s}^{-1}$, the expected total rate for ϕ production is about 4.4 KHz, but we cannot use the RF signals for fast triggers due to the short interbunch time (2.6 ns). The production rate of ϕ is about 5.7×10^{-5} per bunch.

The goal of the trigger is to select (K^+K^-) from Bhabha scattering events, other ϕ decays and cosmic rays.

In the angular region covered by TOFINO (see Fig. 13) the Bhabha scattering cross section is some orders of magnitude lower than in the forward and backward directions. Rates of (K^+ , K^-) and (e^+ , e^-) will then be of the same order of magnitude (few KHz). Rates due to other ϕ decays are considerably smaller.

For these reasons the simple request of multiplicity two in TOFINO is not enough;

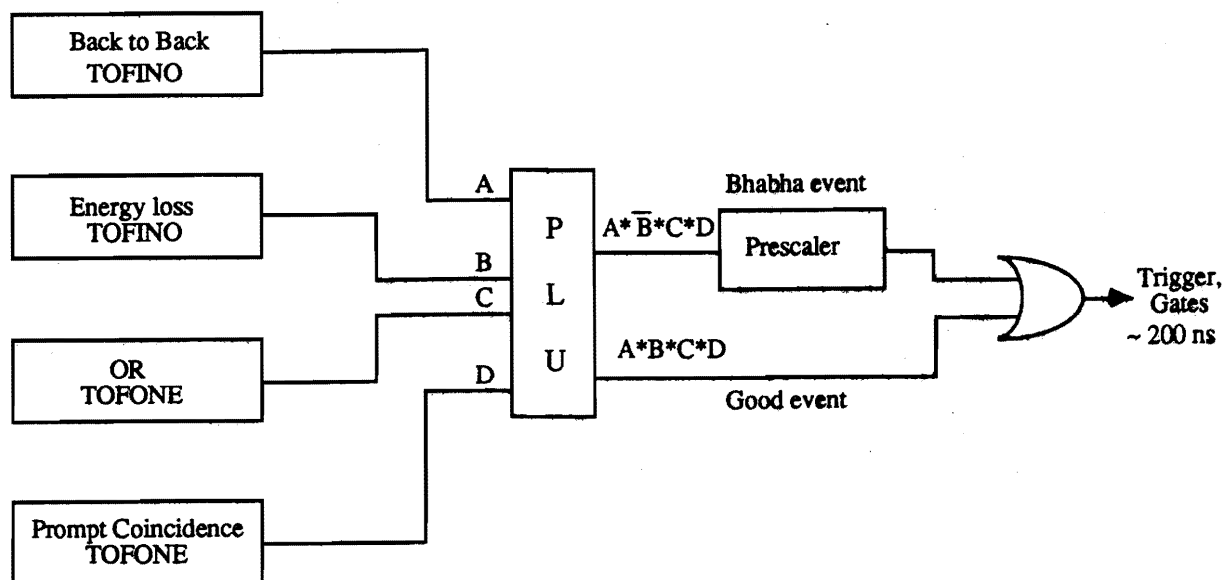


Figure 26: A simplified scheme of the first level trigger.

we can use the information of the energy loss in 1.5 mm of scintillator (see Fig 18), in order to discriminate kaons from pions, electrons and cosmic rays, with high threshold discriminators.

TOFINO can also be used to identify “back-to-back” topologies in the interaction region by simply requiring a coincidence between “axially symmetric” slabs. As described in Sect. 4.2 each scintillator will be viewed by one PM and consequently the arrival times of the signals coming from the PM depend on the crossing point of the particle. This can be accounted for by means of a Mean-Timer (MT) like operation between the two signals coming from axially symmetric scintillators. The resulting timing signal will not depend on the emission angle for any given interaction point.

The OR of the six MT signals can be used not only to trigger, but also for providing the best START signal for Time-Of-Flight system (TOF) and drift chambers.

The time spread of this START signal will be about 650 ps due to the extension of the interaction region (7 cm FWHM \rightarrow 550 ps) in the z coordinate and to the electronic jitter (150 ps). Then the time of flight can be corrected in the off-line analysis by determining the (e^+, e^-) interaction point by means of information from ISIM.

We can use in the trigger TOFONE for two purposes: multiplicity and prompt

coincidence. Each TOFONE slab, at trigger level, is identified by the MT performed on the signals coming from both sides of the slab.

The hypernuclear events are signalled by requiring at least one fired slab of TOFONE within a narrow timing gate (due to π^- coming from stopped K^- interaction).

In summary the first level trigger (Fig. 26) is based on TOFINO and TOFONE and it performs:

- on TOFINO
 - energy loss selection by high threshold discriminators;
 - "back-to-back" topology (multiplicity ≥ 2);
- on TOFONE
 - multiplicity ≥ 1 ;
 - prompt coincidence.

These possibilities can be combined using a Programmable Logic Unit in order to trigger either on good events or on prescaled Bhabha events that can be useful for calibration purposes.

The trigger works in $\sim 150 \div 200 \text{ ns} \ll 1/(rate_\phi + rate_{Bhabha}) = 1/(10 \text{ KHz}) = 100\mu\text{s}$. At that time we can give gates and strobes to readout electronics to digitize the information (requested time $\sim 10 \mu\text{s}$). During the digitization we could perform a second level trigger, using ISIM and TOF information. If we use a Programmable Logic Device, that second level decision takes a few μs .

If a negative decision is taken we can stop the conversion process with a fast clear ($2 \mu\text{s}$ dead time). Otherwise, before reading out and writing on tape the full event, it's possible to process via software in a few ms some basic information, like ADCs of TOFINO, after reading them out via VME bus. The ADCs can give a better information on the energy loss on the slabs. Finally, if every step is successful we can read the full event out and write it on tape.

4.10 Data acquisition (DAQ) architecture

From the DAQ point of view, the experimental setup consists of several sub-detectors, each of them running almost independently.



The apparatus can logically be divided in the following parts (from the center to the external side):

1. the ISIM and OSIM arrays
 \approx 16000 channels;
2. The LMDCs and ST array
 \approx 10000 channels;
3. the TOFINO and TOFONE arrays
 \approx 600 channels.

The trigger can be considered as a particular sub-detector, since the associated electronics concerns essentially the setup procedure. It does not contribute significantly to the event size.

The FINUDA on-line architecture is devised to enable a centralized DAQ as well as independent data taking for each sub-detector.

The modularity and complexity of the apparatus are taken into account in the DAQ system by a distributed architecture, with a high level of parallelism, adopted in order to cope with the big amount of raw data.

The system requires amplitude and/or time measurements in the channels. It also requires fast logic signals from the scintillators.

The general DAQ scheme is shown in Fig. 27 and Fig. 28. In order to allow fast data acquisition and reductions, microprocessors will be used on the various sub-detectors.

All the signals coming from the front-end electronics (FEE) of each sub-detector will be read in a parallel mode by one or more VME CPUs in order to reduce the overall dead time. Trigger interrupts are seen directly by the microprocessors.

For each subdetector, one (or more) dedicated VME CPUs, called Local Event Builder (LEB), assemble(s) all the information in a sub-event and perform(s) the local monitoring.

The LEB tasks are essentially:

- a) sub-event acquisition for each sub-detector;
- b) monitoring and calibration of the sub-detector, setup and reset of the associated electronics;
- c) status display of the sub-detector components;

- d) test and control of the sub-detector.

The LEB computer configuration of each VME crate will be:

- a) one MOTOROLA 68040 type CPU for acquisition purposes;
- b) One MOTOROLA 68040 type CPU for monitoring purposes;
- c) mass storage disks that can be located directly on the VME crate or linked via ETHERNET (NFS, Network File System) to the master CPU;
- d) ETHERNET link.

At this level the data from each sub-detector, to be assembled in the full event are sent to one or more dedicated CPUs called the Global Event Builder (GEB),

The global event is then written on an appropriate mass storage directly from the GEB through a dedicated bus.

The GEB tasks are essentially:

- a) building of the global event;
- b) transfer of the on-line data to the mass storage;
- c) test and calibration of the apparatus;
- d) partial and optional DAQ monitoring, sampling and fast analysis of complete events;
- e) optional total detector reconstruction on sample basis, status display of the global event.

The GEB computer configuration, one VME crate, will be:

- a) one memory board related to each sub-detector;
 - b) one MOTOROLA 68040 type CPU devoted to build up the global event;
 - c) one MOTOROLA 68040 type CPU devoted to data recording;
 - d) one or more MOTOROLA 68040 type CPUs for monitoring tasks;
 - e) mass storage disks, that can be located directly on the VME crate or linked via ETHERNET (NFS) to the master CPU;
 - f) ETHERNET link.
-

The global control of the experiment will be performed by several workstations connected to the microprocessors via ETHERNET and dedicated buses. One workstation dedicated to each sub-detector and one more for the global control are foreseen. All these workstations will be interchangeable and each subdetector will be able to work independently.

The data written on mass storage will be sampled for on-line monitoring in the VME crates. A partial monitoring could be done directly on the VME microprocessors and the results of the analysis will be sent to the associated workstation where it will be displayed. The overall DAQ monitoring and the total detector reconstruction on sample basis will be performed and displayed on the workstations.

This structure will allow to use the off-line reconstruction software also at the on-line stage and guarantee an easier maintenance of the programs.

The workstation tasks are essentially:

- a) interaction with operators for the global control of the experiment, statistics and acquisition tests;
- b) overall data acquisition monitoring and total event reconstruction;
- c) display of the monitor results;
- d) event display;
- e) storage of all the parameters related to the various configurations of the experiment.

The main characteristics of the data flow are:

- a) **ISIM and OSIM**
Zero suppression performed by front-end electronics or readout CPUs
Sub-event buffer length: ≈ 400 words (800 bytes);
- b) **LMDCs and ST**
Zero suppression performed by front-end electronics or readout CPUs
Sub-event buffer length: ≈ 150 words (300 bytes);
- c) **TOFINO, TOFONE and trigger**
Zero suppression performed by front-end electronics
Sub-event buffer length: ≈ 100 words (200 bytes).

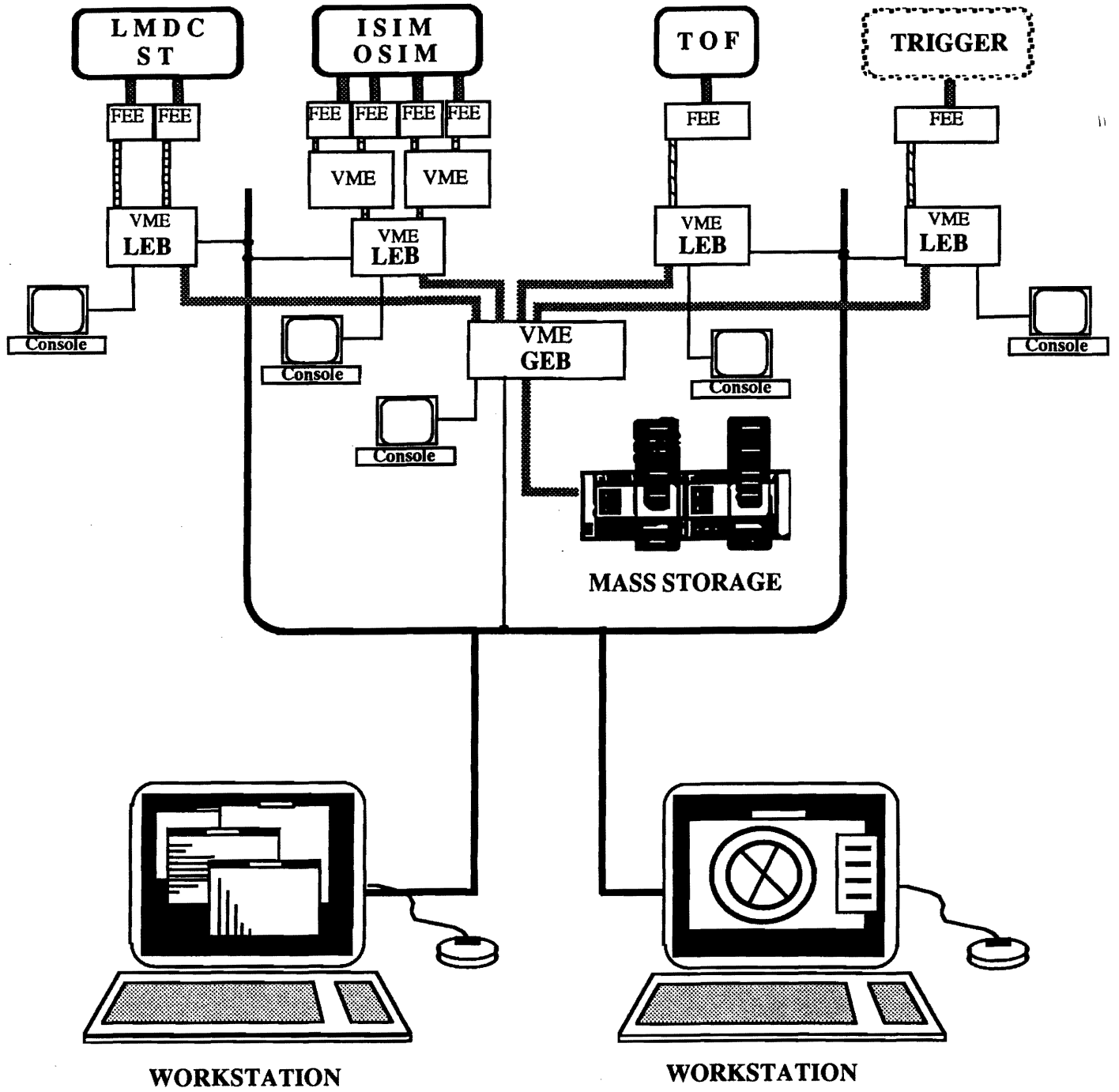


Figure 27: General data acquisition scheme.

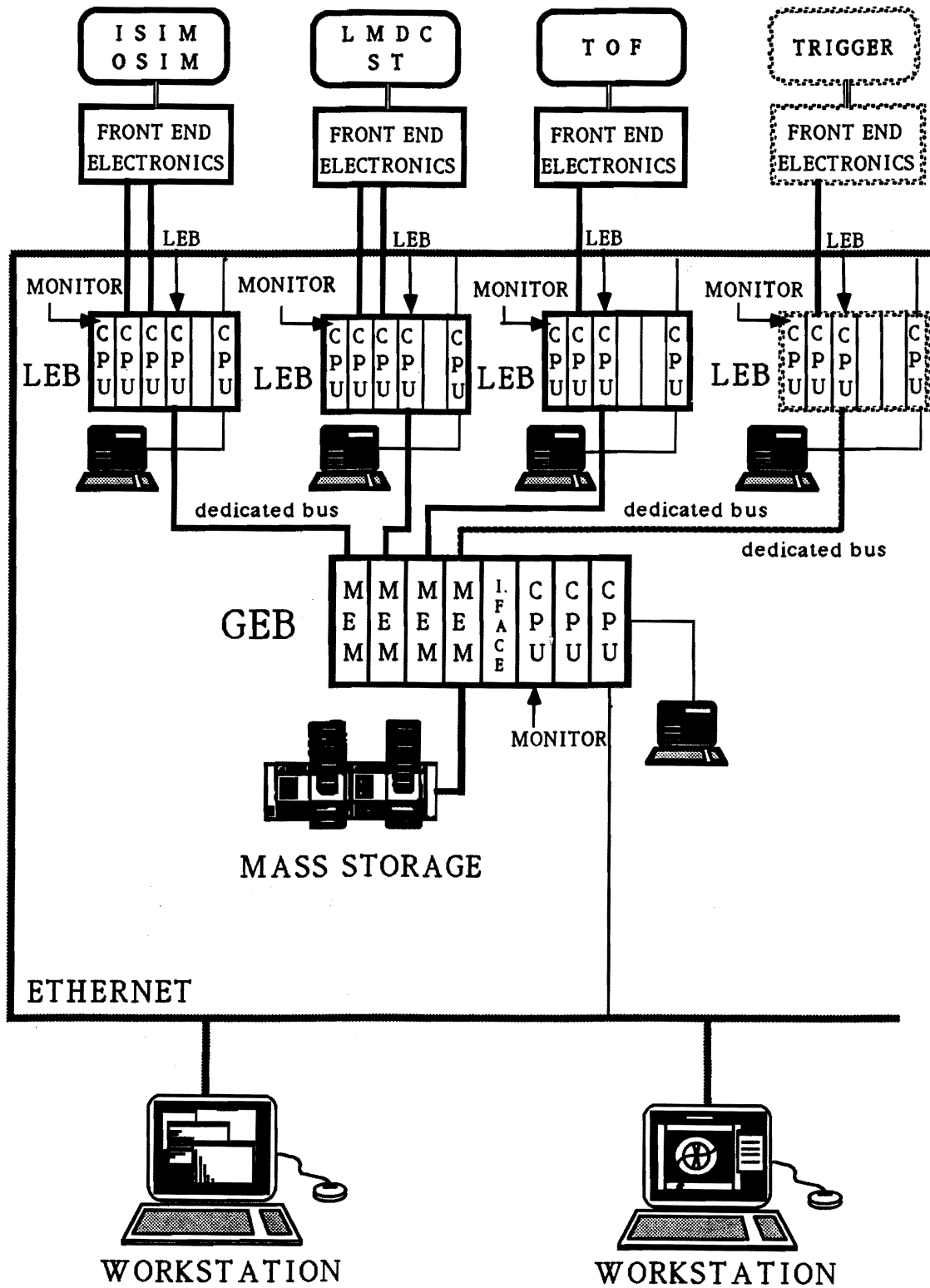


Figure 28: Data acquisition architecture.

The global buffer length should then be of the order of 1.5 Kbytes.

An estimate of the global event acquisition rate can be obtained taking into account the different steps in the data acquisition: trigger, conversions, interrupts, readout and zero suppression, event building and data storage.

Taking into account the high degree of parallelism of the acquisition, the standard hardware now available ensures at least an acquisition rate of ≈ 100 events/s.

This limit is mainly due to the readout and zero suppression of ISIM and OSIM and to transfer rate of the standard storage media. This rate could be enhanced by a suitable event packing.

Another limitation is the storage capacity (at present ≈ 200 Mbytes). Nevertheless the evolution of the technology should make available cartridges with much better performances. In these conditions the data recording will no more represent a limit in the acquisition rate.

4.11 Gas distribution and control system

The gas distribution and control system has been designed for the use of different gases and/or mixtures in the drift chambers, straw tubes and in the Helium tank.

The layout of the system consists of the following main sections:

- a) distribution section;
- b) control and blending section;
- c) detectors section;
- d) analysis and on line monitoring section.

Each of them has specific functions and interacts with the other sections as described in the following.

a) Distribution section

In the flow lines of the gases, between the distribution rack and the control and blending system, there is a set of valves which accomplish different purposes :

- cut-off valves: they are preset by Safety Service to automatically stop the gas flows in presence of anomalous concentrations, revealed by gas leakage probes.
 - check valves: they avoid fortuitous gas blending in the distribution piping due to erroneous pressure unbalance;
-

- safety valves: they are preset to safety limits according to our working conditions. On overpressure they release the excess gas towards the exhaust;
- purge valves: they allow purging vent lines and the whole system with an inert gas (Ar).

The piping from distribution rack to experimental racks will be made of stainless steel and polyurethane. To prevent the contamination of He (used as tank gas) with the other gases we plan two distinct vent lines.

b) Control and blending system

Concerning the control and blending system, the main components are the thermal mass flowmeters (Brooks model 5850) which measure and control each flow of gas according to the preselected values. These values may be set separately for each gas on the control and readout equipment, either independently or in servo-mode.

In the latter mode the requested flowrate of the main component of the blend (master gas) is set on the controller dial while the flowrate of the other component (slave gas) is set as a percentage of the master flow.

In this way, by regulating this last one, the flow rate of the slave gas will be driven consequently, with no change in the preselected composition of the blend.

On failures or electric power breakdowns a bypass emergency line may be activated in order to preserve the gas flow through the detectors. The elements of this line are, in sequence, a manually operated valve, a manometer and a flowmeter with its needle valve. The flowmeters must be adjusted to the same value set on the Brooks valves.

The reset of the power supply does not imply the automatic reset of Brooks valves, since a manual restore may be planned after blackout: in this way one avoids pressure shocks due to the sudden opening of the valves, especially dangerous for the very thin windows of the chambers.

c) Detectors

Two control operations are required :

- monitoring of all absolute pressures
- monitoring of all differential pressures

The differential pressure regulation is achieved both by adjustments of gas flowrates entering the chambers and proper modification of the oil level in the bubbling device, which are located between the chamber outlets and the vent lines. Other bubbling devices

are inserted before the chambers inlets as additional safety device against pressure raising over preset values.

d) Analysis and on-line monitoring

It consists of the lines and devices necessary to monitor that the mixture percentages of flowing gases remain constant.

It is possible to test each line of the distribution system and the outlets of each chamber in order to locate easily sources of incidental contaminations or leakages. The test will be performed by a mass spectrometer.

Besides local readout, the system is linked with the DAQ in order to allow remote on-line monitoring of the whole set of parameters.

In Fig. 29 an overall scheme of the gas distribution and control system is given.

4.12 Mechanical installation

The area in which the apparatus has to be installed (Fig. 30) is a rectangular hole $10.00 \times 11.00 \text{ m}^2$. The depth of the hole is 2.50 m and the beam line elevation from the floor is 1.20 m.

The magnet can be moved laterally sliding on rails after having disconnected the sections of the beam pipe which are contained inside the apparatus. It is likely that the low-beta quadrupoles connected with the beam line close to the target region will be enclosed in the magnet. However, they will not limit the acceptance of the detector, since they are outside the useful tracking volume.

We foresee that at least one of the two end-cups could be divided into two parts and they can slide too on rails in order to allow the extraction of the inner removable detectors (see Fig. 31).

The ST array and TOFONE will be solidal to the magnet. The light guides of TOFONE will be brought out from the magnetic volume through holes drilled in the end-caps of the yoke. The PMs will consequently sit out from the yoke (see Fig. 32).

The LMDCs, OSIM, ISIM and TOFINO could be removed as a whole or individually taking also into account that we must have a rather quick way to substitute the nuclear target.

All the tracking detectors must be positioned relative to the magnet with a mechanical accuracy of $100 \mu\text{m}$. The final alignment of the detectors before every data taking run will be obtained by means of laser based optical systems and finally checked with the Bhabha events.

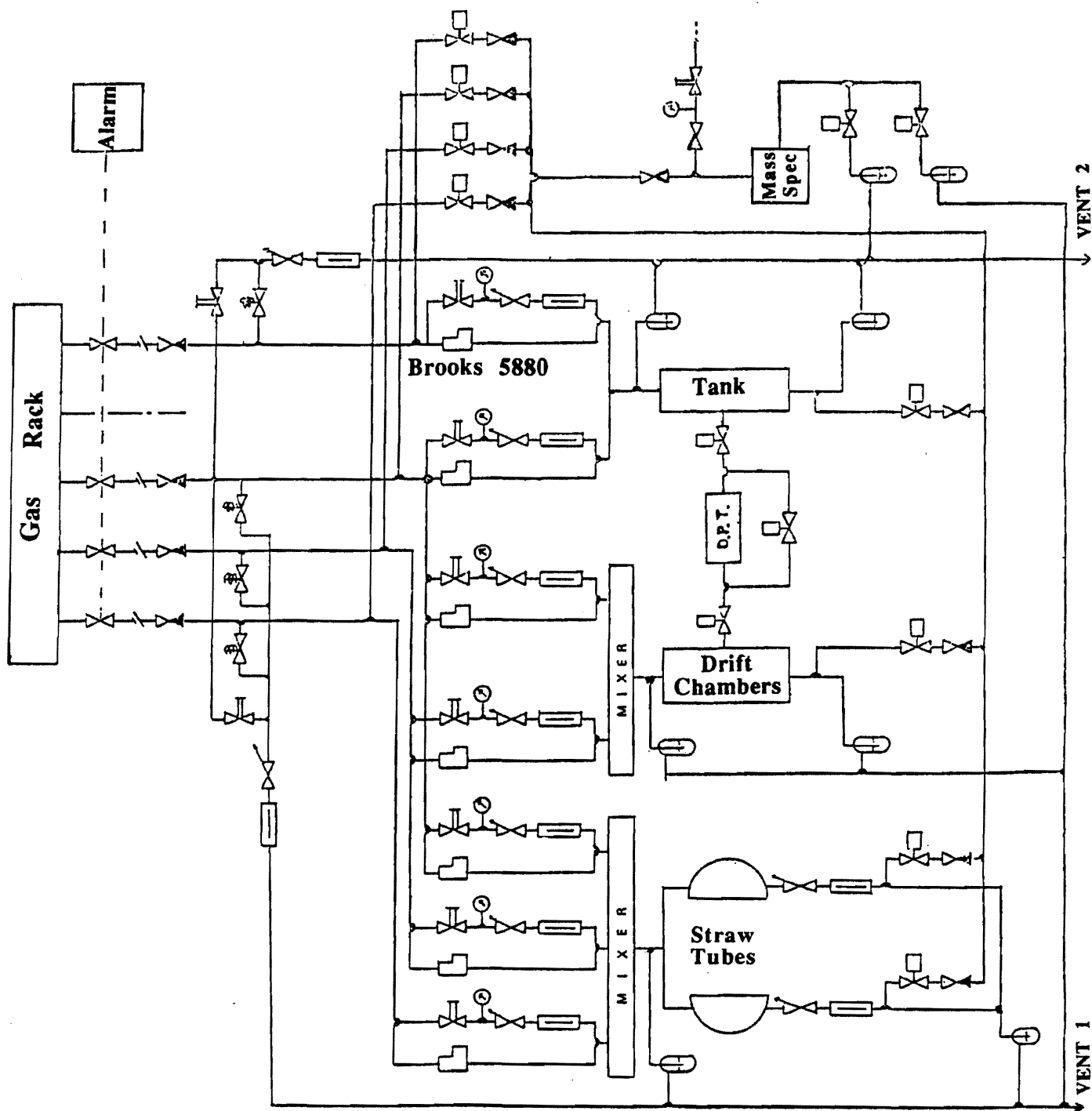


Figure 29: Gas distribution and control scheme.

On the contrary the reproducibility in positioning the whole magnet relative to the beam pipe can be acceptable within 1 mm.

We may envisage a system of monorails allowing the transport of the removable parts of the detector in the counting room/laboratory likely located in the present ADONE control room.

4.13 Calibrations

In order to exploit at best the timing resolution properties of each element of the scintillator array, it is mandatory to have a precise and flexible calibration system allowing to equalize the timing of the different scintillators within 200 ps or better.

To this purpose we will use a calibration system based on a N₂/Dye laser combination (LN203CN₂ + LD2S lasers of the PRA firm: the pulse width is $\sim 300 \div 600$ ps, the spectral band width is $1 \div 3$ nm, the energy stability is $\pm 3\%$ with a repetition rate variable between 10 and 50 Hz), whose pulses are transmitted through optical fibers (HCS-HCN) to each scintillator slab.

In particular all the fibers will see the output of the laser beam and will be directly embedded in the scintillator through a small hole.

Then the laser based system allows a simple calibration procedure: the same laser pulse, suitably splitted following the described optical fibers array, activates all the scintillators of the detector at the same time and a good primary timing of the trigger can be given. A similar system is successfully operating in the OBELIX spectrometer [59]. Routine calibration in conditions similar to experimental measurements can be performed with the Bhabha scattering events.

The coordinates of a particle traversing the drift chamber in the plane perpendicular to the sense wires are determined by drift time measurements and knowledge of the geometrical wire positions, the drift velocity and the Lorentz angle, while the z coordinate along the sense wires is determined using resistive charge division. We plan to use a laser system also for these purposes.

UV lasers, in fact, have proven to be a simple, powerful and versatile tool for calibrating and surveying drift chambers [60], [61], [62] and for precision measurements of electron transport parameters in gases, but the photon energy of these lasers is only $3 \div 4$ eV, not sufficient to ionize usual drift chamber gases which have ionization thresholds from 9 to 16 eV also via two-photon processes.

Then for ionization it is mandatory to use doped substances which have a suitable

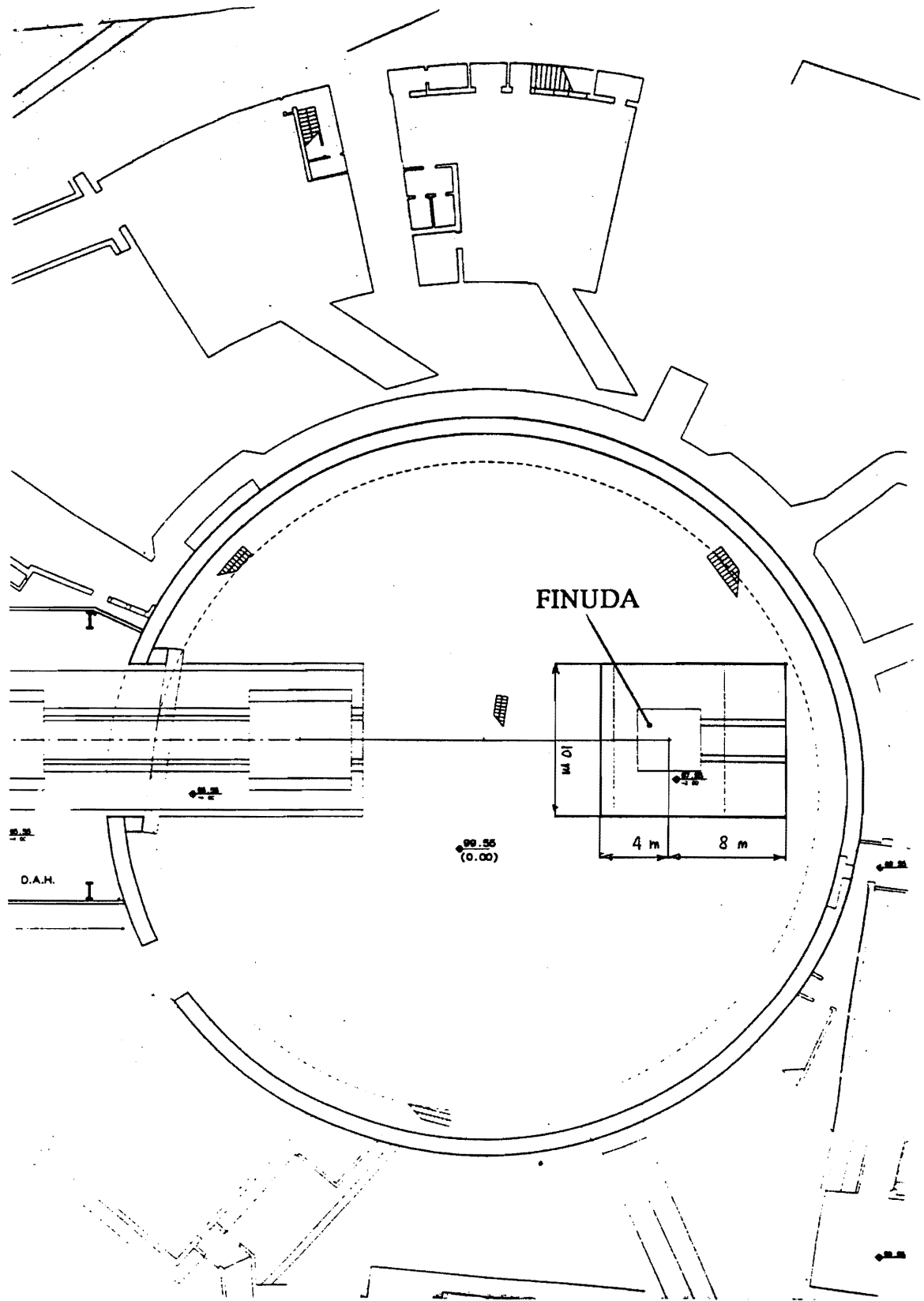


Figure 30: The installation of FINUDA in the DAΦNE building.

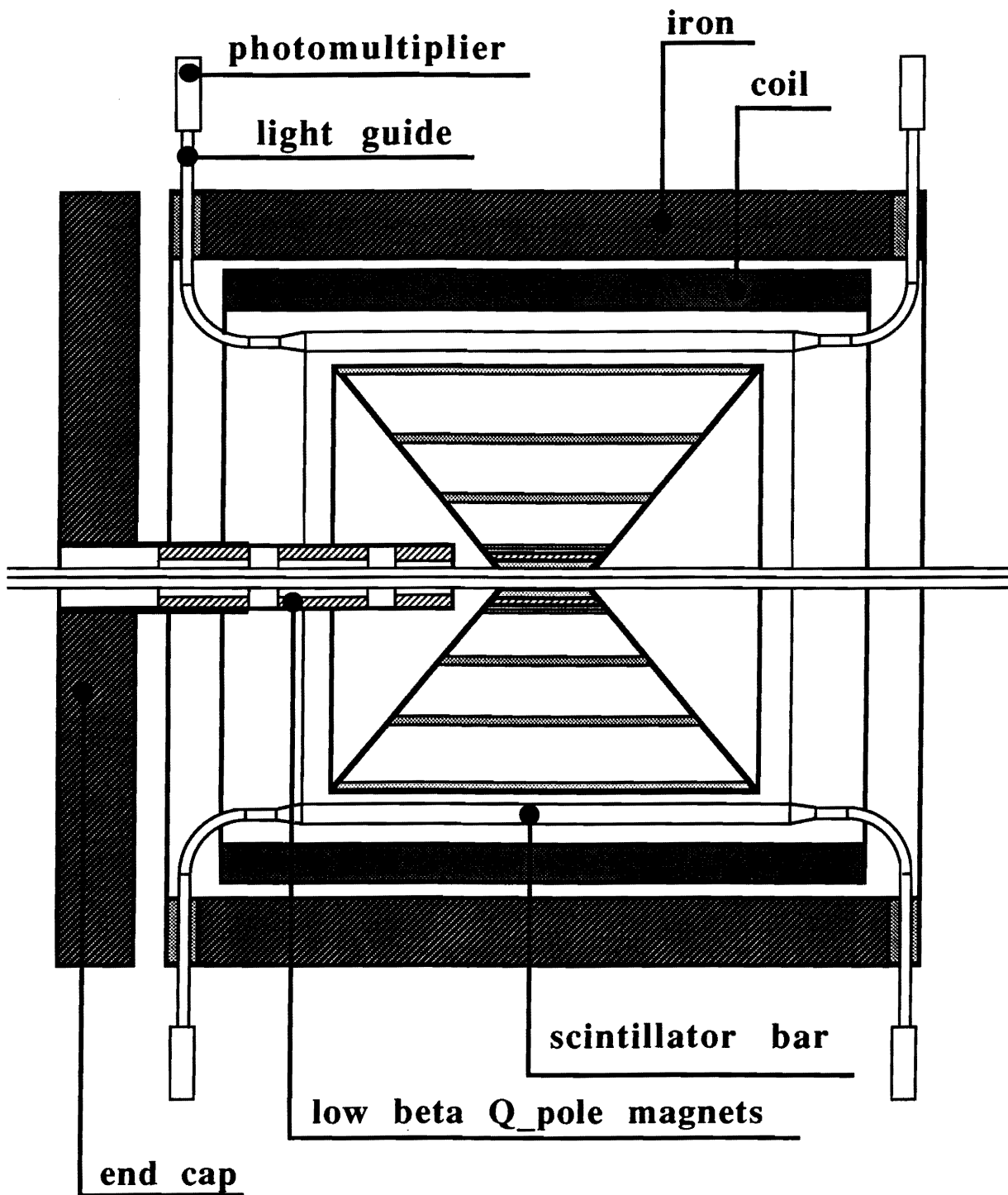


Figure 31: Side view of the solenoid and detector. Only one end-cup and low-beta Q-pole is shown for simplicity.

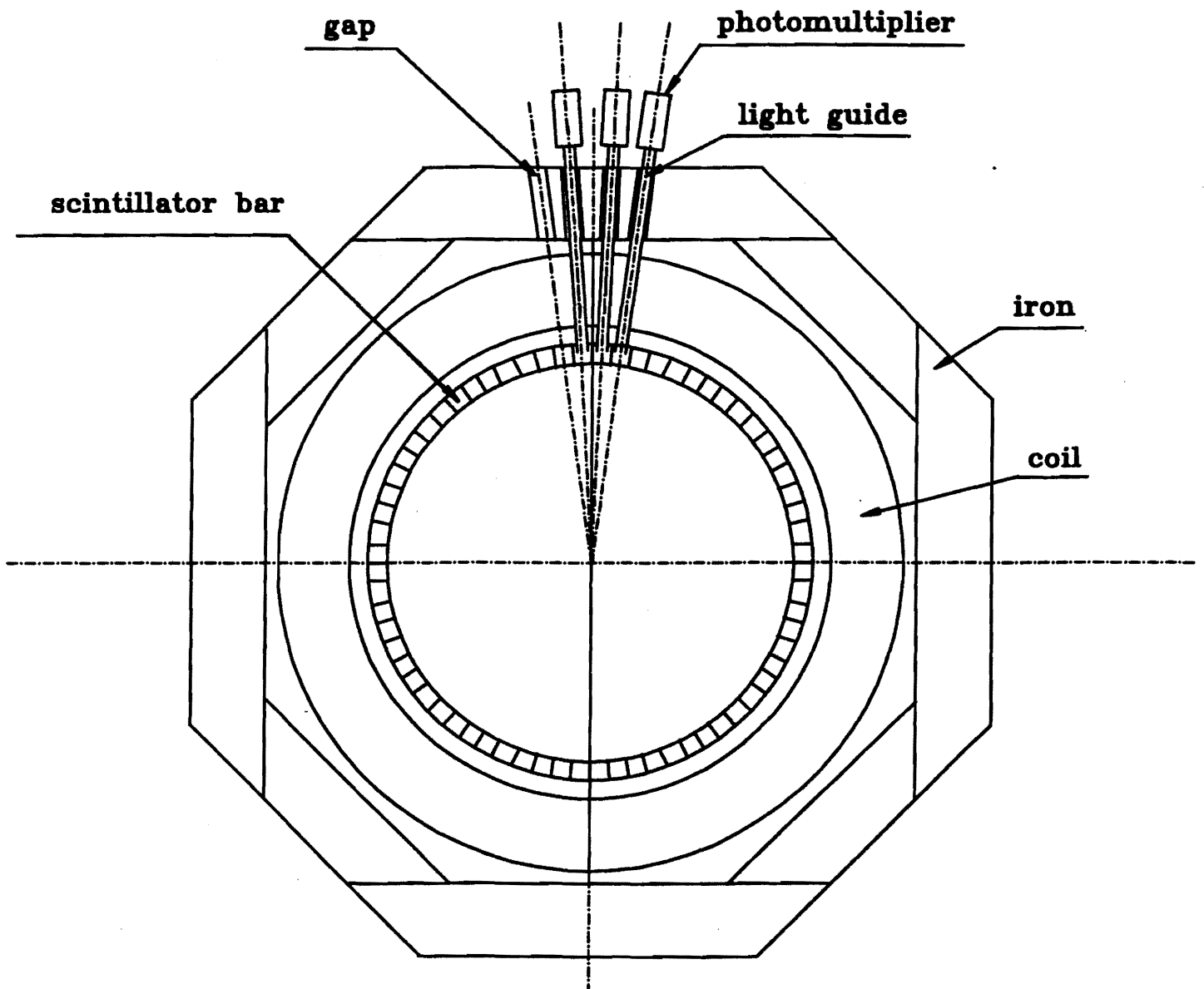


Figure 32: Cross section view of the solenoid with the TOFONE's phototubes.

photon absorption energy or UV lasers with higher energy density. Another laser calibration system is based on Nd-Yag lasers at a wavelength of 266 nm (4.68 eV) with moderate energy density. After the choice of the gases of drift chambers we will test the best system among N₂ or Nd-Yag lasers: it could be important to avoid the use of doped substances that are toxic and chemically active.

Of course the laser beam will be directed onto suitable mirrors and finally reflected into the chambers.

4.14 Off-line software

The aim of the off-line software is to accomplish three main tasks:

- 1) Monte Carlo simulation of the apparatus;
- 2) event reconstruction and analysis program;
- 3) detector calibration.

The computer code is written in Fortran 77 language and maintained using the PATCHY code management system [63].

The purpose of the MC simulation is twofold. On one hand, in the design stage, it has been used to compute, as realistically as possible, geometrical and trigger efficiencies, experimental resolutions and background rejections. On the other hand it will be used, in a second stage, to generate a simulated Raw Data Tape (RDT), formally identical to a real one, in order to make a full test of the reconstruction and analysis procedures and compute reconstruction efficiencies.

The MC simulation of the apparatus has been performed in the framework provided by the CERN GEANT3 software [64]. All the different physical volumes of the detector have been modelled with high level of detail, and some different options have been tested for the internal region (silicon microstrip or microstrip gas chamber) and for the tracking system (low mass chambers or TPC).

Particles produced in the interactions are tracked through the various volumes of the apparatus and energy loss, multiple scattering and decays are taken into account by GEANT physical processes. Hadronic interactions are not accounted for and the hypernucleus formation and decay are properly inserted as user tasks.

The kinematics part of the program is based on the GEANFI code, developed by the KLOE collaboration [65]. The event generator routine handles ϕ decay into ($K^- K^+$),

$(K_S^0 K_L^0)$, $(\pi^- \pi^+ \pi^0)$ and the decay of neutral and charged kaons. Concerning the formation and the decay of the hypernuclei, we have written a dedicated routine. For every K^- stopped in the target, we force the π^- following (16).

In the same routine the different decay modes of the hypernuclei, in particular the non mesonic channels, are implemented. Fig. 33 shows the front display of the event with proton stimulated decay and Fig. 34 with a neutron stimulated decay.

From the geometrical point of view, the apparatus architecture has been logically divided in the three main parts described in Sec. 4.1. A single PATCHY control card allows to substitute the ISIM with a gas microstrip chamber (GMSC) and/or the complex of tracking devices (OSIM + LMDCs + ST) with a TPC. Hits of the tracks in the different detectors are recorded and smeared with the proper resolution functions.

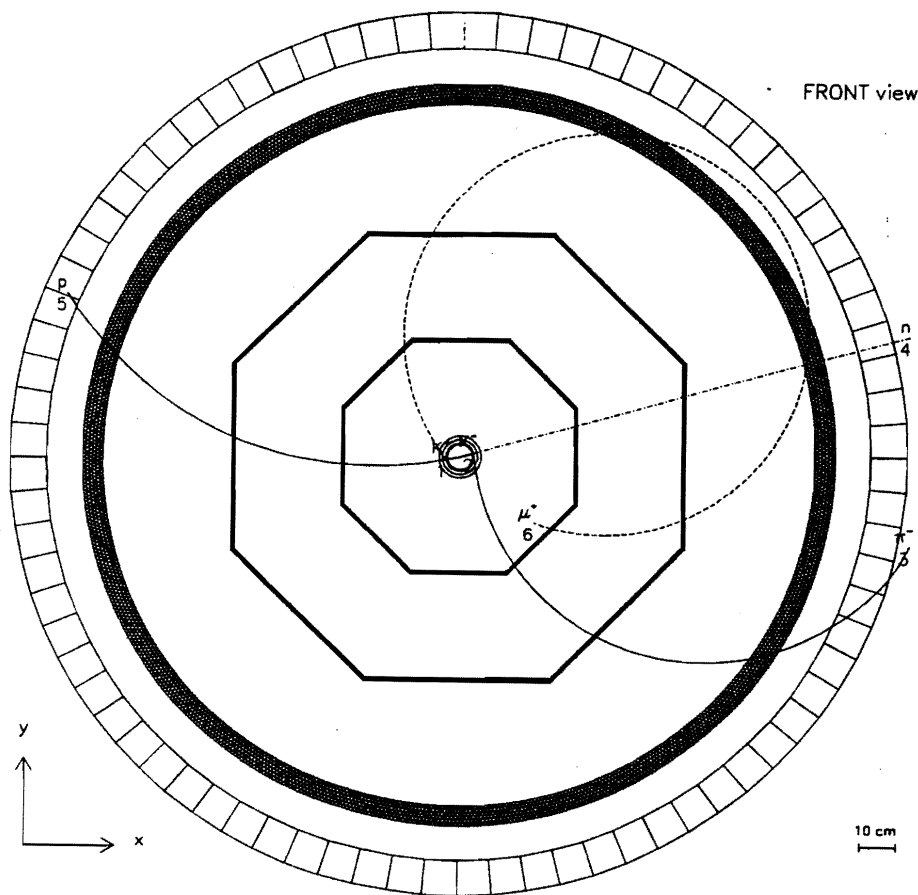


Figure 33: Simulated event with proton stimulated decay.

Track fitting procedures are applied to the points measured by the tracking detectors, momenta of the tracks are computed and momentum resolutions are estimated as

a function of the assumed spatial resolutions (see Fig. 16, 17). First raw procedures for vertex reconstruction and momentum correction for energy lost in the target material have been also applied and tested [see Fig. 15].

Improvements of the MC simulation program are foreseen. In particular:

- geometrical description of the detectors and of the mechanical parts relevant for the particle tracking will be specialized on the final design of the apparatus;
- accurate simulation of the response and of the efficiency of the different detectors has to be inserted in order to reproduce the assumed or measured characteristics;
- a complete RDT, identical in structure to the real one will be produced by the MC program. The information on event kinematics will be added in proper locations/banks to the simulated RDT. The event then could be reconstructed using the same software as for real data.

At present the computer time needed for generate one event and reconstruct vertex and momenta of the track is, on average, less than ~ 1 s on a 4000/90 VAXstation.

The reconstruction and analysis program will be composed of several parts:

- reading of the RDT structure and decoding of the contents;
 - correction of the raw data with the geometric and physical calibration appropriate to the analyzed run;
 - pattern recognition of the event and tracking of the tracks within the apparatus. The low level of the background and the high rejection power of the trigger allows to wait for clean events. A high efficiency of the pattern recognition in spite of the limited number of hits available, is then expected;
 - track fitting, for which standard procedures are already available. The high uniformity of the magnetic field provided by the solenoid and the possibility to perform easily calibrations using Bhabha scattering will allow to obtain good results in a first approximation with simple helix fitting;
 - hypernucleus formation vertex reconstruction and negative pion momentum correction for the energy lost in the target. The back tracking needed for vertex reconstruction with calculation of energy lost and possible transport of the error matrix could be easily accomplished by the use of GEANE package
-

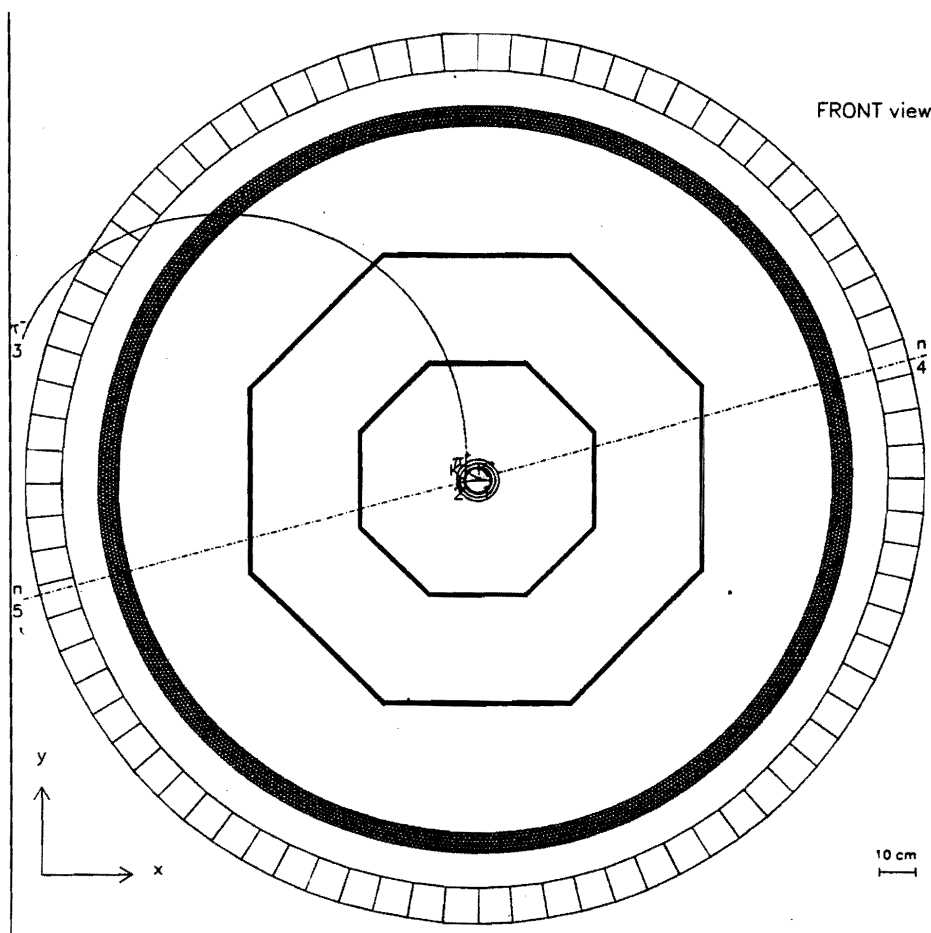


Figure 34: Simulated event with neutron stimulated decay.

[66] which is integrated with the GEANT system. In this way the work already done for the detector simulation can be fully exploited in the reconstruction phase;

- identification of the hypernucleus decay.

All the data resulting from decoding and reconstruction phases will be stored in a ZEBRA structure [67], so to be easily retrieved in the analysis part of the program.

The full reconstruction program or a relevant part of it will be activated on a sample of events during the data taking. This will be helpful as a physical monitor of the data taking itself. An event display procedure will be included in the reconstruction process and will be available both in on-line and in off-line analysis.

Some reduced parts of the reconstruction procedures, or proper parameterization of them could also be utilized during data taking as second level trigger to select with higher efficiency the desired event configurations.

All the calibration constants will be stored in one file, the calibration database. This file could be a directory structured RZFILE based on ZEBRA direct access software. The procedures for update and maintenance of the calibration database could be directly written or an existing database system could be employed. In the reconstruction many sets of constants will be needed. For each run period one type of constants will be kept in one directory. The different sets of constants will be identified univocally by the range of runs for which they are valid.

Coherence among the data under reconstruction/analysis and the calibration constants adopted will be automatically insured and possible clashes avoided.

5 Expected counting rates and data-taking strategy

We will discuss here only the expected counting rates and data taking strategy relative to the Λ -hypernuclei studies. The same problems related to other measurements (Secs. 2.7, 2.8) would be defined at a later stage. We must first of all underline that the physics program, that is a nuclear physics one, is rather broad and must consider:

1. nuclear targets with different A , spanning the Periodic Table;
2. spectra taken with a broad momentum band (from ~ 100 to 270 MeV/c) but moderate resolution (~ 2 MeV), using a reduced field intensity (~ 0.5 T);
3. spectra taken in a narrow momentum band ($220 \div 270$ MeV/c) but with the best resolution that we could attain (~ 500 KeV).

In the following we will always assume a luminosity $\mathcal{L} = 10^{32} \text{ cm}^{-2} \text{ s}^{-1}$, the initial one foreseen at DAΦNE, and we will calculate the counting rates in this hypothesis. Counting rates at higher luminosity may obviously be scaled up. Furthermore, we will normalize our counting rates to an hypernuclear final state produced at a rate of 10^{-3} / stopped K^- , a typical value. It is worthwhile to remind that several hypernuclear final states will be produced at the same time. Taking into account all the numbers previously quoted, a MC simulation showed that we will produce ~ 100 hypernuclear states/hour per single state. Typically in a week of measurement, $\sim 1.7 \times 10^4$ events for state could be collected with high resolution requirement. Obviously, taking into account a possible background of $\sim 1/10$ of the signal, states produced at a rate of $\sim 10^{-5}$ /stopped K^- could be identified.

For the measurement of hypernuclear decays, the counting rate relative to the proton stimulated decay will be about 8 ev/hour and about 1.5 ev/hour for the neutron stimulated one. This last number will increase to ~ 2 ev/hour if the end caps too will be covered by scintillators. Again in 1 week of measurement, more than 250 neutron stimulated non-mesonic decays will be collected, allowing a measurement of the ratio R_n/R_p (7) defined in Sec. 2.3 with a statistical precision of less than 10%.

We may quote for comparison the counting rate at existing or approved machines:

- at BNL both (K^- , π^-) and (π^+ , K^+) reactions are utilized to produce and study hypernuclei. The spectrometer so far used allowed an energy resolution on the hypernuclear states of 2÷3 MeV. An upgrade could reach ~ 1 MeV or less. Production rates of hypernuclear states are of the order of a few (1÷5)/hour [69]. The spectrometer allows the installation of other counters for detecting the products from the decay of hypernuclei. We have no more details on future plans. We may remind that the only counter experiment, just performed at BNL [15] which provided measurements for non-mesonic decays, obtained a few tens of neutrons in coincidence in total, in several days of data taking.
- At KEK the new toroidal spectrometer [43] will allow the production of hypernuclei with stopped K^- at a rate of about 10 ev/hour (always normalized to a production rate of 10^{-3} / stopped K) with an energy resolution of ~ 700 KeV. The structure of the spectrometer however, is such that the products from hypernuclei decay are hardly detectable.
- At CEBAF an estimate [70] of the production of hypernuclei via the (e , e' , K^+) reaction gives 5 ev/hour with a resolution initially of 1.2 MeV (SOS Spectrometer, Hall C), finally of 200 KeV. Again, hypernuclear decays are hardly detectable.

The big difference in counting rates at DAΦNE, even at $\mathcal{L} = 10^{32} \text{ cm}^{-2} \text{ s}^{-1}$ is not only due to the hypernuclei production rate, but also to the large solid angle of detection and to the fact that the same detector is used both for the spectroscopy of π^- from the hypernucleus formation reaction and for the detection of the decay products. In other apparata these tasks are performed by different detectors, subtending smaller solid angles.

For the above measurement, the maximum field intensity will be used. Then only the final part of the typical spectrum shown by Fig. 10 will be detected. Pions with

momentum lower than $\sim 200 \div 220$ MeV/c will spiralize inside the detector, without reaching the external scintillator barrel, and giving a reduced event rate.

For studies in which the full spectrum will be examined, with modest resolution (2 MeV) at a lower field (0.5 T), the event rate could reach the limit of the acquisition system (100 Hz). If we will decide to dedicate a long effort on this subject, following the first exploratory runs, second level triggers may be eventually be activated.

Concerning finally the possible detection of π^+ , related to H-particle production, the crucial point is the evaluation of the background of π^+ following K^- capture in nuclei and due to the decay of quasi-free Σ^+ produced in the reaction and to pion charge exchange reactions in nuclei, following the primary interaction of stopped K^- . As previously done we prefer to take into account the existing experimental information, instead of following phenomenological or pseudo-theoretical estimates. By extrapolating down to 100 MeV/c the experimental π^+ spectra reported by Hayano et al. for a ^4He target [68], we may estimate that the background contribution will be the same than a signal due to a π^+ production rate, via H decay, of 10^{-5} /stopped K^- .

In conclusion, we estimate that if a calendar year will correspond to 150 days of real data taking, in such a time, at $\mathcal{L} = 10^{32} \text{ cm}^{-2} \text{ s}^{-1}$, the experimental program outlined in Sec. 2.2÷2.5 could be performed, allowing an unprecedented step forward in hypernuclear physics. In a following year we could concentrate on specific items, namely hypernuclear physics at lower production rate, profiting also of a foreseen increase in the luminosity. Other measurements, like $K - \mathcal{N}$ interaction (Sec. 2.8) and K -Nucleus scattering (Sec. 2.7), requiring some modifications on the apparatus, could be started.

6 Construction schedule and cost

The goal of completing FINUDA by the end of 1995 is dictated by the circumstance that by that time DAΦNE will provide the first (e^+ , e^-) circulating beams, and that a full physics program would be performed with the initial luminosity $\mathcal{L} = 10^{32} \text{ cm}^{-2} \text{ s}^{-1}$. Two items of those detailed in Sec. 4 are the most critical for the timing: the magnet and the LMDCs. For the solenoid, informal contacts with firms allowed us to know that the time needed for delivering the magnet is two years from the date of the order. Then, in order to start the installation of the solenoid in the second part of 1995, it is necessary to place the order (including the non negligible bureaucratic duties) in the first half of 1993. The second item (drift chambers) needs a strong R&D and prototyping work,

already started. We plan to finish this job by mid 1993, and then have two full years for the construction and tests. We notice that we will benefit from the fact that one of the Groups in our Collaboration (TRIUMF), has easy access to low energy test beams at the TRIUMF meson factory. Together with the Trieste and Bari Groups, which are too presently carrying out experiments at TRIUMF, they will organize and follow most of the test on prototypes of detectors for the central/interaction region. Tests on LMDCs and STs could be done at CERN and we will benefit of the help and advice of Prof. F. Sauli and his group.

The cost estimate of the FINUDA Detector, in July 1992 in MLit, is reported in Tab. 7. We quote a 5 month old evaluation since it corresponds to our request to INFN Nuclear Physics Committee (Gruppo III).

Tab. 8 reports the time schedule.

Table 7: Cost estimate of the FINUDA Detector, in July 1992 MLit

Superconducting Solenoid	4000
ISIM and OSIM (electronics included)	1500
TOFINO and TOFONE (electronics included)	1000
LMDCs and STs (electronics included)	2300
Trigger	300
DAQ	700
Gas Control System	300
Mechanics	700
Targets	100
Miscellanea	400
Contingencies	300
Total	MLit 11600

Table 8: Time schedule for FINUDA Installation

Year	Magnet	Drifts	Central Detector	TOF	DAQ
93	Order	Prototypes, R&D	Design and	Design and	Design Architecture
94	Delivery	Construction	Construction	Construction	Delivery
95	Installation	Tests + Installation	Installation	Installation	Installation
96					

Appendix 1

We list here references of previous works performed by some of us on specific experimental topics related to FINUDA and successfully used in experiments.

1) π/K discrimination with thin scintillators:

- G.C. Bonazzola *et al.*, *A Double Magnetic Spectrometer for the Study of Hypernuclei Production by K^- in flight*, *Nucl. Instr. Meth.* **123** (1975) 269.

2) Drift Chambers in magnetic field:

- E. Chiavassa *et al.*, *Multiwire and Drift Chambers for the Omicron Spectrometer*, *Nucl. Instr. Meth.* **156** (1978) 187.

3) Neutron Detection by large scintillator arrays:

- M.T. Tran *et al.*, *Differential Cross Sections for Radiation Capture of pions of Hydrogen in the Δ region*, *Nucl. Phys.* **A324** (1979) 301.

4) Use and Calibration of scintillators with good time resolution:

- G.C. Bonazzola *et al.*, *Real Time Compensation of the Path Spread in Large time-of-flight systems*, *IEEE Trans. Nucl. Sci.* **36** (1989) 806;
- G.C. Bonazzola *et al.*, *The Laser Calibration System of the OBELIX Spectrometer*, *IEEE Trans. Nucl. Sci.* **38** (1991) 393.

5) DAQ:

- (OBELIX) F. Balestra *et al.*, *IEEE Trans. Nucl. Sci.* **36** (1989), 713;
- (OBELIX) M. Agnello *et al.*, *IEEE Trans. Nucl. Sci.* **37** (1990), 315;
- (OBELIX) F. D'Isep *et al.*, *IEEE Trans. Nucl. Sci.* **38** (1991) 311;
- (OBELIX) M. Agnello *et al.*, *IEEE Trans. Nucl. Sci.* **39** (1992).

6) Running of Large non-focusing Spectrometers:

- (IPER) G.C. Bonazzola *et al.*, *Production of $^{12}_{\Lambda}C$ by K^- in flight*, *Phys. Lett.* **B53** (1974) 297;
- (Omicron) T. Bressani *et al.*, *Investigation of the doubly coherent production of π^- by 3He ions of 910 MeV on the Li isotopes*, *Phys. Rev.* **C30** (1984) 1755;
- (OBELIX) A. Adamo *et al.*, *Meson Spectroscopy with Antineutrons*, *Phys. Lett.* **B287** (1992) 368.

Appendix 2

An alternative readout system for SMD

In order to reduce the number of electronic channels, clusters of about 10 micro-strips can be processed as a whole. This operation, however, will select portions of wafer capable of measuring the position of only one particle: two (or more) particles separated in time by few tens of ns will degrade the position information of each others. Such an occurrence will cause an inefficiency in data taking. As an example, we quote this inefficiency to be about 10% for micro-strip pitch of $100\ \mu\text{m}$ clustered in numbers of ten.

The position of a detected particle will be determined by a time-of-flight method. START will be delivered by TOFINO and stop will be collected at the two edges of each micro-strip cluster. This technique offers some advantage over the more conventional readout technique used in high energy physics [47], [48], [71]. In the following we will emphasize the advantages and briefly discuss the TOF method.

Each micro-strip of a cluster will be connected to a fixed delay (10 ns). Both edges of this chain will be preamp/amplified, and the preamp/amplifier will have a rise-time of about 10 ns to meet the pulse response of a silicon micro-strip detector [46]. Such a signal rise-time is requested to perform an optimum timing. Then, analog signals will feed a discriminator (either channels of a standard leading edge module, or an on-board shaper/discriminator chip) and output logic signals will stop a TDC (for instance, LeCroy VME 1177 multihit TDC). For each event, two time measurements will be collected, T_L and T_R ($L = \text{left}$, $R = \text{right}$). $T_L + T_R$ will give the cluster length. Hence all spurious events (mainly noise associated with the wafers) capable of triggering the electronic chain, but being separated by more than a micro-strip transit time ($< 10\ \text{ns}$) will selectively be rejected. $T_L - T_R$ will identify the micro-strip position, whose pitch establishes the resolution. The proposed electronic chain will not carry out (differential) energy informations: the analog signal will be discriminated and shaped right after the preamp/amp stage. However, they are not required by the FINUDA detector.

The TOF method will appreciably reduce the number of readout channels. We assess that $3500\div 4000$ readout channels will accompany the ISIM and OSIM arrays. The exact number will be established after both thorough MC simulations and tests with pion beams at TRIUMF. However, we estimate that we need about 3 VME crates of TDC channels (LeCroy 1177 multihit TDC model) to entirely instrument ISIM and OSIM. If we realize that each electronic chain associated to a cluster must individually be discriminated, then we require the same amount of discrimination channels as for TDCs. Finally, keeping

within reasonable limits the on-board electronic elements solves the problem of cooling the ISIM and OSIM: the power consumption of this setup can likely be cooled with an air flow.

Appendix 3

Microstrip gas chamber option

As an option to the SMD we are considering the use of a cylindrical Gas Microstrip Chamber (GMSC)[72] for use as tracker close to the nuclear target. The advantages of Gas Microstrip Detector (GMD) are a smaller amount of material on the particle trajectory, typically few hundred μm of light polymer foil (Kapton), a cylindrical shape with a radius adjusted to the needs and fully efficient over the whole surface; the disadvantage is a coarser localization accuracy, around 50 μm in the radial direction and 500 μm along the z -direction, for perpendicular tracks. However, both localization accuracy and detection efficiency in GMSC degrade for incidence angles exceeding $15^\circ \div 20^\circ$ to the normal in the plane perpendicular to the anodes, due to geometrical reasons: there is just not enough ionization produced in the gas volume corresponding to each strip². One can therefore envisage the use of a GMSC only for the detection layer internal to the nuclear target.

GMS are very recent devices, still experimental; a very large development effort is however on the way mostly motivated by the requirements of LHC and SSC (large GMSC arrays are integral parts of the three major technical proposals for the colliders). At CERN an R&D project is on the way to develop the devices at the required scale (several hundred meters of active area [73]).

Fig. 35 shows schematically the structure of the GMSC. Thin metal strips are laid down on an insulating substrate and alternatively connected to potentials as anodes and cathodes. Electrons released in the upper layer of gas, between the strips and the drift electrode, are collected and amplified by avalanche multiplication. Proportional gains between 10^3 and 10^4 can be obtained, allowing detection of minimum ionizing particles; localization accuracies better than 50 μm have been obtained. While the standard substrate used so far has been thin glass or silicon, GMSC of small size have been manufactured and tested on thin (50 to 100 μm) polymer foils [74]; some more development is on the way to realize devices with sizes up to $25 \times 25 \text{ cm}^2$.

A conceptual design of a cylindrical thin-foil GMD with two-coordinate readout is

²The detection efficiency is not affected by the angle between the track and the anode strips, in the plane containing both; in fact, due to the larger energy loss in the thicker layer of gas, it should improve.

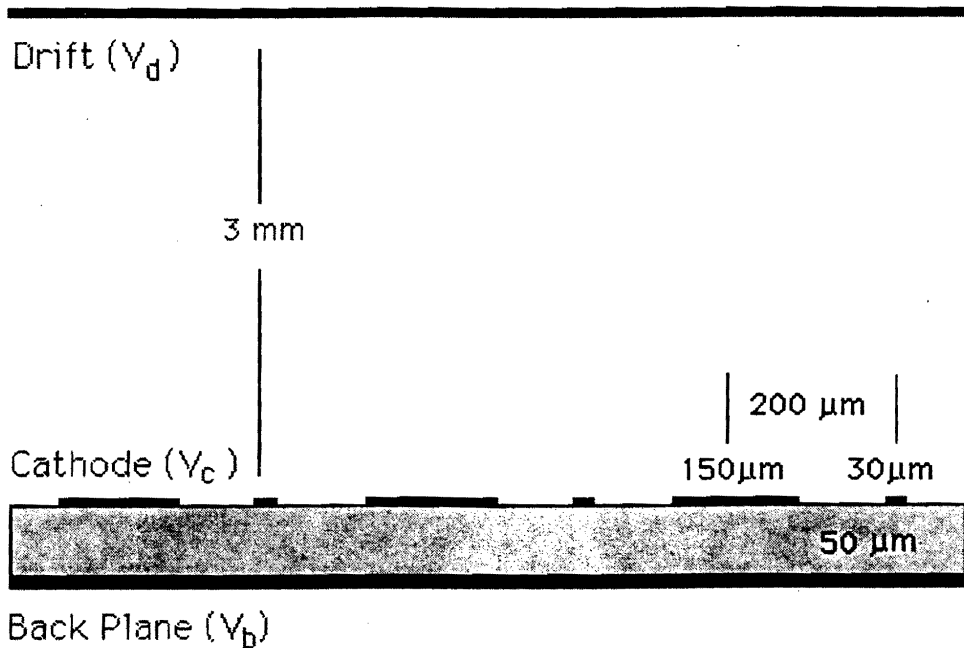


Figure 35: Structure of GMSC.

shown in Fig. 36. The main coordinate is obtained from the readout of the strips on the active side, while the second coordinate is obtained from the readout of strips on the back plane, etched with an angle to the main ones, and also at a 200 μm pitch.

With analogue readout of the pulses on the cathodes, localization accuracies around 30 μm have been measured for minimum ionizing particles [75]; it seems reasonable to assume that 50 μm can be obtained in the proposed GMD for the radial coordinate. With an angle of 15° for the back plane strips, and taking into account some losses due to the smaller signals, we estimate an accuracy of around 300 μm rms for the longitudinal coordinate. With the proposed choice of geometry, 200 μm pitch and 50 μm thick substrate, both the cathode and the back plane strips can be operated at ground potential, thus avoiding the use of HV capacitors for the readout [75]. To provide structural strength to the detector, the inner cylinder can be glued to a light expanded polyurethane (Rhoacell) cylinder, few mm thick as shown in the figure.

As readout electronics, we foresee the use of large scale integrated chips developed for readout of Silicon Microstrips; they have typically 128 amplifiers-sample and hold per chip, with a size compatible with the 200 μm pitch of the strips.

Tab. 9 provides summary information on the inner GMD.

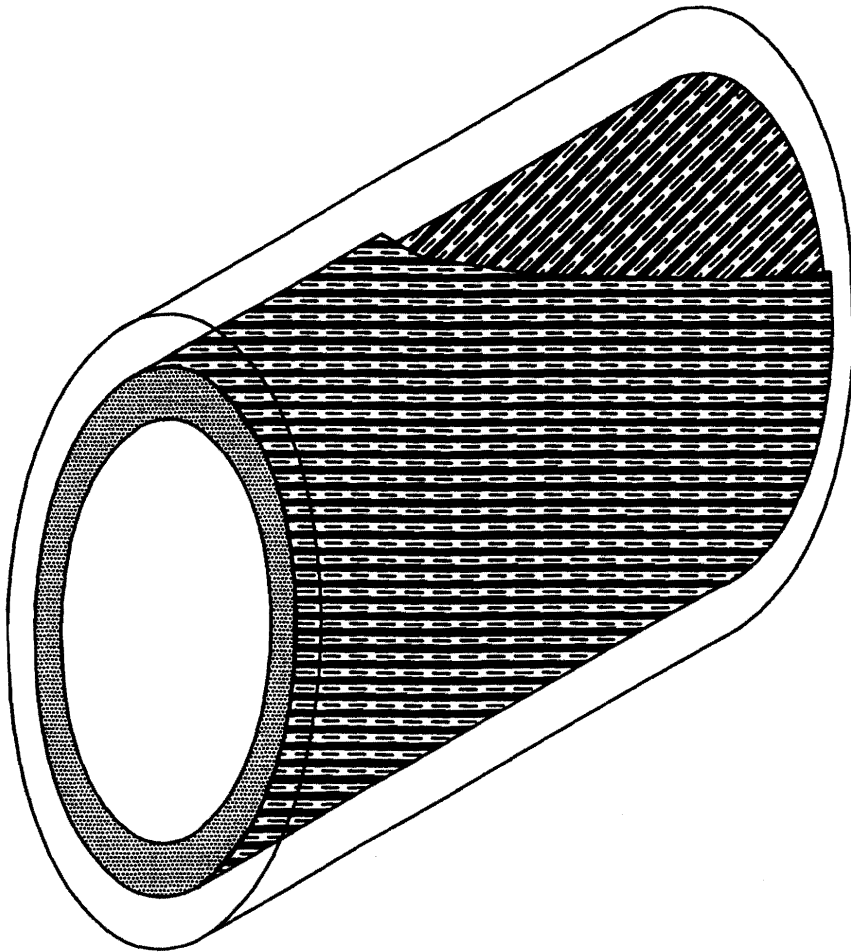


Figure 36: Sketch of a cylindrical thin-foil GMD.

Table 9: Summary information on the inner GMD.

diameter	10 cm
length	12 cm
strips pitch (anode to anode)	200 μm
substrate thickness	50 μm Kapton on 3 mm Rhoacell
total radiation length	$10^{-3} X_0$
drift electrode	50 μm Kapton
readout channels (cathodes)	1600
readout channels (back plane strips)	1600

Appendix 4

More technical details on the Superconducting Solenoid

The tubes used to cool the coils are configured in such a way to assure a natural convection circulation during the operation at 4.2 K. During the magnet cooling down, the liquefier compressor will maintain the necessary gas flux. The circulation for natural convection is reliable and self controlled, since it increases naturally where the sections are warmer, being there the cross section greater. The cylinder, moreover, being thermally and magnetically coupled to the coils, causes, in case of quenching, the so called *quench back*. This increases the magnet protection in case of transition to the normal state, since it decreases the temperature gradients due to heat generation by Joule effect in the conductor.

In the containing cylinder are housed also the pivots for the axial and radial rods which hold the effective weight of the cooled mass and of the electromagnetic stresses between the coils and the yoke. These rods can be made in Titanium alloy Ti 6 Al 4 V ELI grade.

The coils will be enclosed inside a thermic shield cooled by supercritical helium at 60 K, 10 bar, with the surfaces faced to the walls of the vacuum chamber covered by 20÷30 layers of aluminized mylar with high emissivity.

The vacuum chamber will be connected through a very short vacuum line to the descending current cryostat. In the line will pass also the two conductors for the electric power and 4 tubes (IN-OUT for helium at 4.5 K and 60 K). The descendent cryostat houses the two descendants cooled by helium vapors coming from a helium reservoir at 4.3 K, 1.1 bar, and the connection to the quench line. The above helium reservoir can ensure the magnet cooling for some time in case of failure of the 4.2 K supply. On the cryostat of the descendant is also connected the pumping system for the thermic insulating vacuum.

The helium liquefier, constituted by a cold box with helium tank and screw-type compressor, will have a maximum flow of 40 l/h and will be automatically driven. Alternatively, it could be possible to use the helium liquefier system of the Frascati National Laboratories.

The coils will be protected from the quench effects by a fast discharge circuit on a protection resistor connected in parallel. If a normal zone appears in one of the coil layers, the quench detector opens the contact and the energy in the magnetic field is dissipated on the resistor. Fixing at 1000 V (± 500 V) the maximum voltage at the magnet ends

the discharge time will be 6.6 s. In this case the maximum temperature reached after the quench is ~ 65 K and this value is not a problem for the structural integrity of the coils.

In case of quenching, three different alarm levels will be provided: two software and one hardware. The software alarms will act on the magnetic system power supply; the hardware one will be more drastic, and will provide the complete magnet discharge, in case of exceptionally dangerous situations.

Acknowledgements

We are deeply indebted to Prof. L. Maiani for his continuous encouragement and precious advice on the physics aspects.

Prof. R. Baldini and Prof. E. Iarocci are warmly acknowledged for their strong support during all the stages of the proposal.

We are particularly grateful to Prof. F. Sauli for his invaluable advice on all problems related to the experimental feasibility of the proposed detector.

Prof. H.A. Thiessen and Prof. T. Yamazaki are acknowledged for useful discussions and comments.

References

- [1] G. Vignola, in *Workshop on Physics and Detectors for DAΦNE*, Frascati, April 9-12, 1991; ed. G. Pancheri, (INFN-LNF, 1991), p. 11.
- [2] The KLOE Collaboration, *KLOE a General Purpose Detector for DAΦNE*, Rep. LNF-92/019 (IR), 1992.
- [3] KAON Factory Proposal, edited by TRIUMF (Vancouver, Canada) 1985.
- [4] T. Bressani in *Workshop on Physics and Detectors for DAΦNE*, Frascati, April 9-12, 1991; ed. G. Pancheri (INFN-LNF,1991), p. 475.
T. Bressani in *Common Problems and Ideas of Modern Physics*; eds. T. Bressani, B. Minetti and A. Zenoni (World Scientific, Singapore, 1992), p. 211.
- [5] S. Sakata, *Prog. Theor. Phys.* **16** (1956) 636.
- [6] A. Gal, *Adv. Nucl. Sci.* **8** (1977) 1.
- [7] R.E. Chrien in Proc. *LAMPF Workshop on (π, K) Physics*, Los Alamos, NM 1990; eds. B.F. Gibson, W.R. Gibbs, M.B. Johnson, AIP (New York 1991), p. 28.
- [8] E.V. Hungerford and L.C. Biendenharn, *Phys. Lett.* **B142** (1984) 232.
- [9] Proc. *LAMPF Workshop on (π, K) Physics*, Los Alamos, NM 1990; eds. B.F. Gibson, W.R. Gibbs, M.B. Johnson, AIP (New York 1991).
- [10] Proc. *International Symposium on Hypernuclear and Strange Particle Physics*, Shimoda, Japan, Dec. 9-12, 1991; eds. T. Fukuda, O. Morimatsu, T. Yamazaki and K. Yazaki. *Nucl. Phys.* **A547** (1992) N. 1, 2.
- [11] C.B. Dover, D.J. Millener and A. Gal, *Phys. Rep.* **184** N.1 (1989) 1.
- [12] H. Bandò, T. Motoba and J. Žofka, *Int. J. Mod. Phys.* **A5** N.21 (1990) 4021.
- [13] J. Cohen, in *Prog. Par. Nucl. Phys.*, Vol. **25** (Pergamon Press, 1990) 139.
- [14] W. Cheston and H. Primakoff, *Phys. Rev.* **92** (1953) 1537;
H. Primakoff, *Nuovo Cimento* **3** (1956) 1934;
M. Rudermann and R. Karplus, *Phys. Rev.* **102** (1956) 247.
- [15] J.J. Szymansky *et al.*, *Phys. Rev.* **C43** (1991) 849.

- [16] K.J. Nield *et al.*, *Phys. Rev.* **C13** (1976) 1263.
 - [17] J.P. Bocquet *et al.*, *Phys. Lett.* **B182** (1986) 146;
J.P. Bocquet *et al.*, *Phys. Lett.* **B192** (1987) 312.
 - [18] T.A. Armstrong *et al.*, preprint CERN-PPE/92-106 (1992) 1.
 - [19] K. Itonaga, *Nuovo Cimento* **102A** (1989) 501.
 - [20] M. Sakaguchi *et al.*, *Nuovo Cimento* **102A** (1989) 511.
 - [21] R.A. Schumacher, *Nucl. Phys.* **A547** (1992) 143c.
 - [22] W.M. Alberico *et al.*, *Phys. Lett.* **B256** (1991) 134.
 - [23] R. Alzetta *et al.*, Preprint MITH 93/8 (Milano University).
 - [24] L. Majling, *Few Body Systems Suppl.* **5** (1992), 348 and in Proc. *National Conference on Physics of Few-Body and Quark-Hadronic Systems*, Kharkov (Ukraine), 1-5 June 1992.
 - [25] K. Seth in Proc. *Workshop on Nuclear and Particle Physics at Intermediate Energies with Hadrons* Trieste 1-3 April, 1985; eds. T. Bressani and G. Pauli, SIF Conf. Proc. Vol. 3 (1985), p. 1.
 - [26] R.L. Jaffe, *Phys. Rev. Lett.* **38** (1977) 195, 1617(E).
 - [27] C. Guaraldo in Proc. *Hadronic Physics at Intermediate Energy II*; eds. T. Bressani, B. Minetti and G. Pauli (North Holland, Amsterdam, 1987), p. 139.
 - [28] Y. Iwasaki, T. Yoshic and Y. Tsuboi, *Phys. Rev. Lett.* **60** (1988) 1371.
 - [29] T. Kishimoto, *Nuovo Cimento* **102A** (1989) 553.
 - [30] R. Bertini *et al.*, *Phys. Lett.* **B90** (1980) 375.
 - [31] H. Piekarz *et al.*, *Phys. Lett.* **B110** (1982) 428.
 - [32] T. Yamazaki *et al.*, *Phys. Rev. Lett.* **54** (1985) 102.
 - [33] R.A. Krauss *et al.*, *Phys. Rev.* **46C** (1992) 655.
 - [34] P.B. Siegel, W.B. Kaufmann and W.R. Gibbs, *Phys. Rev.* **C31** (1985) 2184.
-

- [35] W. Weise, *Nuovo Cimento* **102A** (1989) 265.
- [36] T.P. Cheng and R.F. Dashen, *Phys. Rev. Lett.* **26** (1971) 594 and *Phys. Rev.* **D13** (1976) 216; T.P. Cheng, *Phys. Rev.* **D13** (1973) 2161; C.A. Dominguez and P. Langacker, *Phys. Rev.* **D24** (1981) 1905.
- [37] J. Ashman *et al.*, *Phys. Lett.* **B206** (1988) 364 and *Nucl. Phys.* **B328** (1989) 1.
- [38] J. Gasser, *Physics with Light Mesons* in Proc. *Second International Workshop on πN Physics*, Los Alamos LA-11184-C (1987).
- [39] S. Okubo, *Phys. Lett.* **B5** (1965) 165; G. Zweig, CERN Report No. 8419/TH412 (1964) unpublished; I. Iiuzuka, *Prog. Theor. Phys. Suppl.* **37-38** (1966) 21.
- [40] J. Ellis, E. Gabathuler, and M. Karliner, *Phys. Lett.* **B217** (1989) 173.
- [41] E.M. Henley, G. Krein, and A.G. Williams, *Phys. Lett.* **B281** (1992) 178 and E.M. Henley *et al.*, Proc. *XIIIth European Conference on Few-Body Problems in Physics*, Island of Elba, Italy, Sept. 9-14, 1991.
- [42] R.L. Jaffe and C.L. Korpa, *Comments Nucl. Part. Phys.* **17** (1987) 163.
- [43] P.M. Gensini, in *Workshop on Physics and Detectors for DAΦNE*, Frascati, April 9-12 1991; ed. G. Pancheri (INFN-LNF, 1991), p.453.
- [44] T. Yamazaki *et al.* *Nuovo Cimento* **102A** (1989) 695.
- [45] H. Tamura *et al.* *Nuovo Cimento* **102A** (1989) 575.
- [46] As an example, we quote the Micron Semiconductor Limited, Sussex, England.
- [47] There is a variety of charge-sensitive chips designed to preamp/amplify and optionally to multiplex the charge pulse from silicon micro-strip detectors. We quote some articles for a detailed discussion of the performances of these chips.
E. Nygard *et al.*, *Nucl. Instr. Meth. in Phys. Res.* **A301** (1991) 506; S.A. Keinfelder *et al.*, *IEEE Trans. Nucl. Sci.* **NS-35**, (1989) 171.
- [48] A. Lang and J.P. Vanuxen, CERN, EP-Electronics Note 90-01(1990).
- [49] G. Charpak *et al.*, *Nucl. Instr. Meth.* **108** (1973) 413;
A. Breskin *et al.*, *Nucl. Instr. Meth.* **119** (1974) 9.

- [50] *Low mass drift chambers for FINUDA*. FINUDA tracking internal note 92-01.
- [51] V. Cindro *et al.*, *Nucl. Instr. Meth.* **A309** (1991) 411.
- [52] *LME properties reviewed*. FINUDA tracking internal note 92-02.
- [53] *Low mass gases for tracking*. FINUDA tracking internal note 92-04.
- [54] B. Zhou *et al.*, *Nucl. Instr. Meth.* **A287** (1990) 439.
- [55] H.N. Nelson, SLAC-PUB-4318, May 1987.
- [56] W.W. Ash *et al.*, SLAC-PUB-4047, August 1986;
J. Adler *et al.*, SLAC-PUB-4578, August 1988.
- [57] *Snowmass Report, 1986*; Solenoidal Detector Collaboration, Technical design report SDC-92-201.
- [58] M.T. Tran *et al.*, *Nucl. Phys.* **A324** (1979) 301.
- [59] G.C. Bonazzola *et al.*, *IEEE Trans. Nucl. Sci.* **38** (1991) 393.
- [60] O. Biebel *et al.*, *The Laser system for calibration and monitoring of the OPAL jet chamber*, CERN, Feb. 7, 1992.
- [61] S.P. Beingessner *et al.*, *Nucl. Instr. Meth. Phys. Res.* **A263** (1988) 26.
- [62] R. De Salvo, *Nucl. Instr. Met. Phys. Res.* **A235** (1985) 509.
- [63] H.J. Klein and J. Zoll, *PATCHY Reference Manual*, CERN Program Library L400 (1977).
- [64] R. Brun, F. Bruyant, M. Maire, A.C. McPherson and P. Zancarini, *GEANT3*, CERN Report DD/EE/84-1 (1987).
- [65] A. Antonelli *et al.*, KLOE Note No. 3 (1991);
A. Antonelli *et al.*, KLOE Note No. 23 (1992).
- [66] V. Innocente, M. Maire and E. Nagy, *GEANE*, L3 Report No. 572 (1988).
- [67] R. Brun and J. Zoll, *ZEBRA User Guide*, CERN Program Library Q100 (1987).
- [68] R.S. Hayano *et al.*, *Nuovo Cimento* **102A** (1989) 437.

- [69] P.H. Pile in Proc. *LAMPF Workshop on (π, K) Physics*, Los Alamos, NM 1990; eds. B.F. Gibson, W.R. Gibbs, M.B. Johnson, AIP (New York 1991) p. 77.
- [70] E.V. Hungerford in Proc. *LAMPF Workshop on (π, K) Physics*, Los Alamos, NM 1990; eds. B.F. Gibson, W.R. Gibbs, M.B. Johnson, AIP (New York 1991) p. 224.
- [71] The literature describing performances of silicon micro-strip detectors embraces a large numbers of articles, we quote a couple of recent ones.
J. Ellet *et al.*, *Nucl. Instr. Meth. in Phys. Res.* **A317** (1992) 28;
Proc. Experimental Apparatus at Future High Energy Machines and Underground Laboratories;
Nucl. Instr. Meth. in Phys. Res. **A277** (1989) 138-169.
- [72] A. Oed *et al.*, *Nucl. Instr. Meth.* **A263** (1988) 351;
F. Angelini *et al.*, *Nucl. Instr. Meth.* **A283** (1989) 755.
- [73] R. Bouclier *et al.*, RD28: Development of Gas Microstrip Chambers.
- [74] R. Bouclier *et al.*, CERN-PPE/92-53 (1992)
- [75] F. Angelini *et al.*, *Nucl. Phys.* **B 23A** (1991) 254.

Contents

1	Introduction	3
2	The physics program of FINUDA	4
2.1	Λ -hypernuclei spectroscopy	4
2.2	Decay of hypernuclei and possible violation of the $\Delta I = \frac{1}{2}$ rule	7
2.3	Production of Λ -hypernuclei with a large neutron excess	12
2.4	Is there a π^+ decay mode of hypernuclei?	13
2.5	The puzzle of Σ -hypernuclei	15
2.6	K^+ -Nucleus total cross section	16
2.7	$K\mathcal{N}$ scattering at low energy and the σ -term	18
3	Production of Λ-hypernuclei	20
4	The FINUDA detector	24
4.1	General description	24
4.2	Internal scintillator barrel (TOFINO)	31
4.3	The Silicon microstrip detectors	35
4.4	The targets	36
4.5	Low mass drift chambers (LMDC)	37
4.6	The outer straw tube (ST) array	42
4.7	The outer scintillator array (TOFONE)	42
4.8	The Superconducting Magnet	44
4.9	First level trigger	47
4.10	Data acquisition (DAQ) architecture	49
4.11	Gas distribution and control system	55
4.12	Mechanical installation	57
4.13	Calibrations	59
4.14	Off-line software	63
5	Expected counting rates and data-taking strategy	67
6	Construction schedule and cost	69

List of Figures

- 1 Hypernuclear states obtained in the $^{89}\text{Y}(\pi^+, K^+) ^{89}_{\Lambda}\text{Y}$ reaction, showing the Λ in the s, p, d, f and g orbitals, as measured at AGS. The solid line represents a DWBA calculation (from Ref.[7]). 6
- 2 Baryon (upper row) and quark (lower row) configurations for the ^4He and $^5_{\Lambda}\text{He}$ systems. 7
- 3 Present experimental values of the lifetime τ_{Λ} of the Λ -hyperon in hypernuclei as a function of A (from Ref. [13]) with the addition of the new measurement for $^{238}_{\Lambda}\text{U}$ 9
- 4 Ratio Q^- of non-mesonic to π^- mesonic decay rates as a function of A (from Ref. [13]). 11
- 5 Ratio of neutron stimulated non-mesonic decay rate to the total non-mesonic decay rate as a function of A (from Ref. [13]). 12
- 6 Chart of light Λ -hypernuclei with binding energies B_{Λ} and particle instability thresholds ([from Ref. 24]). The neutron rich hypernuclei observable in (K^-_{stop}, π^-) reactions are indicated with \spadesuit 14
- 7 Decay rate of π^+ mesonic decay as a function of the H mass, for the hypernuclei $^{13}_{\Lambda}\text{C}$, $^5_{\Lambda}\text{He}$ and $^4_{\Lambda}\text{He}$. The ordinate scale is in (%) of the total decay rate (from Ref. [29]). 15
- 8 Experimental and theoretical values of \mathcal{R} [Ref. 33]. The shadowed band between solid lines corresponds to no "swelling" within the theoretical uncertainties. The dashed and continuous lines correspond, respectively, to calculations done with a 10% increase in the s-wave phase shift ($\delta R/R = 0.1$) and a density dependent rescaling effect with $const = 0.1$ 17
- 9 Kinematics in the forward direction for the Λ , and, respectively, Σ^0 production. The curves which limit the hatched areas downwards are for a π^- emission angle of 0° , those which limits upwards for 6° 21
- 10 π^- spectrum from ^{12}C (stopped K^-, π^-) reaction measured at KEK. The insert shows on an expanded scale the high momentum region, corresponding to the production of $^{12}_{\Lambda}\text{C}$ in the excited and ground state (from Ref. [44]). 22
- 11 Low-momentum regions of (stopped K^-, π^-) spectra on several nuclear targets. The vertical scale of all spectra is the intensity per stopped K^- (from Ref. [45]). 23

12	General view of the FINUDA detector.	25
13	The two views of the proposed target/interaction region.	28
14	Radial distributions of the stopping points, as obtained in a MC simulation for a Carbon target.	29
15	MC simulation of the effect of the “tagging technique” on the π^- reconstructed momentum spectrum. π^- momentum distribution with (solid line) and without (dotted line) corrections.	30
16	Momentum resolution with a tracking device based on LMDCs, as obtained by a MC simulation, for 270 MeV/c pions.	31
17	Momentum resolution with a TPC based tracking device, as obtained for a MC simulation, for 270 MeV/c pions.	32
18	ΔE in internal scintillator (1.5 mm thick) for different particles.	32
19	a) Time distribution of events recorded by TOFINO due to proton stimulated non-mesonic decays. The dashed and dotted lines refer to $\tau_\Lambda = 100$ and 200 ps respectively. The solid line shows the time distribution for prompt events ($\tau_\Lambda = 0$). The distributions are not corrected for the different path lengths. b) Same than a), but with corrections for the different path lengths.	34
20	Cross section of HADC.	38
21	Arrangement of the LMDC modules.	39
22	Cross section of LMDC.	39
23	Comparison of the drift velocities and longitudinal diffusion coefficient σ_l for mixture of He-CO ₂ (70%-30%), He-DME(70%-30%) and He-CO ₂ -DME(70%-25%-5%).	41
24	An example of the behaviour of the detection efficiency for a neutron scintillator’s bar (from Ref. [58]).	44
25	Drawing of the superconducting solenoid. Only one of the low beta Q-poles is drawn for simplicity.	45
26	A simplified scheme of the first level trigger.	48
27	General data acquisition scheme.	53
28	Data acquisition architecture.	54
29	Gas distribution and control scheme.	58
30	The installation of FINUDA in the DAΦNE building.	60
31	Side view of the solenoid and detector. Only one end-cup and low-beta Q-pole is shown for simplicity.	61

32	Cross section view of the solenoid with the TOFONE's phototubes.	62
33	Simulated event with proton stimulated decay.	64
34	Simulated event with neutron stimulated decay.	66
35	Structure of GMSC.	75
36	Sketch of a cylindrical thin-foil GMD.	76

List of Tables

1	ϕ decays.	3
2	Probabilities $P(x)$ of survival of K^\pm at different energies after a given length $x(\text{cm})$	4
3	Typical design parameters of HADC/LMDC.	40
4	Specifications and materials tentatively used for ST.	42
5	TOFONE features.	43
6	Main characteristics of the solenoid.	47
7	Cost estimate of the FINUDA Detector, in July 1992 MLit	71
8	Time schedule for FINUDA Installation	71
9	Summary information on the inner GMD.	76